Research Article

Modeling how a Powerful Airburst destroyed Tall el-Hammam, a Middle Bronze Age city near the Dead Sea

Phillip J. Silvia[1], Steven Collins[2], Malcolm A. LeCompte[3], Luis Costa[4], George A. Howard[5], James P. Kennett[6], Christopher R. Moore[7,8], Gunther Kletetschka[9,10], A. Victor Adedeji[11], Robert E. Hermes[12], Timothy Witwer[13], Kurt Langworthy[14], Joshua J. Razink[14], Valerie Brogden[14], Brian van Devener[15], Jesus Paulo Perez[15], Randy Polson[15], Radana Kavková[10], Marc D. Young[16] and Allen West[13,*]

[1]College of Archaeology, Trinity Southwest University, Albuquerque, NM 87109, USA; [2]School of Archaeology, Veritas International University, Albuquerque, NM 87109, USA; [3]Center of Excellence in Remote Sensing Education and Research, Elizabeth City State University, Elizabeth City, NC 27909, USA; [4]Ozen Engineering, Inc., 1210 E Arques Ave #207, Sunnyvale, CA 94085, USA; [5]Restoration Systems, L.L.C., Raleigh, NC 27604, USA; [6]Department of Earth Science and Marine Science Institute, University of California, Santa Barbara, CA 93106, USA; [7]South Carolina Institute of Archaeology and Anthropology, University of South Carolina, Columbia, SC 29208, USA; [8]SCDNR Heritage Trust Program, Land, Water, and Conservation Division, South Carolina Department of Natural Resources, Columbia, SC 27909, USA; [9]Geophysical Institute, University of Alaska Fairbanks, 903 Koyukuk Drive, Fairbanks, AK 99775, USA; [10]Faculty of Science, Charles University, Albertov 6, Prague, 12843, Czech Republic; [11]Department of Natural Sciences, Elizabeth City State University, Elizabeth City, NC 27909, USA; [12]Los Alamos National Laboratory (retired), Los Alamos, NM 87545, USA; [13]Comet Research Group, Prescott, AZ 86301, USA; [14]CAMCOR, University of Oregon, 1443 E 13th Ave, Eugene, OR 97403, USA; [15]Electron Microscopy and Surface Analysis Lab, Nanofab, University of Utah, Salt Lake City, UT 84112, USA; [16]College of Humanities, Arts and Social Sciences, Flinders University, Sturt Rd., Bedford Park, South Australia 5042, Australia

*Correspondence to: Allen West, E-mail: CometResearchGroup@gmail.com

ABSTRACT

A previous study presented evidence supporting the hypothesis that a low-altitude airburst approximately 3600 years ago destroyed Tall el-Hammam, a Middle-Bronze-Age city northeast of the Dead Sea in modern-day Jordan. The evidence supporting this hypothesis includes a widespread charcoal-and-ash-rich terminal destruction layer containing shock-fractured quartz, shattered and melted pottery, melted mudbricks and building plaster, microspherules, charcoal and soot, and melted grains of platinum, iridium, nickel, zircon, chromite, and quartz. Here, we report further evidence supporting a cosmic airburst event at Tall el-Hammam. Fifteen years of excavations across the city revealed a consistent directionality among scattered potsherds from individually decorated vessels, including one potsherd group distributed laterally approximately southwest to northeast across ~22 m, spanning six palace walls. Similar trails of charred grains, charcoal, and bone fragments were also found distributed across multi-meter distances inside the destroyed city. Although an earlier report of the directionality of this debris was challenged, further evidence presented here strengthens that interpretation. We also report Middle-Bronze-Age partially melted breccia that likely formed at >2230 °C, consistent with a cosmic event. We investigated additional glass-filled fractured quartz grains using ten analytical techniques, including transmission electron microscopy (TEM), scanning electron microscopy

(SEM), cathodoluminescence (CL), and electron backscatter diffraction (EBSD). These grains are inferred to have formed by high-pressure shock metamorphism, consistent with an earlier report that has been challenged. To test that the mode of destruction could have been an airburst, we produced a hydrocode computer model of a Type 2 or touch-down airburst, in which a high-temperature, high-pressure, high-velocity jet intersects Earth's surface, producing meltglass, microspherules, and shock metamorphism. The modeling shows that the explosive energy released can propel high-velocity airburst fragments to strike the Earth's surface, producing shock metamorphism and creating superficial craters potentially susceptible to geologically rapid erosion. Although the probability of such airbursts is low, the potential for substantial damage is high, especially in cities.

KEYWORDS

airbursts, shocked quartz, hydrocode modeling, asteroids, meltglass, breccia, Tall el-Hammam, Bronze Age, Dead Sea, Jordan Valley

Introduction

The destruction of an ancient city

Bunch et al. [1] described archeological excavations conducted since 2005 at Tall el-Hammam ("TeH"), an ancient walled city in the southern Jordan Valley northeast of the Dead Sea (Figure 1; **Appendix,** *Site setting* below). Located on what is called a "tell" or "tall" in Arabic and "tel" in Hebrew, the ruins are the stratified remains of an ancient heavily fortified urban center, now recognized as the largest continuously occupied Bronze Age city in the southern Levant [2]. Fifteen years of excavations revealed a widespread charcoal-and-ash-rich "terminal destruction layer" [3] up to 2 m thick that contained melted materials, including potsherds, mudbricks, roofing clay, and building plaster [1]. This layer also displayed peak concentrations of shock-fractured quartz, microspherules, charcoal, soot, and melted grains of platinum, iridium, nickel, zircon, and chromite [1]. For more information, see Appendix, Figures A1 and A2; **Appendix,** *Melted materials* below.

The ~2-m-thick destruction layer also contained potsherds from thousands of pottery vessels, some displaying individually distinctive decorative patterns, facilitating their reassembly. Plotting the locations of sherds from individual vessels showed them to be oriented in an approximately SW-to-NE linear direction across the complex (Figure 2). The trails of sherds were intermixed with chaotically deposited debris, including mudbrick fragments, objects of daily life, carbonized wood beams, charred grain, bones, and limestone cobbles burned to a chalk-like consistency. Most of these materials were suspended within the destruction matrix above, not atop the Middle-Bronze-Age (MBA) floors. For more on stratigraphy and sampling sites reported in Bunch et al. [1], see **Appendix,** *Stratigraphy of Tall el-Hammam* below.

In addition, unusually high salt concentrations (up to 4 wt%) in the destruction layer produced hypersalinity across the site. Background concentrations above and below the destruction layer were typically <1 wt%. The salt appears to have inhibited local agriculture around 3600 years ago and

caused an approximately 300-600-year-long abandonment of ~120 regional settlements within a diameter of ~26 km [1, 4].

Bunch et al. [1] concluded that the best explanation for this wide range of evidence is a cosmic airburst that destroyed the city, including the multi-story palace and temple complexes, and did significant damage to much of the massive 4-m-thick mudbrick rampart surrounding the city, especially along the SW-facing facade (see Appendix, Figures A3 and A4; **Appendix,** *Destruction of the palace* below).

Bunch et al. [1] modeled airbursts from 60-m to 75-m-wide bolides that produced near-surface airburst events. These are defined as "touch-down" or Type 2 airbursts [5–8], in which a high-temperature, high-velocity jet of vapor and fragments of the bolide reach Earth's surface [9]. The modeled airburst generated SW-to-NE-trending high-velocity winds that demolished all the city buildings and scoured the city ruins. Bunch et al.'s models are consistent with existing literature that fragmentation during an airburst is common and that when bolide fragments from airbursts reach Earth's surface, they can cause considerable surface damage [9, 10] (see **Appendix,** *Fragmentation of bolides* below).

Previous studies conclude that although airbursts mainly vaporize the bolide, fragments commonly reach the ground surface, and the kinetic energy of the airburst vapor jet may be high enough to produce shallow craters [7, 9, 11], along with shocked quartz, meltglass, microspherules, breccia, and other impact-related proxies. The following are some proposed examples of low-altitude Type 2 airbursts that caused extensive damage to Earth's surface: (i) Chrudim/Pardubice in the Czech Republic [12, 13], (ii) Nalbach/Saarlouis in Germany [14–16]. (iii) Chiemgau in Germany [17–27], (iv) Niederrhein in Germany [28], (v) Franconia in Germany [29], (vi) Sachsendorf Bay in Germany [30], (vii) seven possibly related strewn fields across about half of the Czech Republic [13], (viii) a 6400-year-old strewn field in Finland [31], (ix) the Luzice melt rock and megabreccia outcrops, proposed as evidence of a low-altitude airburst [32], (x) the 20-km-diameter Kolesovice airburst crater in the Czech Republic [33], (xi) a 2600-year old strewn field in Kansas [34], (xii) a
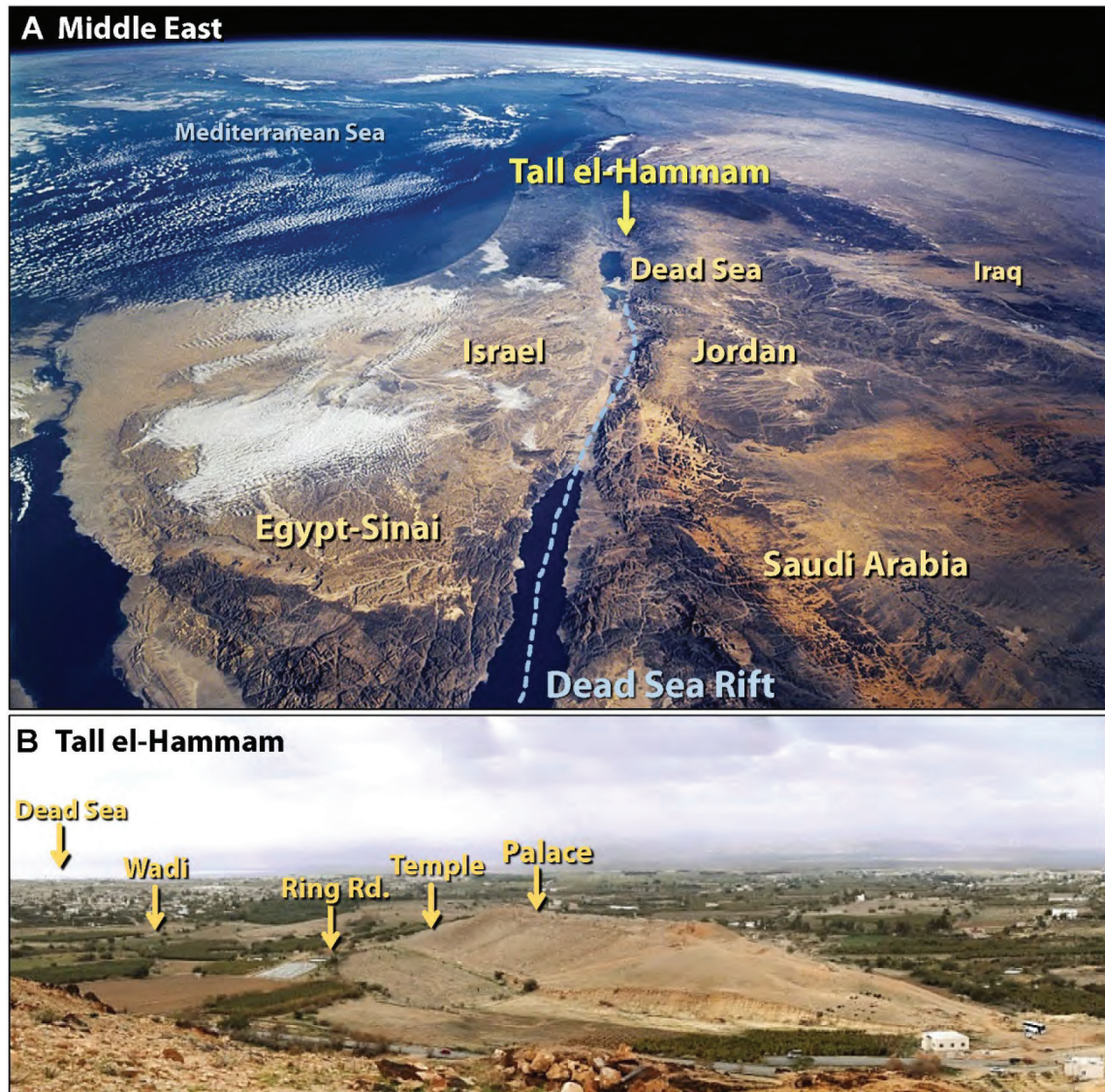
Figure 1: Location of Tall el-Hammam. (A) Photograph of the southern Levant, looking north, showing the Dead Sea, the site location (TeH), and nearby countries. "Dead Sea Rift" (dashed blue line) indicates a major tectonic plate boundary. The base image is from NASA's Space Shuttle, "The Sinai Peninsula and the Dead Sea Rift." Photograph: sts109-708-024, taken 12/16/2009, from the NASA Langley Research Center Atmospheric Science Data Center. **(B)** West-southwest-facing view of Tall el-Hammam showing sampling locations at the palace, temple, ring road, and wadi. The Dead Sea is faintly visible at the upper left below the arrow. Images and captions are adapted from Bunch et al. [1], usable under Creative Commons, CC by 4.0 (http://creativecommons.org/licenses/by/4.0/).

1600-year-old airburst in Ohio that destroyed several Native American villages [35], (xiii) a 5000-year-old airburst by an iron meteorite in Poland [36], (xiv) a ~12,500-year-old strewn field in the Atacama Desert of Chile [37–39], (xv) multiple airbursts on four continents 12,800 years ago by the Younger Dryas impact event [40–60], (xvi) a large airburst at the Dakhleh Oasis in Egypt ~145,000 years ago [61–63], (xvii) two near-surface airbursts in Antarctica, one ~430,000 years old and a second one ~2.3 Myr old [7, 8], and (xiii) an airburst in the Libyan Desert ~29 million years ago [64]. For more details, see **Appendix, *Airburst examples*** below.

The process by which airbursts can produce meltglass is described by Boslough and Crawford [65, 66] and quoted here because of its importance: *"… the hot jet of vaporized projectile (the descending "fireball") makes contact with the Earth's surface, where it expands radially. During the time of radial expansion, the fireball can maintain temperatures well above the melting temperature of silicate minerals, and its radial velocity can exceed the sound speed in air. We suggest that the surface materials can ablate by radiative/convective melting under these conditions, and then quench rapidly to form glass after the fireball cools and recedes."*

Tall el-Hammam may be the second oldest human settlement destroyed by a cosmic airburst/impact, after the destruction of the village at Abu Hureyra, Syria ~12,800 years ago [46, 47, 53, 54, 67]. It may also be the earliest
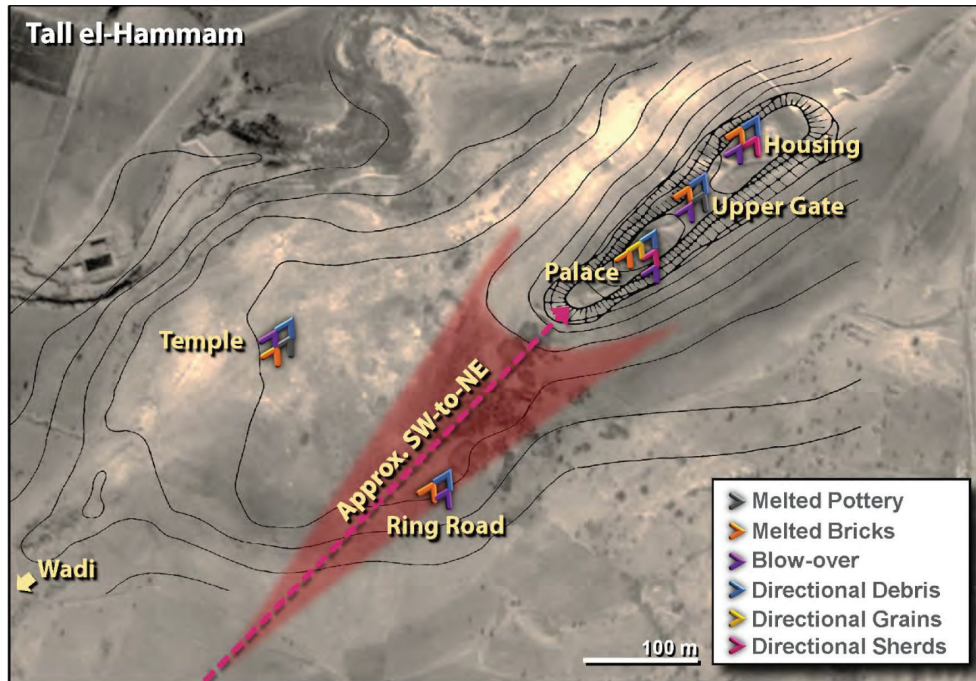
Figure 2: Directionality of debris across Tall el-Hammam. Color-coded arrows indicate the type and inferred direction of six categories of debris. A red dashed arrow highlights the inferred variation in the directionality of the airburst shockwave, moving from approximately SW to NE across excavations covering an area of ~58,000 m² (~480 m long by up to ~240 m wide). While the directions of most oriented materials fall within the red-shaded area, not all did. The conclusion supporting directionality is based on the following: 32 photographs and drawings of NE-oriented potsherds; 8 photographs of 7 ~NE-oriented bones; 16 of charred grains and charcoal; 7 of plaster detritus; 4 of windblown "blow-over" deposits; and 12 captioned photographs and ~100 observations from archaeological Season Reports and the PhD dissertation of co-author, Dr. Silvia [4]. Image direction and caption have been revised from Bunch et al. [1], usable under Creative Commons, CC by 4.0 (http://creativecommons.org/licenses/by/4.0/).

human settlement whose destruction by a cosmic airburst led possible eyewitnesses to construct an oral history that was written down centuries later [1]. For further discussions of this evidence, see Bunch et al. [1] and references [2–4, 68–82].

Age of the terminal destruction layer

To date the destruction layer in the palace, 20 radiocarbon dates were acquired by Bunch et al. [1] on carbonized wood (n = 11), carbonized grain (n = 3), carbonized material (n = 4), burned bone (n = 1), and organic sediment (n = 1) (**Appendix, *Bayesian analysis, Table A1***). Bunch et al. [1] used the OxCal radiocarbon calibration program, version 4.4 (IntCal20 calibration curve), to determine a Bayesian-derived age for the terminal destruction layer of 3611 ± 21 cal BP (before 1950), rounded to 3600 cal BP.

Study objectives

In this study, we investigate and present new evidence for shock-fractured quartz, brecciated meltglass, and the SW-to-NE orientation of melted debris within the city. We also introduce a hydrocode-based airburst model to explain the destruction of Tall el-Hammam. Most airbursts occur at high altitudes with minimal effects on the Earth, so we chose

to model a 55-m asteroid that would produce a touch-down airburst approximately 653 m above the Earth's surface. The model tests whether such an airburst can produce the evidence observed at Tall el-Hammam. Note that the modeling parameters are not unique solutions; similar effects can be produced by numerous variations in the selected parameters (e.g., different bolide diameters, densities, velocities, and entry angles).

We explore specific questions about the touch-down airburst modeling:

1) Are the temperatures high enough to melt pottery and produce meltglass?
2) Can touch-down airburst conditions lead to the formation of microspherules?
3) Is the shockwave powerful enough to destroy a multi-story mudbrick palace?
4) Can the shockwave shatter and distribute potsherds directionally across 22 m?
5) Can a touch-down airburst produce impact brecciated meltglass?
6) Can impacts by airburst fragments produce shock metamorphism in quartz?
7) Are airburst pressures alone sufficiently high to produce shock metamorphism?

Results and Discussion

Oriented trails of potsherds

Bunch et al. [1] reported linear directionality at Tall el-Hammam for potsherds, charred grains, and bones but presented limited evidence to support that claim. That study attributed the directionality to airburst-related high-velocity winds, modeled at 255 m/s for a 60-m asteroid to 330 m/s for a 75-m asteroid. Our study presents additional evidence supporting this linear directionality from SW to NE across the site. The conclusion about directionality for potsherds, bones, charred grains, charcoal, plaster detritus, and blow-over deposits (Figure 2) is based on 79 site photographs and drawings and ~100 field observations from archaeological Season Reports and the PhD dissertation of co-author

Dr. Silvia [4]. See Figure 2 and **Appendix, *Oriented materials, Table A2*** for further details.

Of the uniquely identifiable potsherds analyzed for this study, ~187 out of 191 (98%) are oriented in groups from ~NNE to ENE (averaging NE). Some clusters contain potsherds from multiple vessels; others are from single vessels (Figures 3–5). Additional examples of directional potsherds are shown in Appendix, Figures A5–A10. As illustrated below, widely separated potsherds from several distinctively decorated pots were found spread narrowly across up to ~22 m of the excavations in an average SW-to-NE direction. The site locations where directional evidence was found are listed below in the **Appendix, *Oriented materials, Table A2*.**

Notably, none were found in contact with the original floor where they were almost certainly placed initially. Instead,
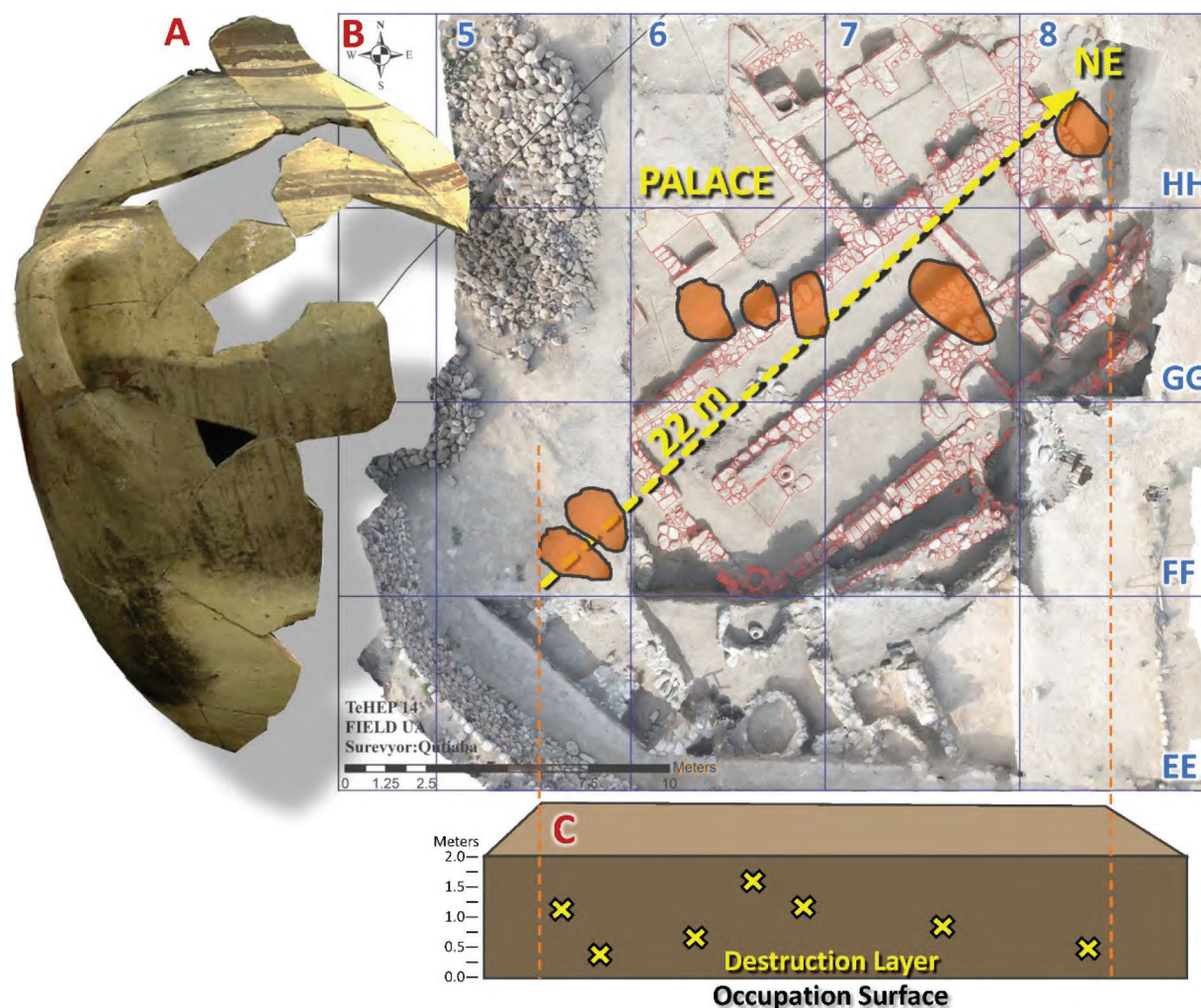
Figure 3: Directionality of potsherds from a single vessel. (A) Palace: a distinctively decorated large vessel partially reconstructed from multiple potsherds. **(B)** An aerial view of the excavation site shows the locations of seven clusters of potsherds from the vessel, as shown in panel A. The sherds were distributed ~22 m across six palace walls in multiple rooms. Also, the potsherds were found on top of some foundations, suggesting the walls no longer stood when the sherds were emplaced. **(C)** This panel represents a side view of the occupation surface. No potsherds from this single distinctively decorated vessel were found in contact with the occupation surface. Instead, all were found "floating" ~0.25 to 1.75 m above the floor and wall foundations within the churned-up terminal destruction layer.
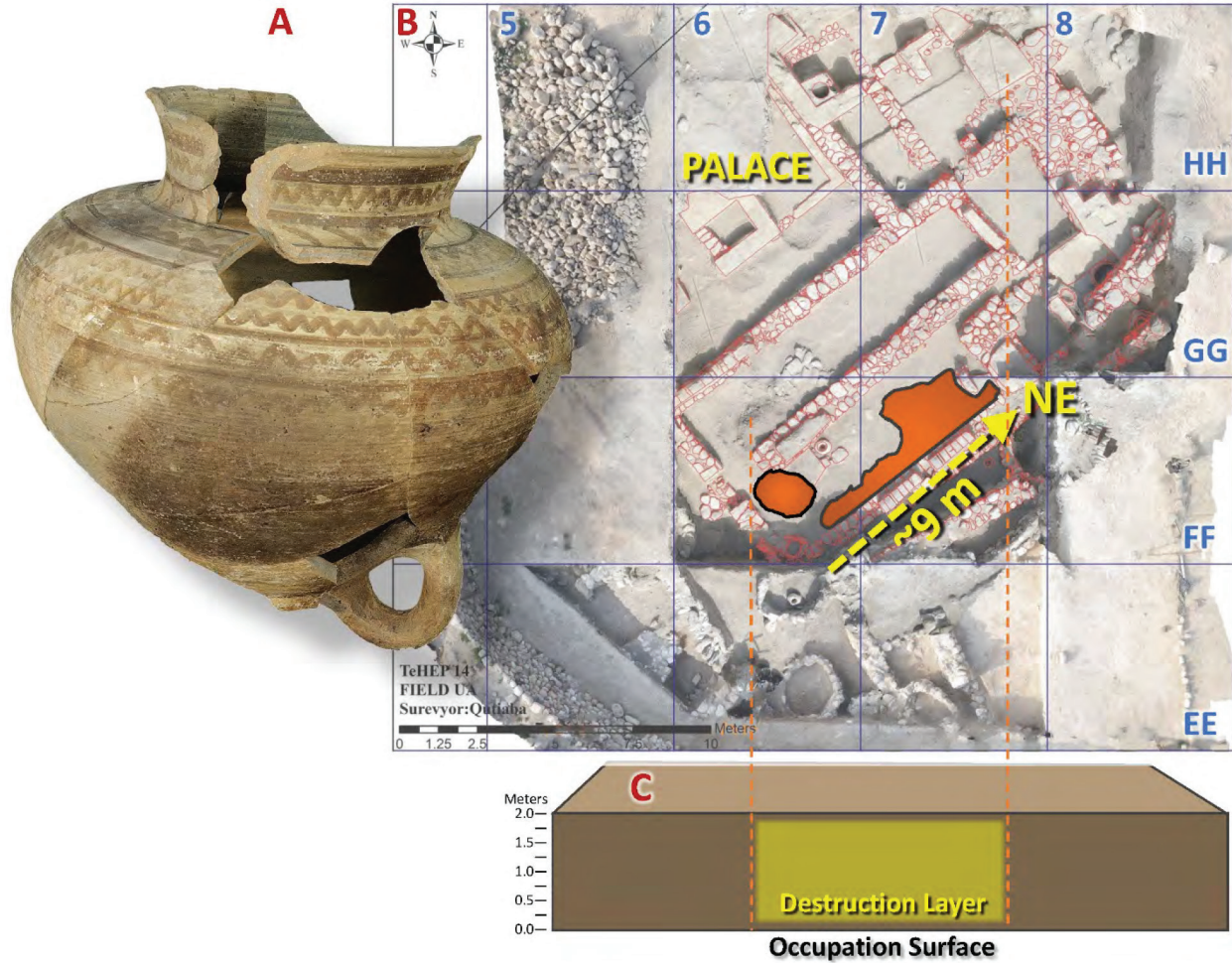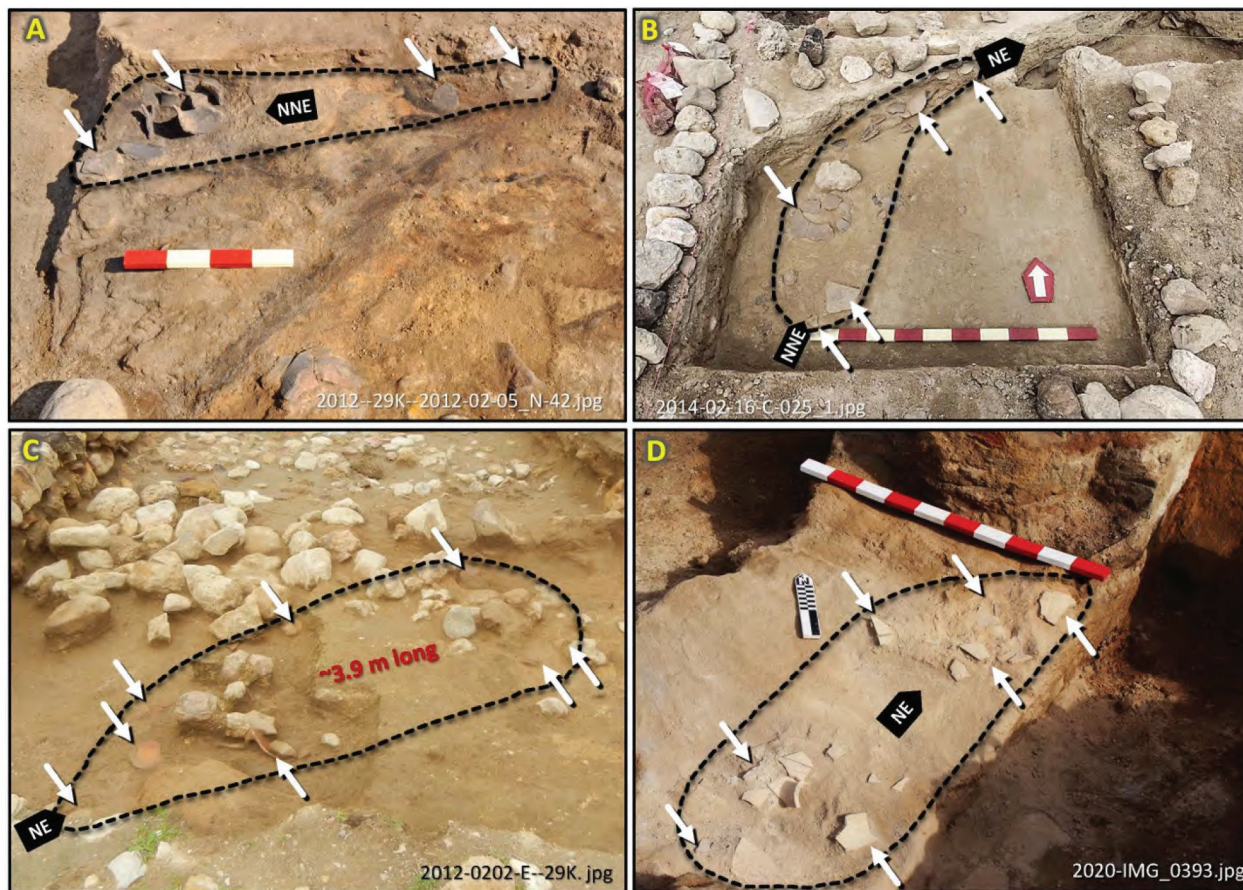
Figure 4: Directionality of potsherds from a single vessel. (A) Palace: ~12 reassembled sherds from a single distinctively decorated large vessel. **(B)** An aerial view of the excavation site shows the potsherds locations from the vessel, as shown in panel A, distributed across ~9 m from SW to NE. They were mixed with ~50 different vessels in three 6×6-m excavation squares and were mingled with charcoal and carbonized grain. **(C)** This panel represents a side view of the occupation surface. No potsherds from this single distinctively decorated vessel were found in contact with the occupation surface on which they were initially placed. Instead, all were found "floating" randomly ~0.25 to 1.75 m above the floor within ~1.5 m of the 2-m-thick churned-up terminal destruction layer (yellow shaded area).

they were suspended at random depths within up to 2 m of a churned-up matrix of potsherds, broken and pulverized mudbricks, meltglass, melted pottery, microspherules, and charred building materials. All potsherds from single vessels were linearly oriented approximately SW to NE (range: approximately ± 25°) (Figures 3–5). We found only a few smaller intact vessels, likely preserved due to their small size or sheltered location. Of the broken ones, we rarely found all the pieces within any given 6×6-m excavated square, i.e., at least some sherds from the same shattered vessel were typically separated by more than 6 m. As discussed in Bunch et al. [1], this situation was unique to the MBA terminal destruction layer and was not evident in any older or younger layers at Tall el-Hammam. This situation is atypical for earthquakes when vessels are locally shattered *in situ* and buried beneath collapsed walls and roofing material.

We drew dashed lines around the clusters and labeled the inferred direction for clarity. Also, for clarity, we often enlarged, cropped, and globally adjusted the photographs' contrast, brightness, and sharpness; they have not been otherwise altered. Most photographs of potsherds display a north arrow, or in other cases, N-S and E-W excavation string lines are visible, allowing us to establish a north direction. In the other cases, directionality was inferred using the time of day recorded in the metadata of the original photographs with sun-shadow software (https://app.shadowmap.org/) to determine the photograph's north compass direction, estimated to be accurate within approximately ± 25°.

To summarize, potsherds from undecorated vessels were rarely found on the original occupation floor and, instead, were found randomly distributed at varying depths within the 2-m-thick terminal destruction layer. For every

Figure 5: Directionality of potsherds. (A) Ring road: a ~1.2-m line of potsherds from a single pot. White arrows indicate some representative examples of directional sherds. **(B)** Ring road: a ~1.2-m trail of potsherds from the single pot, curving along a NE-trending mudbrick wall. **(C)** Ring road: a ~3.9-m long trail of sherds from different vessels mixed with rocks from a fallen wall. **(D)** Palace: a ~1.4-m-long trail of potsherds from a single pot found on top of the foundation of a fallen wall.

distinctively decorated vessel recovered, no potsherd was found in contact with the occupation floor on which they were initially placed. Instead, all were found directionally oriented from SW to NE and "floating" ~0.25 to 1.75 m above the floor and wall foundations within the churned-up terminal destruction layer among numerous other potsherds, broken and pulverized mudbrick, meltglass, melted pottery, microspherules, and charred building materials. Their positions and conditions are inconsistent with emplacement by earthquakes, windstorms, and warfare but are consistent with high-velocity winds produced during an airburst.

### Oriented trails of charred grains and charcoal

Nearly every 6 × 6-m square excavated contained irregular streaks of charred grains and charcoal; an estimated 80% were oriented NNE to ENE, averaging ~NE (Figure 6). Additional examples of directional charred grains/charcoal are shown in Appendix, Figures A11 and A12. Note that this material is commonly visible on the side faces of vertical excavations and on horizontal surfaces. However, directionality cannot be determined from a side view only; it must be

observed from the top down during excavation or as viewed in photographs. The selected photographs below are all approximately top-down views of the ~NE-oriented charred grains and charcoal.

Oriented trails of bones

Numerous small bone fragments were found in every 6 × 6-m square across the site. Most bones were small, so we could not determine whether they were human or animal. However, large, identifiably human bones were rare (Figure 7). The count was ~23 single human bones, for which 7 of 10 groups (70%) were oriented ~NNE to ENE, averaging ~NE ± 25°. The other three groups were oriented ~NW. We infer this to be the expected orientation of bodies exposed to high-velocity winds that tend to orient long objects, such as a body, lengthwise in the direction of least resistance, which in this case is ~SW to NE. Experts in Middle Eastern burial practices confirm that these remains were not emplaced during intentional burials [70]. Instead, all were suspended at random depths within the ~2-m-thick destruction layer among a churned-up matrix of potsherds,
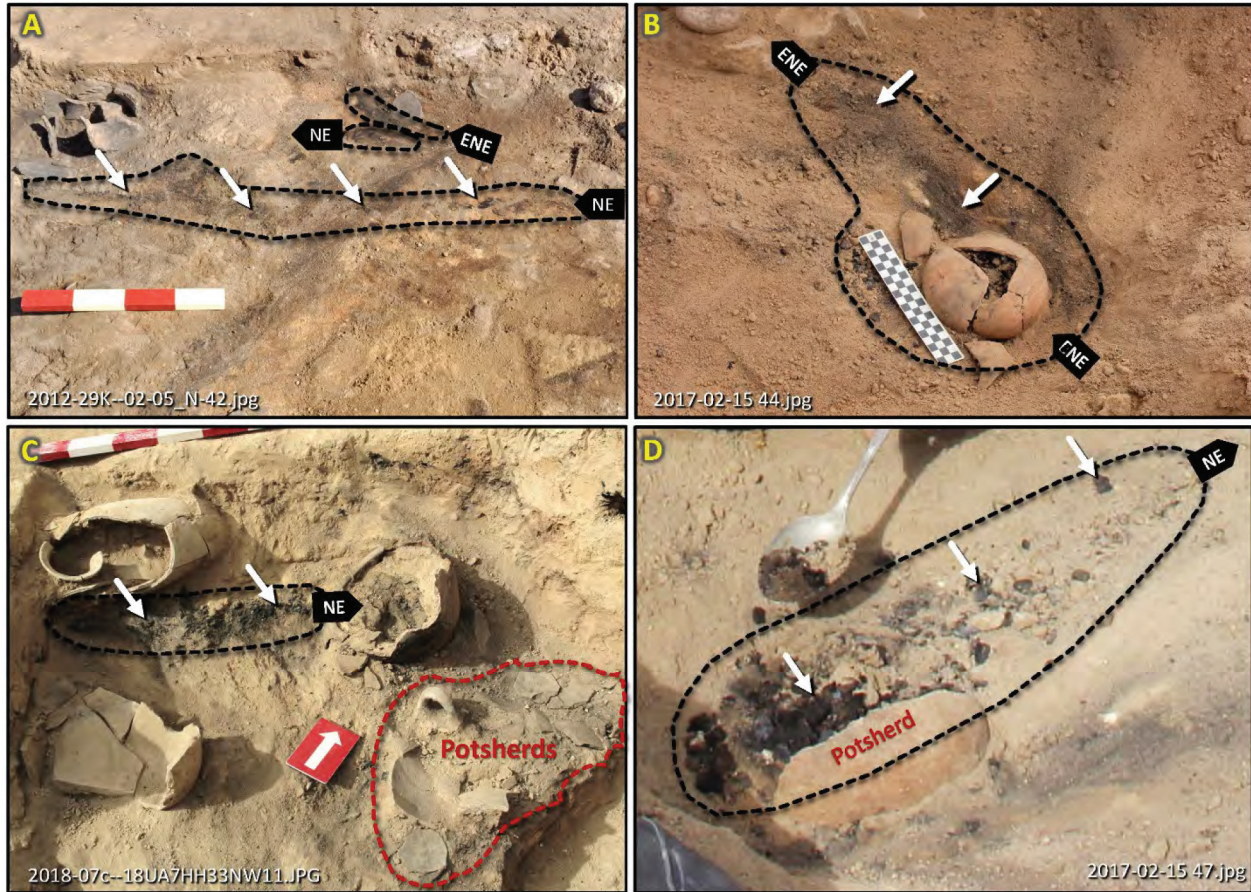
Figure 6: **Directionality of charcoal and charred grains. (A)** Ring road: streaks of charred grains spanning up to 1.1 m (black dashed line with white arrows). **(B)** Palace: ENE-trending ~50-cm-long streak of charred grain that spilled out of broken ENE-trending vessel. **(C)** Palace: ~50-cm-long streak of charred grains among NE-trending potsherds (red dashed line). Panel C is from Bunch et al. [1], usable under Creative Commons, CC by 4.0 (http://creativecommons.org/licenses/by/4.0/). **(D)** Palace: a NE-trending streak of charcoal that spilled out of a broken vessel.

broken and pulverized mudbricks, meltglass, melted pottery, microspherules, and charred building materials. In some cases, broken pieces of the same bone were found within a 6-m radius [70]. In all cases, most bones from any given skeleton were not recovered.

Summary of directionality

The airburst shockwave's energy appears to have been redirected around substantial obstructions, including ramparts, the multi-story palace, foundations, and cross-walls, following the path of least resistance along walls and streets. Thus, although the directionality of debris trended typically SW-NE, the orientation occasionally varied by approximately ± 25° when the shockwave encountered obstacles.

The directionality method used in this study is similar to that used to investigate the airburst at Tunguska, where the compass directions of hundreds of trees were compiled to provide an average local direction. At Tunguska, the tree-fall pattern produced mostly straight lines radiating from ground zero, but there was substantial variation. For groups of trees at four locations, researchers measured blast directions that varied approximately ± 20-35° (Fig. 3 of Florenskiy [84]). Other researchers reported large-scale variations in average tree-fall directions varying by ± 180° from some radial lines (Figs. 4-5 of Florenskiy [84] and Fig. 1 of Longo et al. [85]). These variations at Tunguska are interpreted to have resulted from turbulent convection cells within the shockwave and from deflection by topographical features, such as hills and streambeds. This effect is similar to what is inferred from obstructions within Tall el-Hammam.

Brecciated melt rock

Breccia is a rock typically composed of angular fragments of minerals or rocks cemented together by a fine-grained matrix. Sedimentary and metamorphic processes can produce breccia, but if its matrix is melted, breccia is typically associated with high-energy, high-velocity crater-forming impact events [86–89] and touch-down airbursts [22, 32].
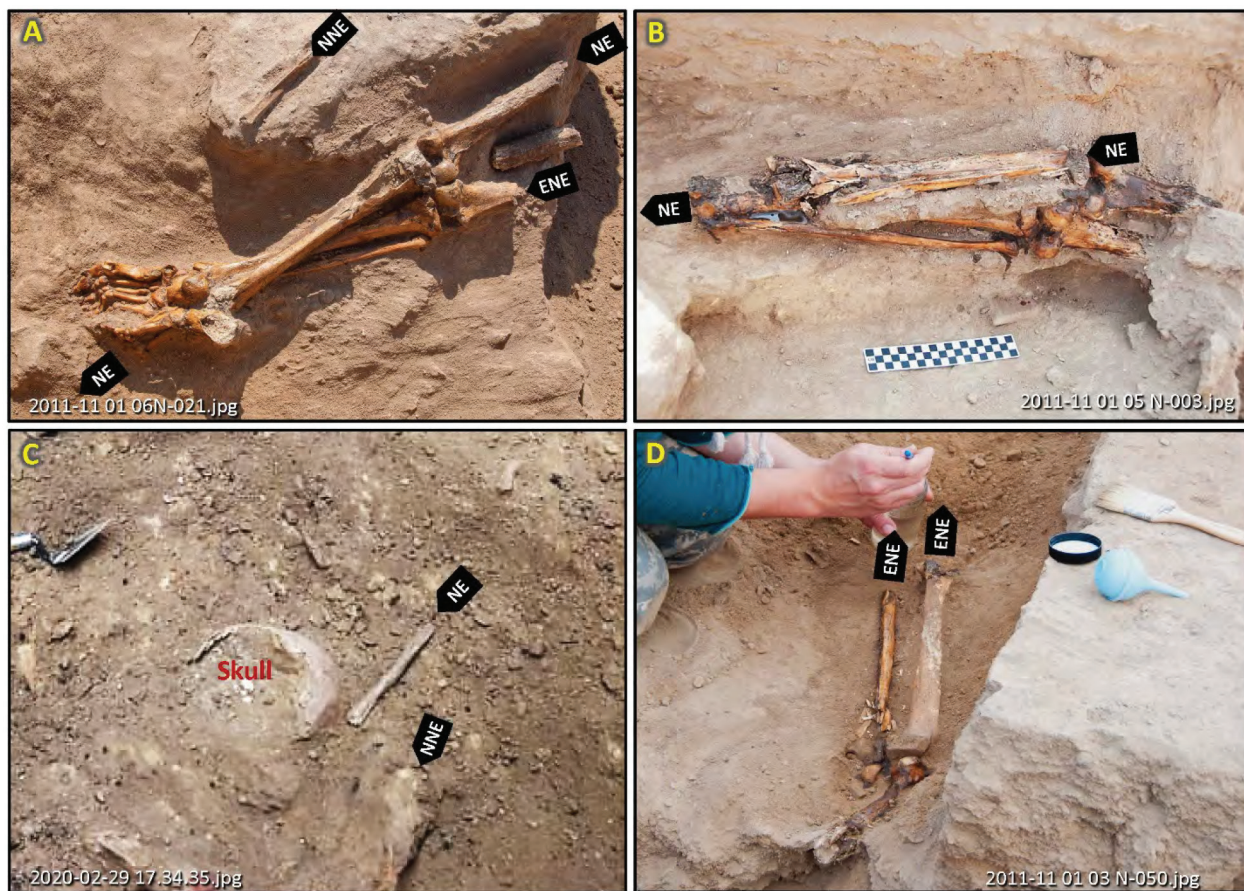
Figure 7: **Directionality of bones and skeletons. (A)** Ring road: the sun's shadow is from the south (top), indicating a SW-NE direction. **(B)** Ring road: the edge of the N-S excavation is to the right, confirming the NE alignment of bones. **(C)** Palace: disarticulated skull and bones. The sun's shadow is from the SE, upper left, confirming a SW-NE alignment. **(D)** Ring road: two disarticulated legs and foot bones are oriented ENE. Panels A and C are from Bunch et al. [1], usable under Creative Commons, CC by 4.0. (http://creativecommons.org/licenses/by/4.0/).

Dr. Ted Bunch, lead author of the previous Tall el-Hammam study [1], prepared the following analysis of the brecciated melt rock for this manuscript before he passed away. In 2010, a fine-grained brecciated melt rock measuring 19 cm wide and weighing 672 g (Figure 8) was discovered ~9 km SW of Tall el-Hammam at the site of a small abandoned village now called Tall Mwais. Although this site remains unexcavated, numerous Middle Bronze Age (MBA) potsherds were exposed at the surface in unconsolidated sand. The melt rock was found adjacent to the foundation of an MBA stone wall and surrounded by MBA potsherds in close association. No pottery from any other archaeological period was associated with the breccia, and post-depositional disturbance at the site appeared minimal. This archaeological association suggests the breccia is contemporaneous with the MBA terminal destruction layer at Tall el-Hammam, which contains the same types of potsherds. Although the provenance of this breccia cannot be accurately established, its complex melt attributes and structure are consistent with some type of impact event during the Middle Bronze Age.

Future research is needed to search for breccia and other impact-related materials in well-stratified contexts at this site and others within a few km of Tall el-Hammam.

Lithological and petrological analyses were performed to explore the possibility of impact-related melting. The fine-grained brecciated melt rock comprises a matrix of melted and unmelted sandy limestone mixed with rounded clasts mainly of quartz and sandstone. The breccia displays unmelted and partially melted fine-grained quartz grains, gypsum, and carbonates that are common in the region near Tall el-Hammam. For major elements, the bulk composition of the breccia averages 62.0 wt% SiO_2, CaO at 10.1 wt%, and Al_2O_3 at 14.0 wt%.

The melt rock displays three distinct morphologies, designated as Lithologies A, B, and C. Lithology A (Figure 8B, 8E) has a fine granular texture of partially melted and fused grains, mainly quartz, that is almost entirely coated with a glossy veneer of melted SiO_2. The top of the melt rock is composed almost entirely of lithology A with a thin-to-thick veneer of melted, shiny glass covering
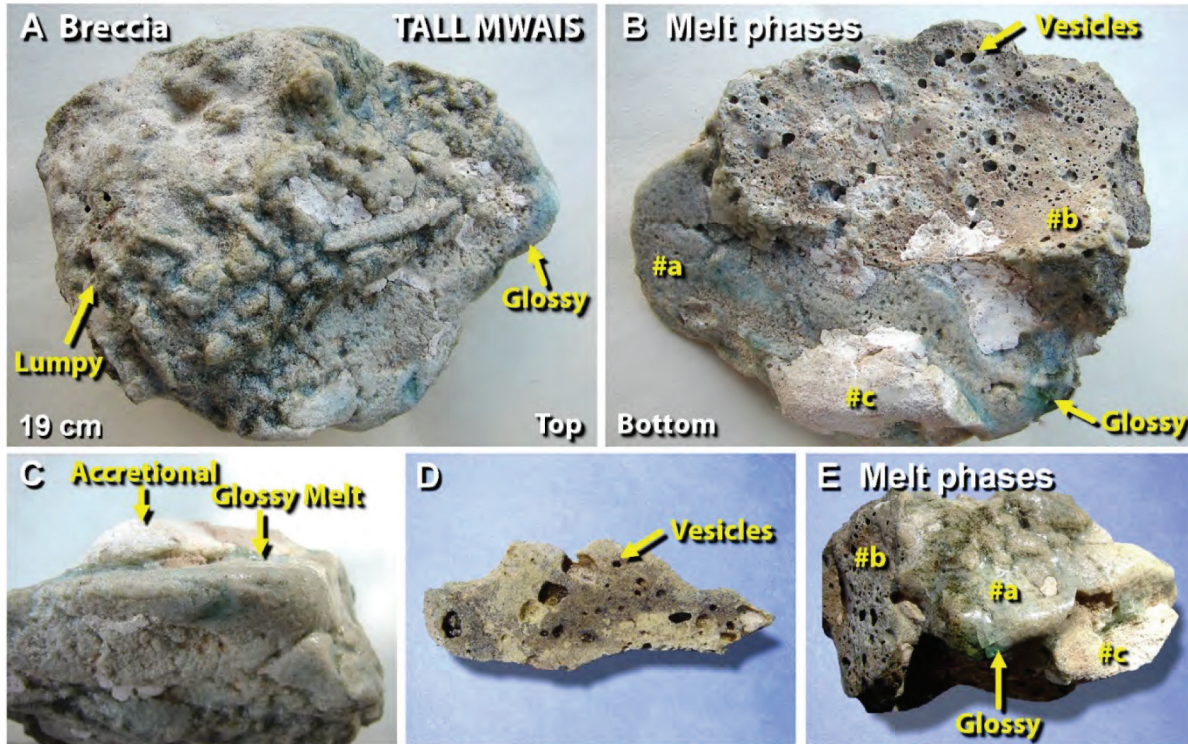
Figure 8: **Brecciated melt rock from Tall Mwais, ~8.5 km SW of Tall el-Hammam. (A)** Top view of the 672-g piece of breccia; **(B)** bottom view of the same melt rock. Note the locations of lithologies marked as #a, #b, and #c. **(C)** The side of the melt rock shows a glass-like melted surface and accretional feature. The green color is typical of melted quartz sand, and the white area is melted gypsum and carbonates. **(D)** Cut surface of melt rock slice, showing numerous vesicles formed by gas trapped as the molten rock rapidly cooled; **(E)** another image of the glossy, glass-like melted surface, showing various lithologies, marked as #a, #b, and #c.

most of the upper surface and sides. The raised points of the surface are thinly covered with glass, and the lower areas are thickly covered, indicating that the glass flowed at very low viscosity. Lithology A material appears composed of partially molten debris fragments that were lightly stuck together before being firmly welded by exposure to very high temperatures. This glass has a hardness of >6.5 on the Mohs scale and is almost optically clear, consistent with the melting of orthoquartzite.

The bluish-to-greenish color of most of the glass coating likely results from mixing melted quartz with trace elements, e.g., Ni or Cu. During melting, red ferric Fe (Fe_3O_4) reduces to a blue-green color when combined with a small amount of Fe_2O_3 (<0.5 wt%). This coloration occurs only under very low oxygen fugacity (minimal O_2 availability), which is rare under typical geological conditions. However, it is common in high-temperature, flash heating/melting events, including atomic detonations (trinitite), lightning strikes (fulgurites), and cosmic impacts.

Lithology B (Figure 8B, 8E) occurs mainly on the basal surface of the Tall Mwais breccia and shows evidence of fracturing. It is darker than lithology A and lacks a glassy coating. This lithology is composed of a mixture of gypsum, quartz grains, and clasts of orthoquartzite sandstone, and it

displays numerous large, deep, irregular vesicles, some of which are tube-like, with the remainder being bubble-like. These vesicles most likely were produced during the rapid outgassing of H_2O and SO_x gases, the rapid thermal decomposition of gypsum and carbonates, and the vaporization of trapped pore water. Although pure carbonates decrepitate under gradual exposure to high temperatures (i.e., break into small flakes), they can melt if exposed to temperatures greater than 1500 °C for a few seconds, followed by rapid quenching [1]. However, impure carbonates can melt at lower temperatures.

Lithology C (Figure 8B, 8E) is composed of white, partially melted glass that is fused to the larger melt rock (Figure 8C). This lithology appears as a clump of ortho-quartzite sandstone that is fritted (viscous from heating but not completely melted). The material appears to have fallen onto the still-molten surface glass of lithology A with only partial melting at the margins.

In the breccia from Tall Mwais, we also observed zircon grains with multiple phases that display varying degrees of melting (Figure 9A, 9B) and *in situ* fracturing (Figure 9C, 9D). These breccia zircons are similar to those previously reported by Bunch et al. [1] from Tall el-Hammam in melted pottery and melted mudbricks. Additionally,
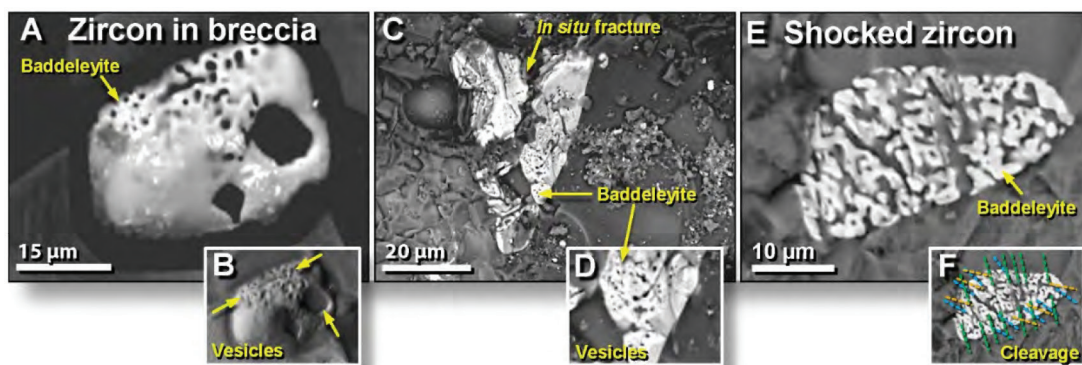
Figure 9: **SEM images of melted zircon grains in melt rock from Tall Mwais. (A)** A melted zircon grain from the Tall Mwais brecciated melt rock shows large vesicles produced by the melting of the grain; **(B)** SEM topographical image of the same grain. **(C)** Distorted, fractured zircon grain, most likely produced *in situ* by thermal or mechanical shock; **(D)** close-up of the vesicular surface caused by temperatures high enough to boil the zircon. **(E)** Possibly shock-metamorphosed zircon grain with three sets of potential shock lamellae (crystalline lattice) as indicated in the inset (F). Bohor et al. [90] showed images of impact-shocked zircons from the K-Pg impact event at 66 Ma that are morphologically indistinguishable from those at Tall Mwais.

one zircon shows signs of potential shock metamorphism (Figure 9E, 9F).

SEM-EDS analyses confirmed that zircons in the breccia show enrichments in baddeleyite (ZrO_2), displayed as bright areas distributed across the grains (Figure 9A, 9C, 9D). In several samples from the terminal destruction layer at nearby Tall el-Hammam, Bunch et al. [1] observed zircons with reduced SiO_2 concentrations due to a loss of volatile SiO resulting from the dissociation of SiO_2. This alteration occurs at high temperatures of ~1676 °C, slightly below zircon's melting point of ~1687 °C [91], thus forming distinctive granular textures of pure ZrO_2 known as baddeleyite [90]. At Tall el-Hammam, Bunch et al. reported that nearly all zircons observed on the surfaces of melted materials showed some conversion to baddeleyite, as do the zircons in the Tall Mwais breccia.

All zircon grains observed were also vesiculated, indicative of outgassing, likely caused by the dissociation of SiO_2 during high-temperature melting and boiling. Vesicular (i.e., decorated) zircon grains are uncommon in nature, but they are commonly associated with cosmic impact events [1], as evidenced by vesicular zircons from the known airburst/impact at Dakhleh Oasis, Egypt, and the proposed airburst at the Younger Dryas boundary at Abu Hureyra, Syria [47]. The bubbles indicate that temperatures reached at least 1676 °C, causing the zircon to outgas and dissociate. Similar dissociated zircon grains have been found in glass and distal fallback ejecta from the ~180-km-wide K-Pg impact crater in Mexico [92] and the 28-km-wide Mistatin Lake crater in Canada [92].

The zircon evidence suggests exposure to extreme temperatures >1676 °C for an inferred duration of less than several seconds, during which these grains began to melt, outgas, and disassociate into baddeleyite. However, because this brecciated melt rock is partially vesiculated and shows

low-viscosity flow, it was most likely exposed to transient temperatures >2230 °C, the boiling point of quartz. These temperatures are within the range modeled for this experiment.

Glass-filled, shock-fractured quartz grains
Shock metamorphism in quartz

This section is adapted from West et al. [9] Multiple studies have investigated various types of impact-related shock metamorphism in quartz, including planar deformation features (PDFs) [10, 18, 93–103] and planar fractures (PFs) [10, 102, 104]. Both types of lamellae are typically parallel, planar, less than a few microns wide, spaced a few microns apart, and crystallographically controlled. These lamellae are also commonly filled with non-hydrated amorphous silica [10], considered diagnostic of impact-cratering events [105]. In contrast, natural fractures in quartz and non-impact-related tectonic deformation lamellae (DLs) are typically non-parallel, non-planar, and contain no non-hydrated amorphous silica [9, 10, 47, 95, 96, 98, 101, 102, 106–110].

Some studies of cosmic impact structures have described another type of lamellae resulting from impact shock metamorphism and given them various names, including vermicular (i.e., wormlike) microfractures [111–113], shock extension fractures (SEFs) [111, 112, 114, 115], and shock fractures [108, 116]. These shock fractures are intragranular cracks in quartz grains that are typically sub-parallel, sub-planar, greater than a few microns wide, spaced more than a few microns apart, not crystallographically controlled, and may or may not contain amorphous silica [9, 10, 17, 18, 20, 53, 117–121]. Here, we follow previous studies [9, 10, 46, 121] and adopt the term "shock fractures" to denote microfractures in quartz produced by thermal and mechanical shock. This study focuses only on the subset of

shock fractures that contain amorphous silica (a term we use interchangeably with "glass").

Origin of glass-filled shock fractures

Shock-metamorphic, glass-filled fractures differ from classical shock lamellae. Buchanan et al. [113] wrote *"Vermicular quartz* [i.e., glass-filled, shock-fractured quartz], *which apparently is composed of near-planar lamellae of silica glass in a host of crystalline quartz, suggests either formation by melting due to extremely high ambient temperatures (~1610 °C) or by shock melting."* Kieffer et al. [118] reported glass-filled shock-fractured quartz grains from Meteor Crater that differed from classical shock lamellae. To explain these, they proposed a process called "jetting," in which molten quartz is injected under high pressure into shock-generated fractures in the grains. Wakita et al. [122] also observed that during the early stages of an impact, molten material might be jetted when the impactor contacts target rocks. Similarly, Ernstson [119, 120] observed that target rocks and grains may fracture from thermal shock and spallation (i.e., tensile fracturing), which occurs *"where the expanding compressive shock front superimposes with the tensile rarefaction waves starting from reflection at the free surface of the impacted target."* [120], during which the stress on the target materials from the rarefaction wave exceeds their tensile strength and, thus, produces fractures. If the shock pressures are sufficient to melt or vaporize the target material, silica vapor or melt can be injected into the fractures.

Previous investigations of shock-fractured quartz

One previous study focused on the Trinity atomic airburst and on Meteor Crater [10]. The other two studies focused on the airburst event at the Younger Dryas boundary (YDB) at Abu Hureyra, Syria [46] and at three sites in South Carolina, Maryland, and New Jersey along the Eastern Seaboard of the USA [121]. All three studies presented evidence and a protocol for identifying glass-filled, shock-fractured quartz associated with airbursts. Their key conclusion is that quartz fractures filled with melted silica strongly indicate shock metamorphism at pressures approximately >1 GPa (= ~10,197 kg/cm^2), whether from an airburst or a typical crater-forming impact.

Although similar evidence for Tall el-Hammam was presented by Bunch et al. [1], Jaret and Harris [123] contend that Bunch et al. did not follow well-established techniques and failed to provide convincing evidence of classically shocked quartz at Tall el-Hammam. Here, we explore whether the evidence suggests the formation not of classical, high-pressure shocked quartz but rather glass-filled, shock-fractured quartz, which is different. For our study, we present new evidence acquired using ten analytical techniques, as listed below. We attempted to use the universal stage, a standard technique for identifying classical shock metamorphism; this is one of the deficiencies claimed for Bunch et al. [1] by Jaret and Harris. However, we found it unsuitable because the glass-filled fractures observed at Tall el-Hammam are typically sub-parallel and sub-planar, so the fractures' angles and inclinations could not be accurately measured with a universal stage.
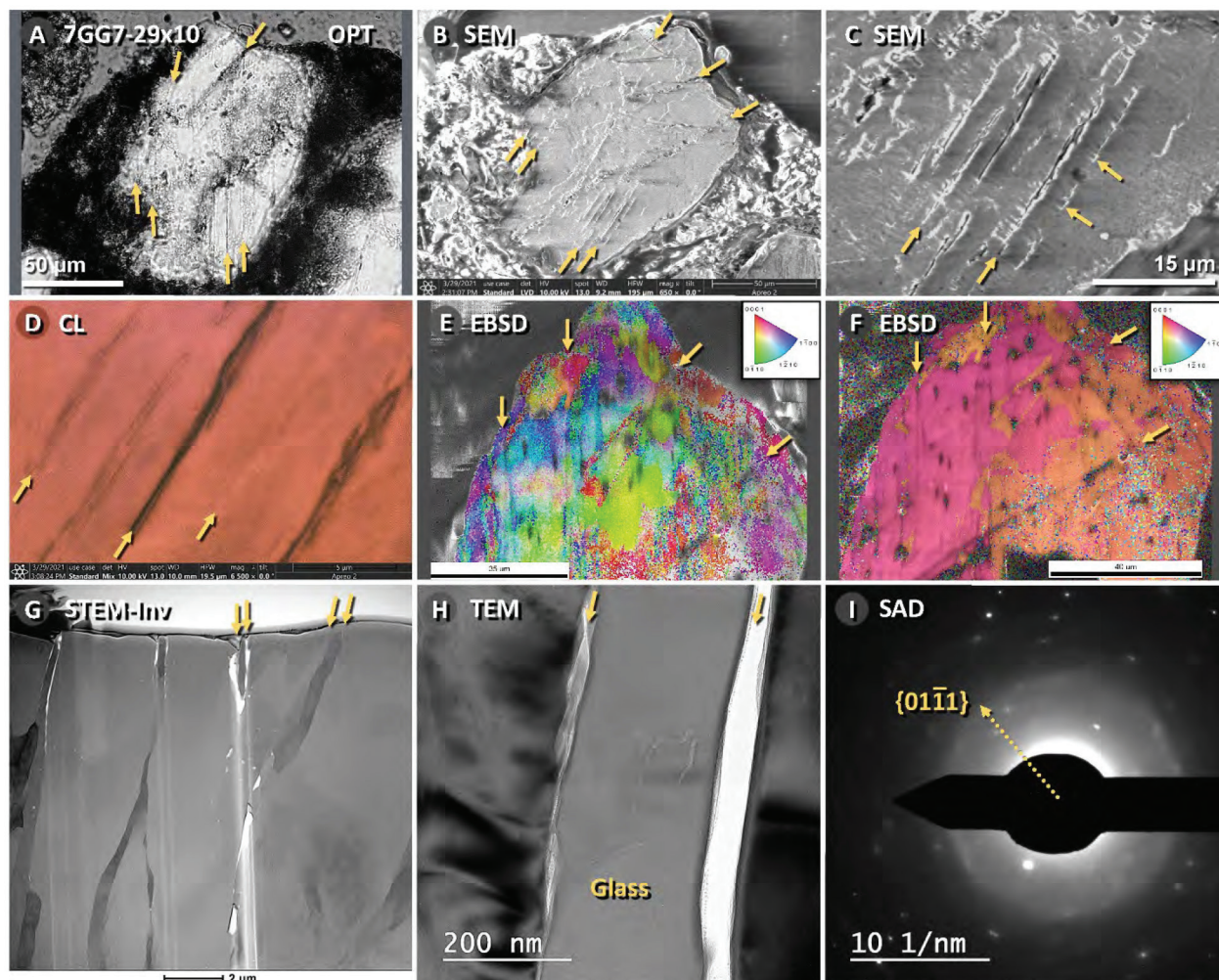
Identifying shock-fractured quartz

Bunch et al. [1] and Hermes et al. [10] cited multiple studies concluding that glass-filled lamellae in quartz grains are evidence of impact-related shock metamorphism. Thus, a crucial part of this study involves identifying those quartz fractures filled with melted silica, and we report that all the quartz grains reported here contain amorphous silica within their fractures. To reach that conclusion, we used the following ten techniques:

1) EPI-illumination microscopy (EPI) can show whether a fracture is filled but does not show whether or not the material is amorphous.
2) Optical transmission microscopy (OPT) uses crossed polarizers to determine whether parts of a quartz grain are isotropic (i.e., they remain dark during rotation) and are likely to be amorphous.
3) Scanning electron microscopy (SEM) can determine whether fractures are filled but does not determine the material's composition.
4) Energy dispersive spectroscopy (EDS) can determine the composition of any material filling the fractures, e.g., amorphous silica, hydrated silica, other minerals, or polishing compounds.
5) Focused ion beam milling (FIB) was used to create thin slices of quartz grains for use in the TEM to investigate crystallinity.
6) Transmission electron microscopy (TEM) was used to determine whether fractures are filled with material and which areas are amorphous.
7) Scanning transmission electron microscopy (STEM) was used to determine whether fractures are filled with material.
8) Selected area diffraction (SAD), fast-Fourier transform (FFT), and inverse fast-Fourier transform (IFFT) are TEM techniques used to generate diffraction patterns that show which parts of a quartz grain are amorphous.
9) Cathodoluminescence (CL) was used to determine which parts of a quartz grain are crystalline or amorphous. Non-luminescent (black) areas indicate the presence of amorphous silica.
10) Electron backscatter diffraction (EBSD) was used to determine which parts of a quartz grain are amorphous and the degree to which the crystalline lattice has been damaged by shock.

Our study explores the characteristics of the glass-filled quartz fractures observed by Bunch et al. in the terminal destruction layer in the palace and temple. Importantly, we also investigate whether the characteristics of these fractured quartz grains differ from those of classically shocked quartz. Abundant new evidence is presented in Figures 10–14 below.
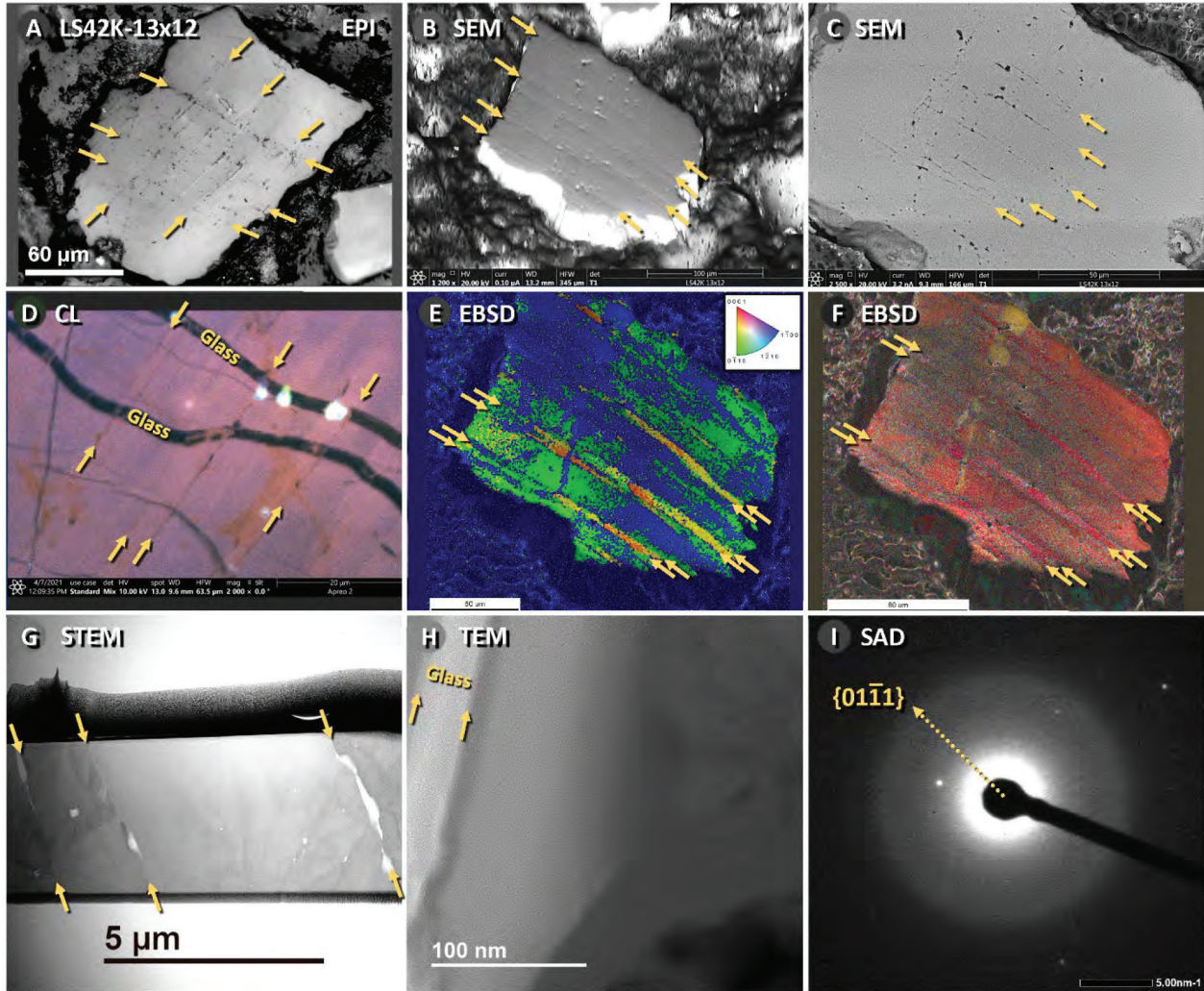
Figure 10: Shock-fractured quartz grain from the palace. All images are from grain 7GG7-29×10. **(A)** Cross-polarized optical photomicrograph of the shock-fractured quartz grain. Yellow arrows indicate visible shock-fractured lamellae in this grain and the following panels. Three sets of differently oriented lamellae are apparent. Amorphous silica remains dark during rotation under crossed polars. **(B)** SEM image of the quartz grain. **(C)** Close-up SEM image showing two sets of lamellae. Note the short feather-like lamellae, indicative of low-pressure shock-fractured quartz [1, 124]. **(D)** Cathodoluminescence (CL) image showing oriented lamellae. Darker linear features represent fractures filled with melted silica (glass), an indicator of shock metamorphism [10, 46]. **(E)** Electron backscatter diffraction (EBSD) image. Dark linear features, marked by arrows, indicate lamellae filled with melted silica. The range of colors represents minor crystalline lattice dislocations caused by shock metamorphic damage to the grain [10, 46]. The legend of color-coded Miller-Bravais indices is at the upper right. **(F)** EBSD image of the same grain, where the two colors represent Dauphine twinning, commonly observed in shock-fractured quartz grains [10, 46]. **(G)** Scanning-transmission electron microscope (STEM) image (inverted color). Darker features at the arrows are sometimes bounded by lighter borders, representing sub-parallel and sub-planar shock lamellae [10, 46]. Note that glass-filled fractures are non-planar and non-parallel, unlike classical shock lamellae, and, therefore, cannot be indexed with a universal stage. **(H)** Transmission electron microscope (TEM) close-up image showing a lamella infilled with melted silica (glass) and bounded by open fractures (light-colored bands). **(I)** The selected area diffraction (SAD) pattern was acquired from the region in panel 'H.' The bright diffuse ring indicates the presence of melted silica within an area that includes crystalline quartz, indicated by bright spots. The outer border of the diffuse halo corresponds to the $\{01\bar{1}1\}$ diffraction line of quartz. Panels C, E, and F are from Bunch et al. [1], usable under Creative Commons, CC by 4.0 (http://creativecommons.org/licenses/by/4.0/).

Due to the tectonic nature of Tall el Hammam's geologic province, we considered whether the fractured quartz grains could be tectonic in origin, superficially resembling shock-fractured quartz. However, multiple investigations [9, 10, 46, 121] observed that they can be differentiated using two major distinguishing characteristics, which must co-occur: (i) Shock--fractured quartz typically displays open fractures, i.e., open gaps between the sidewalls, and at the same time, (ii) the fractures are filled with non-hydrated melted silica. These two characteristics are never observed in tectonic quartz, where fractures are closed crystalline dislocations and are not filled with melted silica. Thus, the glass-filled, shock-fractured quartz grains found at Tall el-Hammam are not tectonic in origin and, instead,
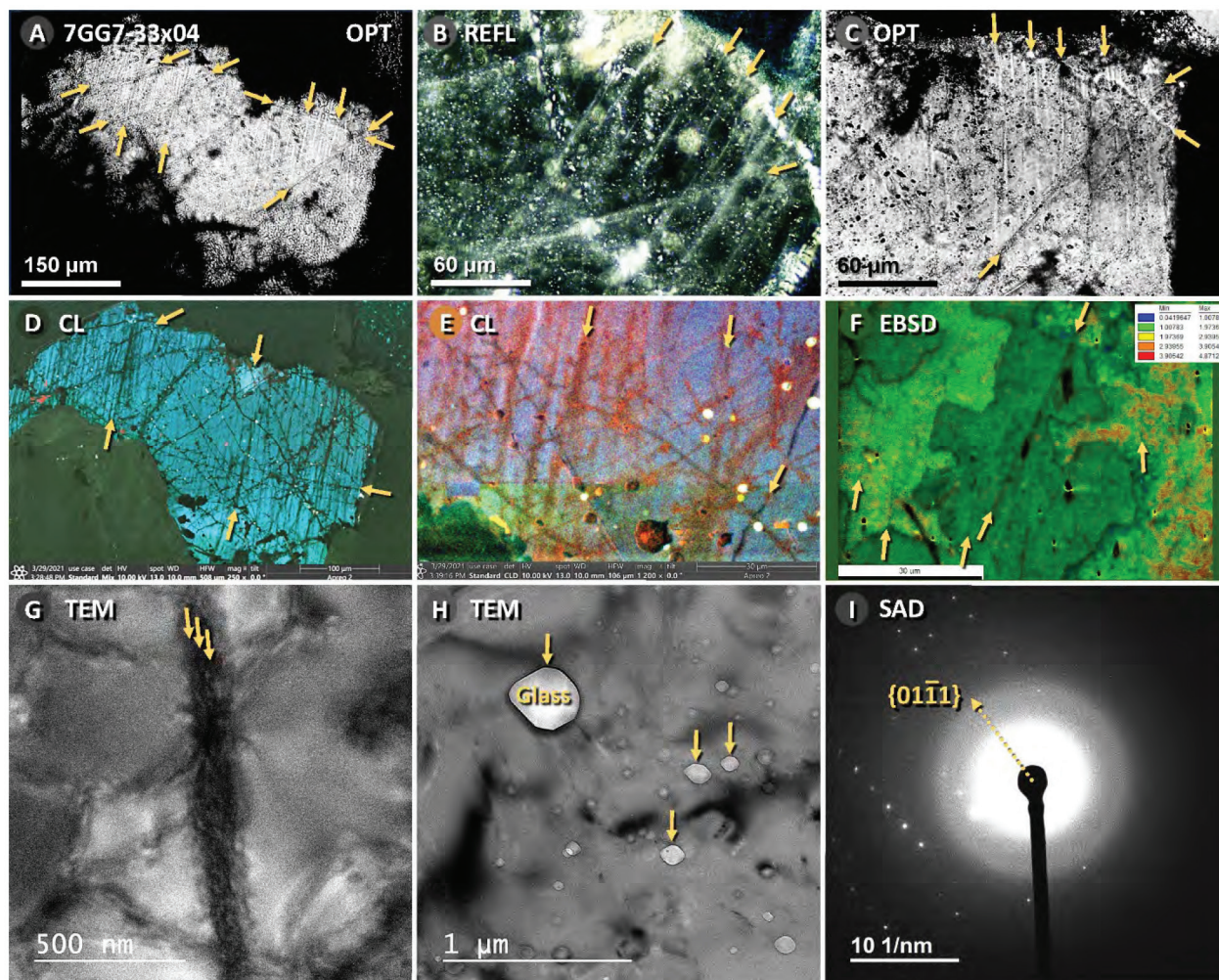
Figure 11: **Shock-fractured quartz grain from the temple complex.** All images are from grain LS42K-13×12. **(A)** Epi-illuminated photo-micrograph of shock-fractured quartz grain. Yellow arrows indicate visible shock-fractured lamellae here and in the following panels. Two sets of differently oriented lamellae are apparent. **(B)** EBSD-SEM image of the quartz grain. **(C)** Close-up SEM image of lamellae, indicative of shock-fractured quartz [1, 124]. **(D)** Cathodoluminescence (CL) image displaying oriented lamellae. Darker linear features represent open fractures filled with melted silica (glass), an indicator of shock metamorphism [10, 46]. **(E)** Electron backscatter diffraction (EBSD) image. Linear features at arrows indicate lamellae infilled with melted silica. They appear as "twins" but are not of the Dauphine variety. The wide range of colors represents crystalline lattice dislocations caused by shock metamorphic damage to the grain [10, 46]. **(F)** EBSD image in which the two colors represent Dauphine twinning, commonly observed in shock-fractured quartz grains [10, 46]. **(G)** Scanning-transmission electron microscope (STEM) image (inverted color). The darker features at the arrows, bounded in some cases by light borders, represent sub-parallel, sub-planar shock lamellae [10, 46]. Note that glass-filled fractures are non-planar and non-parallel, unlike classical shock lamellae, and, therefore, cannot be indexed with a universal stage. **(H)** A close-up transmission electron microscope (TEM) image shows a lamella at arrows filled with melted quartz (glass). **(I)** This selected area diffraction (SAD) image was acquired in the region in panel 'H.' The bright diffuse ring indicates the presence of melted silica within an area that includes crystalline quartz, indicated by bright spots. The outer border of the diffuse halo corresponds to the $\{01\bar{1}1\}$ diffraction line of quartz. Panels 'A' and 'D' are from Bunch et al. [1], usable under Creative Commons, CC by 4.0 (http://creativecommons.org/licenses/by/4.0/).

are consistent with shock-fractured quartz grains previously reported in touch-down airbursts [9, 46, 121]. However, they differ from classically shocked quartz grains produced in typical cratering impacts [10], mainly because the fractures are sub-parallel and sub-planar, as observed in proposed airbursts [46, 121].

We also considered whether the amorphous silica within the fractures might be hydrated silica ($SiO_2 \cdot H_2O$), a common mineral that forms when dissolved quartz is deposited within grain fractures. To investigate this possibility, we analyzed the silica in all fractured grains and determined that none is composed of hydrated silica. The melted silica we observed

Figure 12: Shock-fractured quartz grain from the palace. All images are from grain 7GG7-33×04. **(A)** Cross-polarized optical photomicrograph of shock-fractured quartz grain. Yellow arrows indicate visible shock-fractured lamellae here and in the following panels. Three sets of differently oriented lamellae are visible. **(B)** Reflected-light close-up photomicrograph. **(C)** Close-up cross-polarized optical photomicrograph showing three sets of shock-fractured lamellae. **(D)** Cathodoluminescence (CL) image showing oriented lamellae. TEM imaging shows that some black linear features represent open fractures, while others contain melted silica (glass), an indicator of thermal or mechanical shock metamorphism [10, 46]. **(E)** Another CL image also displays red and dark linear features indicative of melted silica [10, 46]. **(F)** Electron backscatter diffraction (EBSD) image. Linear features at arrows indicate lamellae infilled with melted silica. The range of colors represents crystalline lattice dislocations caused by shock metamorphic damage to the grain [10, 46]. Dark green represents minimal damage, ranging to red, indicating substantial damage. **(G)** TEM image. Multiple dark linear features at the arrows represent sub-parallel and sub-planar shock lamellae [10, 46]. **(H)** A close-up transmission electron microscope (TEM) image shows numerous vesicles infilled with melted quartz (glass). **(I)** This selected area diffraction (SAD) image was acquired in the region in panel 'H'. The bright diffuse ring indicates the presence of melted silica within the large vesicle, surrounded by crystalline quartz, indicated by the bright spots. The outer border of the diffuse halo corresponds to the {01$\bar{1}$1} diffraction line of quartz. Panel 'D' is from Bunch et al. [1], usable under Creative Commons, CC by 4.0 (http://creativecommons.org/licenses/by/4.0/).

has stoichiometric EDS ratios for Si:O (~47:53 wt%) consistent with melted quartz and inconsistent with hydrated silica, which typically contains ≥60 wt% oxygen. Thus, we conclude that the melted quartz observed in some fractured quartz grains from Tall el-Hammam is best explained as resulting from a high-temperature, high-velocity airburst event.

In summary, we investigated three layers from the palace and temple: one sample in each area taken from within, immediately above, and immediately below the terminal destruction layer. We observed glass-filled, shock-fractured quartz only in the terminal destruction layer, suggesting that a high-pressure, high-temperature event occurred when that layer was deposited around 3600 years ago.

Hydrocode modeling of a 55-m asteroid
Hydrocode modeling is commonly used for impact simulations [5, 9, 11, 125–131], and specifically, Autodyn-2D, a
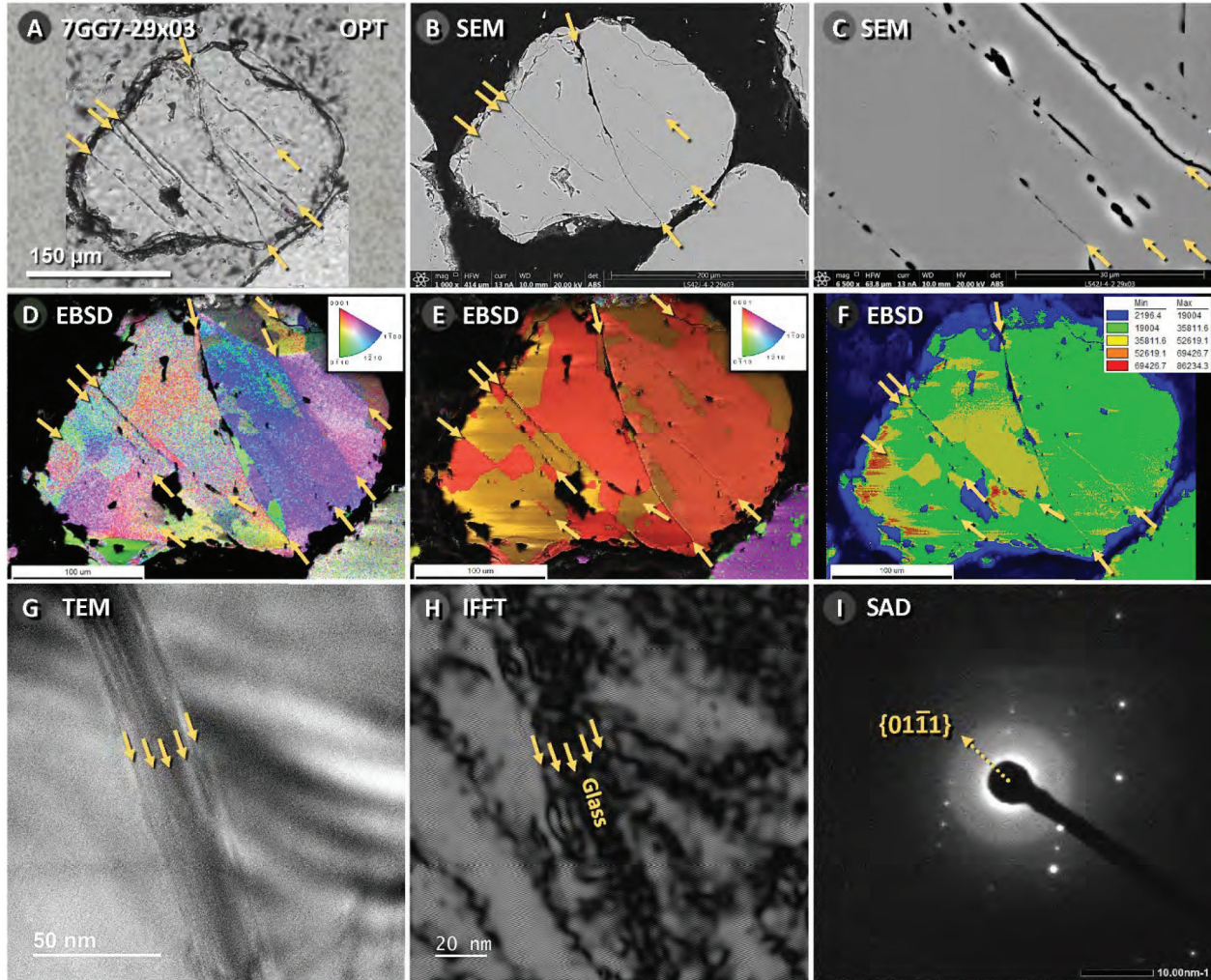
Figure 13: Shock-fractured quartz grain from the palace. All images are from grain 7GG7-29×03. **(A)** Cross-polarized optical photomicrograph of shock-fractured quartz grain. Yellow arrows indicate visible shock-fractured lamellae here and in the following panels. One set of lamellae is visible. **(B)** Scanning electron microscope (SEM) image of the same grain. **(C)** Close-up SEM image showing shock-fractured lamellae. Note that glass-filled fractures are non-planar and non-parallel, unlike classical shock lamellae, and, therefore, cannot be indexed with a universal stage. **(D)** Electron backscatter diffraction (EBSD) image. Linear features at arrows indicate lamellae infilled with melted silica (glass). The range of colors represents crystalline lattice dislocations caused by shock metamorphic damage to the grain [10, 46]. **(E)** Another EBSD image where the two colors indicate the presence of Dauphine twinning, an indicator of shock metamorphism [10, 46]. **(F)** EBSD image. The range of colors represents crystalline lattice dislocations caused by shock metamorphic damage to the grain [10, 46]. Green represents minimal damage, ranging to red, signifying high damage. **(G)** Transmission electron microscope (TEM) image. Multiple dark linear features at the arrows represent sub-parallel and sub-planar shock lamellae [10, 46]. **(H)** Inverse Fast Fourier transform (IFFT) image. Dark areas represent substantial grain damage, indicative of melted silica (glass); light gray areas represent minimal to no damage to the crystalline lattice. **(I)** This selected area diffraction (SAD) image was acquired in the region in panel 'H.' The bright diffuse ring indicates the presence of melted silica within the large vesicle, surrounded by crystalline quartz, indicated by the bright spots. The outer border of the diffuse halo corresponds to the $\{01\bar{1}1\}$ diffraction line of quartz.

hydrocode program from Ansys, Inc., has seen widespread use [127, 132–144]. In the current study, we first modeled the Tall el-Hammam airburst using the Earth Impact Effects Program (EIEP) developed by Marcus et al. [145] and Collins et al. [129, 130] Second, we input the EIEP results into Autodyn-2D (Ansys, Inc.), a hydrocode software program commonly used for modeling high-velocity airbursts and impacts [5, 11, 125–143]. For more information, see **Appendix,** *Autodyn modeling*, **Appendix,** *Testing the accuracy of modeling*, **Appendix,** *Previous modeling of airbursts* below.

The temperatures modeled in this study are not fully quantitative because of the inherent difficulties in accurately determining extreme temperatures under highly chaotic conditions. The Autodyn program can account for the kinetic energy, strain energy, and contact energy but does
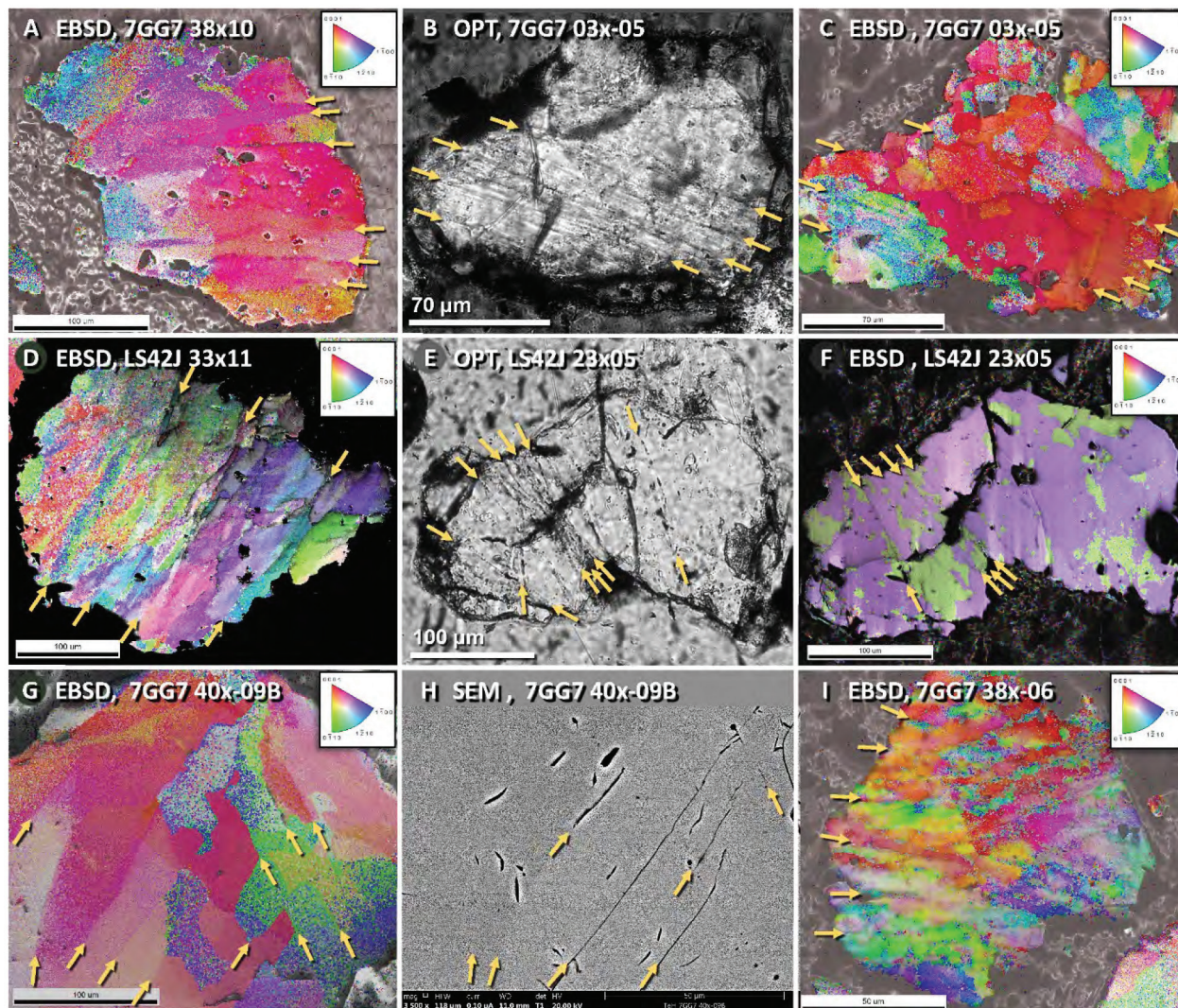
Figure 14: **Multiple shock-fractured quartz grains from the palace and temple complex. (A)** Electron backscatter diffraction (EBSD) image of a quartz grain 7GG7 38×10. Linear features at arrows indicate lamellae infilled with melted silica (glass). The range of colors represents crystalline lattice dislocations caused by shock metamorphic damage to the grain [10, 46]. **(B)** Cross-polarized optical photomicrograph of shock-fractured quartz grain 7GG7 38×-05 from the palace with one set of shock-fractured lamellae. **(C)** EBSD image of the same grain as in panel 'B' shows one set of shock-fractured lamellae. **(D)** EBSD image of quartz grain LS42J 33×11 from the temple complex shows one set of shock-fractured lamellae. **(E)** Cross-polarized optical photomicrograph of shock-fractured quartz grain LS42J 23×05 from the temple complex, showing several sets of shock-fractured lamellae. **(F)** EBSD image of the same grain in panel 'E' with two colors representing the presence of Dauphine twinning, often an indicator of shock metamorphism [10, 46]. **(G)** EBSD image of quartz grain 7GG7 40×-09B from the palace, with a range of colors representing crystalline lattice dislocations caused by shock metamorphic damage to the grain [10, 46]. **(H)** Close-up SEM image of the same grain as in panel 'G' with multiple dark linear features at the arrows representing sub-parallel, sub-planar shock lamellae [10, 46]. **(I)** EBSD image of quartz grain 7GG7 38×-06 from the palace shows two lamellae sets. The range of colors represents crystalline lattice dislocations caused by shock metamorphic damage to the grain [10, 46].

not calculate how some parameters affect temperature (e.g., plasma chemistry/physics and thermal radiation), potentially leading to modeled temperatures that are too high. Thus, Autodyn's calculated temperatures here should be considered semiquantitative.

Modeling limitations

Regarding the EIEP, Marcus et al. [145] emphasized that the results are estimates based on the currently limited understanding of the impact process, and the results have significant uncertainties. Similarly, the Autodyn models have high uncertainties, given that airbursts are highly complex events with multiple variables that are difficult to model. Despite these limitations, hydrocode models are widely used to explore and better understand airburst conditions.

The parameters used for modeling the airburst at Tall el-Hammam are only one set of numerous conceivable scenarios. Our use of this specific model of a 55-m asteroid

does not imply that these parameters accurately describe what happened at Tall el-Hammam around 3600 years ago; instead, it is just one set of circumstances under which the city's destruction could have occurred.

The tests of the modeled results produced by West et al. [9] with Autodyn for Trinity and the EIEP for the airbursts at Tunguska and Chelyabinsk (**Appendix,** *Tunguska, Table A3* **and Appendix, Chelyabinsk,** Table A4) are reasonably close to actual values. These results provide confidence that our model for an airburst at Tall el-Hammam is also reasonably accurate.

Asteroid airburst model for Tall el-Hammam

Modeling parameters: 55-m-wide asteroid, airburst energy: 3.68 Mt, entry velocity: 11 km/s, density: 2920 kg/m^3; entry angle: 90°; initial breakup height: 47.9 km; burst height: 653 m. The touch-down airburst produces an airburst with a TNT-equivalent energy of 3.68 megatons, equaling more than 160 Hiroshima-sized nuclear bombs. We modeled values for pressure, semiquantitative temperature, shock speed, bulk material failure, and visual materials (Figures 15–20). The scale of the occupation mound (comprising the upper and lower tall) is approximately accurate horizontally but vertically exaggerated about two times for better visibility. The Temple, Palace, and other structures are also vertically exaggerated about two times. It is important to note that these buildings are for representational purposes only and are not accurately positioned where they would have been.

Visible materials Video (Click URL below or copy and paste to play). Video 1 is a depiction of the condition of visible materials during the first 500 ms. It is important to note that the impactor fragments (depicted in black) strike the Earth's surface during this interval, forming small shallow craters and destroying all the buildings. A near-vacuum zone forms within the airburst ("void," depicted in white). Note that the video's duration of 20 s is ~25 times slower than the actual duration of the airburst, during which every mudbrick structure in the city is demolished at extreme pressures, temperatures, and wind speeds, and much of the building material is vaporized.

https://vimeo.com/937434939/

Temperature Video (Click URL below or copy and paste to play). Video 2 is a depiction of the airburst's semiquantitative temperatures during the initial 500 ms. Semiquantitative temperatures exceed ~95,000 K, consistent with modeling estimates from Silber et al. [149] and Zhilyaev et al. [150]. After a few seconds, temperatures fall below most minerals' melting point. Note that the video's duration of 19 s is ~26 times slower than the actual 500-ms duration of the airburst. Also, note that the ground temperature remains ambient and does not change significantly.

https://vimeo.com/937432944/

Future research

We suggest future investigations into whether the airburst at Tall el-Hammam may have been part of a larger cyclical bombardment rather than just an isolated event. Dating to approximately 4200-4000 cal BP, close to the age of the event at Tall el-Hammam, widespread evidence for airbursts has been reported from Syria, Sumatra, and deep-sea cores from the Mediterranean, Caspian Sea, and Indian and Austral Oceans by Courty et al. [151–154]. In addition, an airburst of similar age (~3600-3900 cal BP) has been proposed in Kentucky by Tankersley and Meyers [155]. The hypothesis of a cyclical bombardment episode is consistent with the proposal by Napier for a multi-century-long encounter ~3500-4000 years ago with the remnants of the Taurid meteor stream resulting from the hierarchical disintegration of a large comet called a centaur [54, 60]. Notably, Napier's hypothesis of cyclical encounters includes a previous one called the Younger Dryas impact event ~12,800 year ago. If correct, then the Tall el-Hammam episode resulted from a collision with disintegrated remnants of the of the same large comet.

Potential causes of the destruction at Tall el-Hammam

Ten possible causes could have produced the twelve destruction characteristics observed at Tall el-Hammam by Bunch et al. [1] and this study (Table 1). Floods, sandstorms, and tornadoes could have accounted for the linear directional suspension of bones, pottery, and debris in the destruction layer but not the widespread burning, melted pottery, microspherules, melted minerals, and shock-fractured quartz. Earthquakes, human activities (e.g., smelting, pottery-making), city fires, volcanic eruptions, and warfare could have accounted for the burning and melting of some materials but not the directionality and matrix suspension of bones, pottery, and debris. Of all the events, only lightning and an airburst could have created the shock-fractured quartz and high-temperature melted minerals, but lightning could not have accounted for the directionality and matrix suspension of bones, pottery, grain, and debris. Thus, although some non-airburst causes can account for some evidence (25% to 58%), only an airburst can account for all twelve observed destruction characteristics at Tall el-Hammam.

In 1976, George Box wrote, "*All models are wrong, some are useful.* [156]" Regarding the utility of the model proposed here for a touch-down airburst, it is only one possibility among many. The model almost certainly does not precisely describe what happened at Tall el-Hammam around 3600 years ago – it is unlikely that any model can do so. This limitation is because temperature, pressure, and shock speed interactions in an airburst are so complex that dynamical modeling can only approximate the original event. Even so, the hydrocode model presented here is useful because the high-temperature, high-pressure results are consistent with the evidence observed at Tall el-Hammam, including shock-fractured quartz, meltglass, melted pottery, and microspherules.
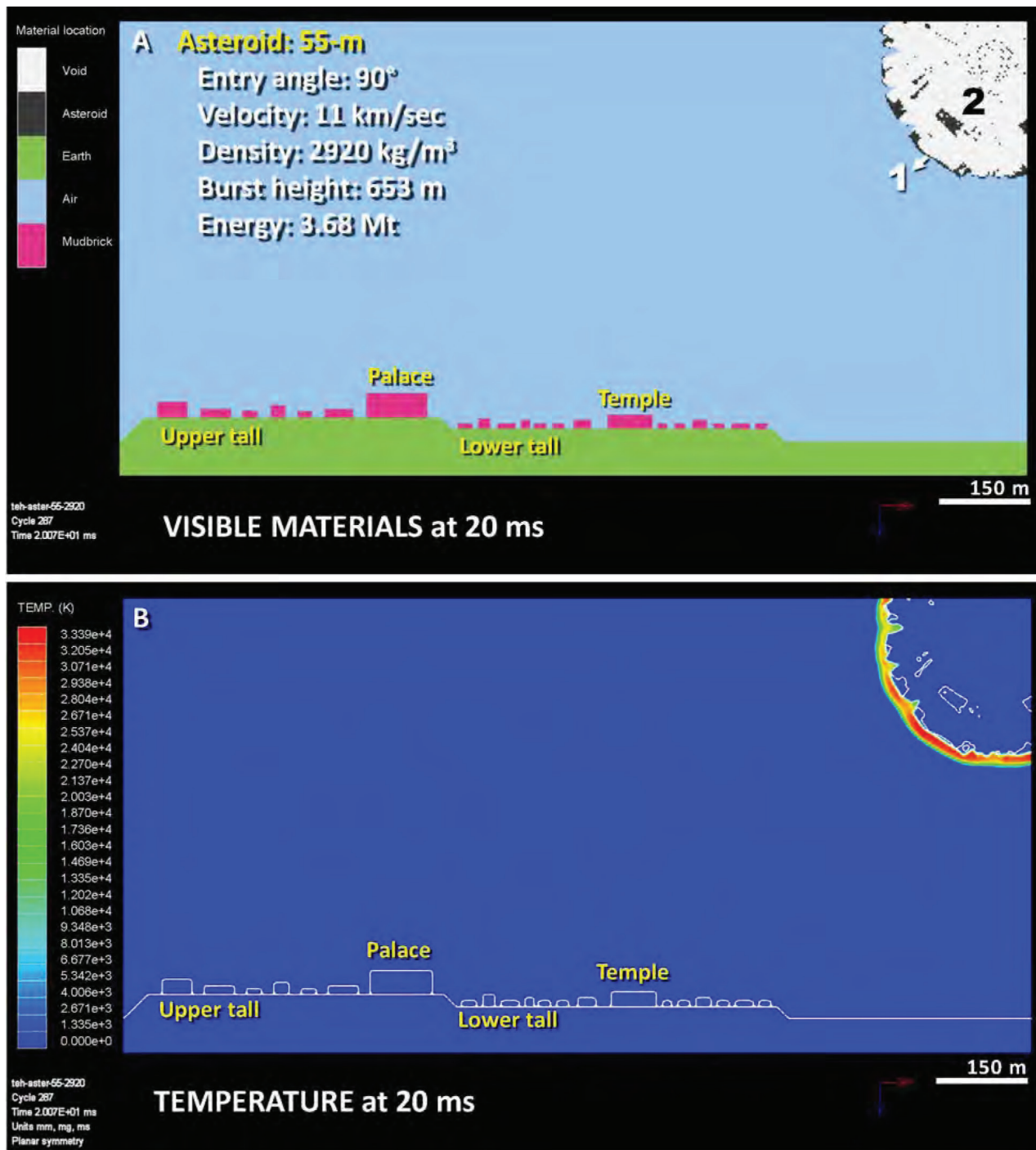
Figure 15: **Modeled airburst at 20 ms. A)** Visible materials. The airburst radius extends to ~250 m. Asteroid fragments (depicted in black) expand along with the airburst and **2)** produce a near-vacuum zone within the airburst ("void," depicted in white). **B)** Within the airburst, the semiquantitative temperature is >30,000 K; pressure reaches ~30 GPa (≥300,000 kg/cm^2), and the shockwave speed is ~18 km/s. Several possibilities might explain the lack of vaporization at high temperatures. (i) A large proportion of the bolide is vaporized, but the temperatures are so transient (<2 s) that there is insufficient time for the complete melting of all bolide fragments. (ii) Some fragments are pushed out at the leading edge of the high-temperature wave and, therefore, are not exposed to the highest temperatures. (iii) Some fragments travel within the near-vacuum (#2 in panel A) behind the shock front and are protected from the highest temperatures.

Figure 16: **Modeled airburst at 83 ms. (A)** Bulk material failure (defined as the point at which strain on a material exceeds a specified pressure value in the tensile direction). A near-vacuum zone within the airburst ("void" in legend) is depicted in white. **(1)** Fragments of the asteroid disperse in all directions. **(2)** These fragments induce bulk material failure and amorphization upon impact with the Earth's surface. The high-velocity fragment impacts result in small, shallow impact craters and generate pressures up to 14 GPa, sufficient to produce shocked quartz. **(B) (1)** The airburst radius expands to ~700 m. **(2)** At the ground surface, semiquantitative temperatures (total energy, including thermal and radiant) reach exceed ~95,000 K [149, 150], sufficient to produce meltglass and spherules from the condensation of melted and vaporized matter. The shock speed reaches ~16 km/s, far higher than that formed by any terrestrial mechanism. For comparison, the most powerful known tornadoes have wind speeds of ~0.16 km/s, 1000 times slower than that modeled here. Field of view = 1500 m wide × 750 m high.

Figure 17: **Modeled airburst at 121 ms. (A) (1)** The airburst radius expands to ~950 m. **(2)** The airburst initiates the destruction of buildings on the lower tall, including the temple complex (largest building on the left), exerting pressures of up to 11 GPa, sufficient to produce shocked and shock-fractured quartz. Semiquantitative temperatures briefly exceed ~95,000 K [149, 150], sufficient to melt and vaporize mudbrick walls. **(B) (1)** Shock speeds reach up to 15 km/s across the lower tall, sufficient to pulverize mudbrick buildings. **(2)** The shockwave strikes the ground and rebounds upward at up to 15 km/s, resulting in what is commonly referred to as a reflection wave.

Conclusions

Our analyses of glass-filled, shock-fractured quartz grains from the terminal destruction layer used ten different advanced techniques to further test the previous conclusions of Bunch et al. [1] about the occurrence of shock metamorphism at Tall el-Hammam. Our observations counter the conclusions of Jaret and Harris [123] that there is no convincing evidence for shock metamorphism at Tall el-Hammam. However, we agree that the grains are not classical high-pressure shock lamellae
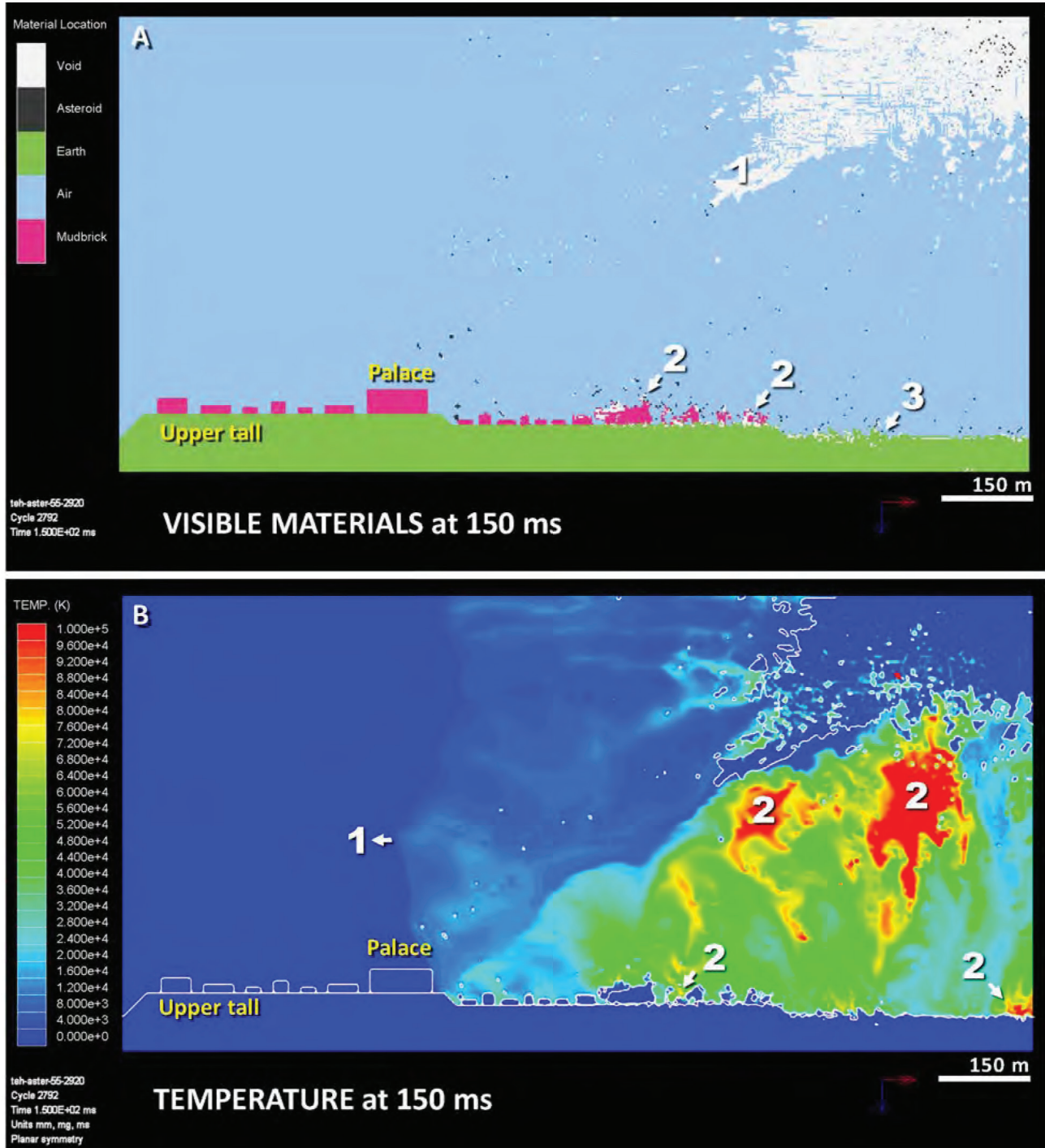
Figure 18: Modeled airburst at 150 ms. (A) Visible materials. **(1)** The central region of the airburst experiences near-vacuum conditions ("void," depicted in white). **(2)** On the lower tall, asteroid fragments (depicted in black) have almost destroyed the temple complex (to the right of the middle) and other buildings. Other fragments are approaching the palace complex on the upper tall. Pressures exceed 8 GPa within the airburst and 1 GPa on the ground. **(3)** Asteroid fragments (depicted in black) strike the ground, creating small, shallow craters. The airburst ejecting these fragments sometimes produces near-vacuum conditions (depicted in white). Such shallow craters would likely be rapidly erased by wind and water erosion after a short time. **(B) (1)** The airburst radius expands to 1090 m. Shock speeds reach up to 15 km/s. **(2)** Semiquantitative temperatures in portions of the reflection wave exceed ~95,000 K [149, 150], both at the ground surface and in the atmosphere.
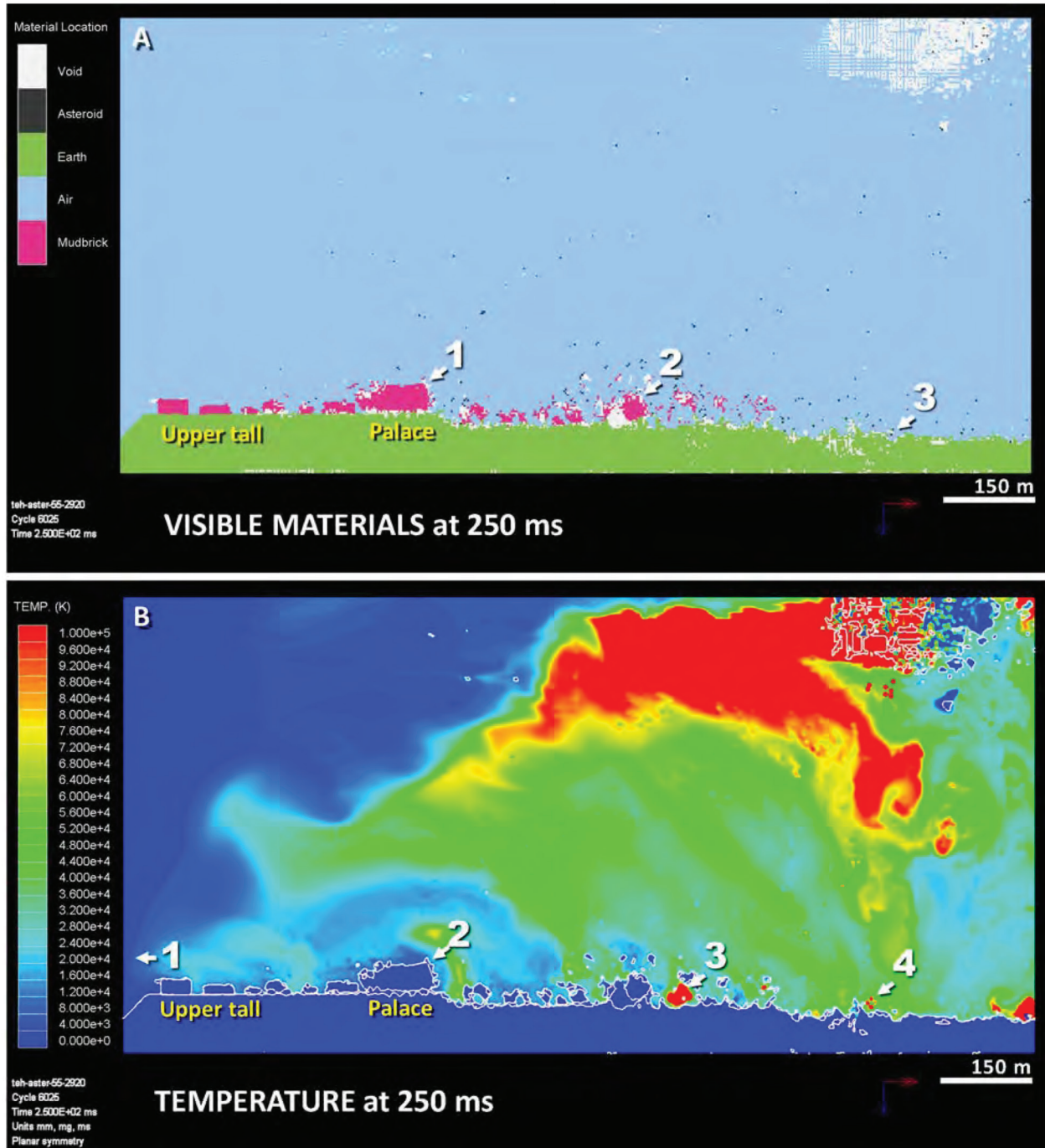
Figure 19: Modeled airburst at 250 ms. (A) (1) Asteroid fragments (depicted in black) and the shockwave begin to demolish the palace and other structures on the upper tall. The surface pressures in some areas reach 2 GPa. In some areas, semiquantitative temperatures exceed ~95,000 K [149, 150], sufficient to melt mudbrick and pottery. **(2)** On the lower tall, the temple complex and surrounding buildings are almost entirely demolished after 250 ms, approximately the duration of an average eye blink. Destruction debris is ejected at velocities of up to 10 km/s and moves left from SW to NE, a direction reported by Bunch et al. [1] to have been observed throughout excavations across the entire site. **(3)** Numerous asteroid fragments continue to strike the surface, creating localized near-vacuum conditions and producing small, shallow craters. **(B) (1)** The airburst radius widens to nearly 1500 m wide after 250 ms. **(2)** The side of the palace facing the airburst is subjected to temperatures briefly exceeding 70,000 K. **(3)** Portions of the lower tall experience temperatures exceeding ~95,000 K for only a few ms [149, 150]. **(4)** Impact craters SW of the lower tall also experience temperatures of >95,000 K [149, 150].
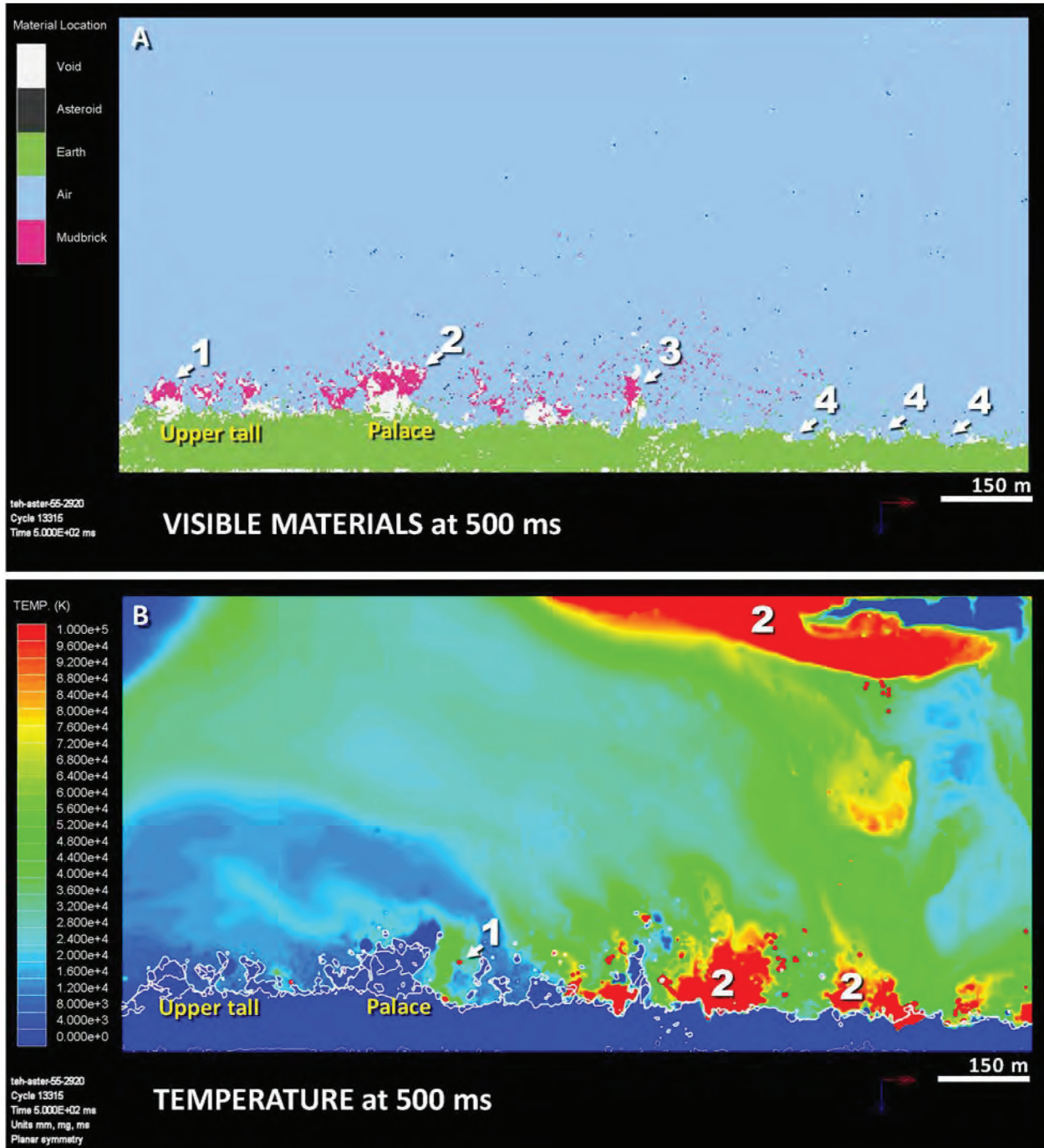
Figure 20: Modeled airburst at 500 ms. (A) (1) The northeastern-most buildings on the upper tall are demolished, and the resulting debris is propelled into the air at velocities of up to 10 km/s and then blown to the NE off the top of the tall [1]. **(2, 3)** The palace, temple, and other upper and lower tall structures are reduced to rubble that is propelled into the air at velocities of up to 10 km/s, producing near-vacuum conditions (depicted in white) underneath. **(4)** Numerous small, shallow craters are distributed across the plain SW of the lower tall. In certain areas, ground pressures exceed two GPa. **(B) (1)** After 500 ms, semiquantitative temperatures near the palace briefly exceed ~95,000 K [149, 150], **(2)** as do portions of the lower tall, the plain to the SW, and the atmosphere above the city. Melting of sediment and mudbrick occurs discontinuously across the ground surface, but because exposure is brief (less than a few seconds), the melting does not extend deeper than a few cm. However, after a few seconds, temperatures drop below 1600 K (1327° C), approximately the melting point of quartz. Below this threshold, meltglass is unlikely to form.

Table 1: Potential explanations for the destruction characteristics observed at Tall el-Hammam.

Destruction characteristics	Flood	Sandstorm	Tornado	Earthquake	Humans	City fire	Fire/eruption	Warfare	Lightning	Airburst
Pottery suspended above floor	Y	Y	Y	-	-	-	-	-	-	Y
Potsherds across multiple rooms	Y	Y	Y	-	-	-	-	-	-	Y
Bones suspended above floor	Y	Y	Y	-	-	-	-	-	-	Y
Debris moved atop foundations	Y	Y	Y	-	-	-	-	-	-	Y
Directionality of pottery. bones	Y	Y	Y	-	-	-	-	-	-	Y
Citywide burning	-	-	-	Y	Y	Y	Y	Y	Y	Y
Ash/charcoal deposition	-	-	-	Y	Y	Y	Y	Y	Y	Y
Bones burned	-	-	-	Y	Y	Y	Y	Y	Y	Y
Melted pottery, mudbricks, plaster	-	-	-	-	Y	Y	Y	Y	Y	Y
Melted Si-Fe-Ca microspherules	-	-	-	-	Y	Y	Y	Y	Y	Y
Melted chromite, zircon. quartz	-	-	-	-	-	-	-	-	Y	Y
Shock-fractured quartz	-	-	-	-	-	-	-	-	Y	Y
# compared to Impact	5 of 12	5 of 12	5 of 12	3 of 12	5 of 12	5 of 12	5 of 12	5 of 12	7 of 12	12 of 12
% compared to Impact	42%	42%	42%	25%	42%	42%	42%	42%	58%	100%

"Humans" refers to human activities, such as smelting and pottery-making. "Fire/eruption" refers to volcanism.

but, instead, are glass-filled shock fractures resulting from a lower grade of shock metamorphism. We also describe new evidence for meltglass breccia and present further support for the unusual SW-to-NE directionality of shattered potsherds randomly distributed throughout the 2-m-thick terminal destruction layer at Tall el-Hammam. This contribution introduces a computer hydrocode model for the airburst of a 55-meter asteroid above a city, showing that a touch-down airburst can intersect the Earth's surface at extreme temperatures and pressures. The modeled airburst shatters the bolide into numerous small fragments that impact Earth's surface at high velocities, producing small, shallow, ephemeral craters. The observed evidence is consistent with an airburst at Tall el-Hammam that produced the conditions necessary to melt pottery, produce meltglass and microspherules, form breccia, demolish the city's buildings, disperse the debris directionality across tens of meters, and generate shock metamorphism via the shockwave and crater formation. We argue, therefore, that a cosmic touch-down airburst is the only plausible explanation for the evidence at Tall el-Hammam.

Acknowledgements

Data availability

All supporting data are included in this manuscript. No unprocessed samples are available.

Author contributions

All authors reviewed and approved the manuscript. P.J.S., S.C., M.A.L., G.A.H., J.P.K., M.D.Y., A.W. conceived of the

Potential conflicts of interest

G.A.H., M.A.L., C.R.M., and A.W. are directors of the Comet Research Group that helped fund the project. Three co-authors, M.A.L, C.R.M., and A.W., are on the editorial board of ScienceOpen's journal, Airbursts and Cratering Impacts. They recused themselves from the editorial process and played no role in reviewing or accepting this contribution.

References

[1] Bunch, T.E.; LeCompte, M.A.; Adedeji, A.V.; Wittke, J.H.; Burleigh, T.D.; Hermes, R.E.; Mooney, C.; Batchelor, D.; Wolbach, W.S.; Kathan J.; et al. A Tunguska Sized Airburst Destroyed Tall el-Hammam a Middle Bronze Age City in the Jordan Valley Near the Dead Sea. *Sci. Rep.* **2021**, *11*(1), 18632; doi: 10.1038/s41598.021.97778.3.

[2] Collins, S.; Kobs, C.M.; Luddeni, M.C. *The Tall al-Hammam Excavations, Volume 1: An Introduction to Tall al-Hammam: Seven Seasons (2005–2011) of Ceramics and Eight Seasons (2005–2012) of Artifacts from Tall al-Hammam*; Penn State Press, 2015.

[3] Collins, S.; Byers, G.A.; Kobs, C.M. *The Tall al-Ḥammām Excavation Project, Season Twelve 2017 Report: Excavation, Interpretations, and Insights*; Department of Antiquities of Jordan: Amman, Jordan, 2017.

[4] Silvia, P.J. *The Middle Bronze Age Civilization-Ending Destruction of the Middle Ghor*; Trinity Southwest University: Albuquerque, NM, 2015.

[5] Boslough, M. Airburst Modeling. In *First International Workshop on Potentially Hazardous Asteroids Characterization*; Atmospheric Entry and Risk Assessment, 2015.

[6] Boslough, M. Airburst Modeling. In *Handbook of Cosmic Hazards and Planetary Defense*; Allahdadi, F., Pelton, J., Eds.; Springer: Cham, 2021: pp. 1–24.

[7] Van Ginneken, M.; Goderis, S.; Artemieva, N.; Debaille, V.; Decrée, S.; Harvey, R.P.; Huwig, K.A.; Hecht, L.; Yang, S.; Kaufmann, F.E.D.; et al. A Large Meteoritic Event Over Antarctica ca. 430 ka ago Inferred from Chondritic Spherules from the Sør Rondane Mountains. *Sci. Adv.* **2021**, *7*(14), eabc1008; doi: 10.1126/sciadv.abc1008.

[8] van Ginneken, M.; Harvey, R.P.; Goderis, S.; Artemieva, N.; Boslough, M.; Maeda, R.; Gattacceca, J.; Folco, L.; Yamaguchi, A.; Sonzogni, C.; et al. The Identification of Airbursts in the Past: Insights from the BIT-58 Layer. *Earth Planet. Sci. Lett.* **2024**, *627*, 118562; doi: 10.1016/j.epsl.2023.118562.

[9] West, A.; Young, M.D.; Costa, L.; Kennett, J.P.; Moore, C.R.; LeCompte, M.A.; Kletetschka, G.; Hermes, R.E. Modeling Airbursts by Comets, Asteroids, and Nuclear Detonations: Shock Metamorphism, Meltglass, and Microspherules. *Airburst. Crater. Imp.* **2024**, *2*, 1–30.

[10] Hermes, R.E.; Wenk, H.-R.; Kennett, J.P.; Bunch, T.E.; Moore, C.R.; LeCompte, M.A.; Kletetschka, G.; Adedeji, A.V.; Langworthy, K.; Razink, J.J.; et al. Microstructures in Shocked Quartz: Linking Nuclear Airbursts and Meteorite Impacts. *ScienceOpen* **2023**, *1*(1), 1–40.

[11] Artemieva, N.; Shuvalov, V. Atmospheric Shock Waves after impacts of Cosmic Bodies up to 1000 m in Diameter. *Meteorit. Planet. Sci.* **2019**, *54*(3), 592–608.

[12] Molnár, M.; Ventura, K.; Švanda, P.; Štaffen, Z.; Rappenglück, M.A.; Ernstson, K. Chrudim-Pardubice: Evidence for a Young Meteorite Impact Strewn Field in the Czech Republic. In *48th Annual Lunar and Planetary Science Conference*; 2017; Volume 1964, pp. 1920.

[13] Poßekel, J.; Molnár, M.; Ernstson, K. The Proposed Meteorite Impact Event in the Czech Republic: Evidence Strengthened by Investigations with the Digital Terrain Model. In *53rd Lunar and Planetary Science Conference*; 2022; Volume 2678, pp. 1558.

[14] Ernstson, K.; Müller, W.; Gawlik-Wagner, A. The Saarlouis Semi Crater Structure: Notable Insight into the Saarland (Germany) Meteorite Impact Event Achieved. *In 49th Lunar and Planetary Science Conference*, 2018; Abstract #1876.

[15] Ernstson, K.; Portz, D.; Müller, W. Zhamanshinite-Like Black-Glass Melt Rocks from the Saarland (Germany) Meteorite Impact Site. In *52nd Lunar and Planetary Science Conference*; 2021;Volume 2548, pp. 1350.

[16] Siegel, U.; Müller, W.; Michelbacher, S.; Ernstson, K.; Rommelfangen, J. Shatter Cones in Litermont Quartzites: Saarlouis/Nalbach (Saarland, Germany) Meteorite Impact Event Strengthened. In *Lunar and Planetary Science Conference*; 2022; Abstract #1842.

[17] Ernstson, K.; Bauer, F.; Hiltl, M. A Prominent Iron Silicides Strewn Field and Its Relation to the Bronze Age/Iron Age Chiemgau Meteorite Impact Event (Germany). *Earth Sci.* **2023**, *12*(1), 26–40.

[18] Ernstson, K.; Mayer, W.; Neumair, A.; Rappenglueck, B.; Rappenglück, M.A.; Sudhaus, D.; Zeller, K.W. The Chiemgau Crater Strewn Field: Evidence of a Holocene Large Impact Event in Southeast Bavaria, Germany. *J. Sib. Fed.* **2010**, *1*(3), 72–103.

[19] Ernstson, K.; Poßekel, J.; Rappenglück, M.A. Near-Ground Airburst Cratering: Petrographic and Ground Penetrating Radar (GPR) Evidence for a Possibly Enlarged Chiemgau Impact Event (Bavaria, SE-Germany). In *Proceedings of the Lunar and Planetary Science Conference*; 2020; Volume 2326, pp. 1231.

[20] Ernstson, K.; Sideris, C.; Liritzis, I.; Neumair, A. The Chiemgau Meteorite Impact Signature of the Stöttham Archaeological Site (Southeast Germany). *Mediterr. Archaeol. Archaeom.* **2012**, *12*(2), 249–259.

[21] Rappenglück, B.; Hiltl, M.; Ernstson, K. Artifact-in-impactite: A New Kind of Impact Rock. Evidence from the Chiemgau Meteorite Impact in Southeast Germany. In *Proceedings of the Modern Problems of Theoretical, Experimental, and Applied Mineralogy (Yushkin Readings – 7-10 December 2020, Syktyvkar, Russia)*; 2020; pp. 365–367.

[22] Rappenglück, B.; Hiltl, M.; Ernstson, K. Metallic Artifact Remnants in a Shock-Metamorphosed Impact Breccia: an Extended View of the Archeological Excavation at Stöttham (Chiemgau, SE-Germany). In *50th Annual Lunar and Planetary Science Conference*; 2019; Volume 2132, pp. 1334.

[23] Rappenglück, M.A.; Ernstson, K.; Mayer, W.; Beer, R.; Benske, G.; Siegl, C.; Sporn, R.; Bliemetsrieder, Th.; Schüssler, U. *The Chiemgau Impact Event in the Celtic Period: Evidence of a Crater Strewnfield and a Cometary Impactor Containing Presolar Matter*; Chiemgau-Impakt c/o Kord Ernstson, 2004.

[24] Rappenglück, B.; Hiltl, M.; Poßekel, J.; Rappenglück, M.A.; Ernstson, K. People Experienced the Prehistoric Chiemgau Meteorite Impact – Geoarchaeological Evidence from Southeastern Germany: A Review. *Mediterr. Archaeol. Archaeom.* **2023**, *23*(1), 1–29.

[25] Rappenglück, B.; Hiltl, M.; Ernstson, K. Exceptional Evidence of a Meteorite Impact at the Archaeological Site of Stöttham (Chiemgau, SE-Germany). In *Harmony and Symmetry: Celestial Regularities Shaping Human Culture. Proceedings of the SEAC 2018 Conference*; Draxler, S., Lippitsch, M.E., Wolfschmidt, G., Eds.; Hamburg, 2020; pp. 116–125.

[26] Rappenglück, B.; Hiltl, M.; Ernstson, K. The Chiemgau Impact: Evidence of a Latest Bronze Age/Early Iron Age Meteorite Impact in the Archaeological Record, and Resulting Critical Considerations of Catastrophism. In *Beyond Paradigms in Cultural Astronomy*, César González-García, A., Frank, R.M., Sims, L.D., Rappenglück, M.A., Zotti, G., Belmonte, J.A., Šprajc, I., Eds.; 2021; pp. 57–64.

[27] Shumilova, T.G.; Isaenko, S.I.; Ulyashev, V.V.; Makeev, B.A.; Rappenglück, M.A.; Veligzhanin, A.A.; Ernstson, K. Enigmatic Glass-Like Carbon from the Alpine Foreland, Southeast Germany: A Natural Carbonization Process. *Acta Geol. Sin. (English Edition)* **2018**, *92*(6), pp. 2179–2200; doi: 10.1111/1755.6724.13722.

[28] Waldmann, G.; Herten, F.; Hiltl, M.; Ernstson, K. The Enigmatic Niederrhein (Germany) Deposit: Evidence of a Middle-Pleistocene Meteorite Impact Strewn Field. In *49th Annual Lunar and Planetary Science Conference*; 2018; Volume 2083, pp. 1610.

[29] Ernstson, K.; Schulz-Hertlein, G.; Poßekel, J.; Ernstson, T. A Probable Holocene Meteorite Impact Crater Strewn Field in Lower Franconia (Germany): Evidence from Digital Terrain Models and Geophysical Surveys (GPR, Electrical Imaging, Geomagnetics). In *Poster, Proceedings of the AGU Fall Meeting*; 2022.

[30] Ernstson, K.; Poßekel, J.; Kurtz, J. The Enigmatic Sachsendorf Bay Structure (Oderbruch, Northeast Germany): Evidence of a Pleistocene/Holocene Meteorite Impact Event. In *12th Planetary Crater Consortium Meeting*; 2021; Volume 2621, pp. 2022.

[31] Ahokas, H. *Thirty-Three Previously Unknown Meteoritic Craters of Diameter from 5 to 100 m in Western Kouvola, Finland from a Swarm of Impactors in the Holocene*; Helsinki: Kave, 2023; p. 38.

[32] Ernstson, K.; Molnár, M.; Poßekel, J. *The Enigmatic Luzice (Czech Republic) Megablock and Melt Rock Megabreccia: Evidence of a Meteorite Impact Origin*; LPI Contributions, 2023; Volume 2990, pp. 6059.

[33] Molnár, M.; Ventura, K.; Poßekel, J.; Ernstson, K. *The Kolešovice 20 km-Diameter Structure (Czech Republic): Evidence of an Airburst Impact Crater*; LPI Contributions, 2023; Volume 2806, pp. 1428.

[34] Tankersley, K.B.; Meyers, S.A.; Stimpson, D.; Knepper, S.M. Evidence for a large late-Holocene Strewn Field in Kiowa County, Kansas, USA. *Airburs. Crater. Imp.* **2023**, *1*(1), 1–16; doi: 10.14293/ACI.2023.0005.

[35] Tankersley, K.B.; Meyers, S.D.; Meyers, S.A.; Jordan, J.A.; Herzner, L.; Lentz, D.L.; Zedaker, D. The Hopewell Airburst Event, 1699–1567 Years Ago (252–383 CE). *Sci. Rep.* **2022**, *12*(1), 1–18; doi: 10.1038/s41598.022.05758.y.

[36] Bronikowska, M.; Artemieva, N.; Wünnemann, K. Reconstruction of the Morasko Meteoroid Impact—Insight from Numerical Modeling. *Meteorit. Planet. Sci.* **2017**, *52*(8), 1704–1721; doi: 10.1111/maps.12882.

[37] Harris, R.; Schultz, P. Are Ti-Rich Particles in Late Pleistocene Sediments from Patagonia Distal Ejecta from an Atacama Airburst? In *Proceedings of the Lunar and Planetary Science Conference*; 2019; Volume 2132, pp. 2526.

[38] Schultz, P.; Harris, R.S.; Perroud, S.; Blanco, N.; Tomlinson, A.J.; Valenzuela, M. Late Pleistocene Fireballs Over the Atacama Desert, Chile. In *Proceedings of the Lunar and Planetary Science Conference*; 2019; p. 50.

[39] Schultz, P.H.; Scott Harris, R.; Perroud, S.; Blanco, N.; Tomlinson, A.J. Widespread Glasses Generated by Cometary Fireballs During the Late Pleistocene in the Atacama Desert, Chile. *Geology* **2022**, *50*(2), 205–209; doi: 10.1130/G49426.1.

[40] Andronikov, A.V.; Andronikova, I.E. Sediments from around the Lower Younger Dryas Boundary (USA): Implications from LA-ICP-Analysis. *Geogr. Ann. A* **2016**, *98*, 221–236; doi: 10.1111/geoa.12132.

[41] Ballard, J.P.; Bijkerk, A.K.; Quartz Melt Structures in European Coversands May Support Younger Dryas Extraterrestrial Impact Hypothesis. In *Proceedings of the UT Geography Research Symposium 2014 "Mapping Outside the Lines: Geography as a Nexus for Interdisciplinary and Collaborative Research"*; Knoxville, Tennessee, 2014.

[42] Bement, L.C.; Madden, A.S.; Carter, B.J.; Simms, A.R.; Swindle, A.L.; Alexander, H.M.; Fine, S.; Benamara, M. Quantifying the Distribution of Nanodiamonds in Pre-Younger Dryas to Recent age Deposits Along Bull Creek, Oklahoma Panhandle, USA. *Proc. Natl. Acad Sci. U. S. A.* **2014**, *111*(5), 1726–1731; doi: 10.1073/pnas.1309734111.

[43] Firestone, R.B.; West, A.; Kennett, J.P.; Becker, L.; Bunch, T.E.; Revay, Z.S.; Schultz, P.H.; Belgya, T.; Kennett, D.J.; Erlandson, J.M.; et al. Evidence for an Extraterrestrial Impact 12,900 Years ago that Contributed to the Megafaunal Extinctions and the Younger Dryas Cooling. *Proc. Natl. Acad Sci. U. S. A.* **2007**, *104*(41), 16016–16021; doi: 10.1073/pnas.0706977104.

[44] Israde-Alcántara, I.; Bischoff, J.L.; Domínguez-Vázquez, G.; Li, H.C.; DeCarli, P.S.; Bunch, T.E.; Wittke, J.H.; Weaver, J.C.; Firestone, R.B.; et al. Evidence from Central Mexico Supporting the Younger Dryas Extraterrestrial Impact Hypothesis. *Proc. Natl. Acad Sci. U. S. A.* **2012**, *109*(13), E738–E747.

[45] LeCompte, M.A.; Goodyear, A.C.; Demitroff, M.N.; Batchelor, D.; Vogel, E.K.; Mooney, C.; Rock, B.N.; Seidel, A.W. Independent Evaluation of Conflicting Microsphere Results from Different Investigations of the Younger Dryas Impact Hypothesis. *Proc. Natl. Acad Sci. U. S. A.* **2012**, *109*(44), E2960–E2969; doi: 10.1073/pnas.1208603109.

[46] Moore, A.M.T.; Kennett, J.P.; LeCompte, M.A.; Moore, C.R.; Li, Y.Q.; Kletetschka, G.; Langworthy, K.; Razink, J.J.; Brogden, V.; van Devener, B.; et al. Abu Hureyra, Syria, Part 1: Shock-Fractured Quartz Grains Support 12,800-Year-Old Cosmic Airburst at the Younger Dryas onset. *Airburs. Crater. Imp.* **2023**. *1*(1), 1–28.

[47] Moore, A.M.T.; Kennett, J.P.; Napier, W.M.; Bunch, T.E.; Weaver, J.C.; LeCompte, M.; Adedeji, A.V.; Hackley, P.; Kletetschka, G.; Hermes, R.E.; et al. Evidence of Cosmic Impact at Abu Hureyra, Syria at the Younger Dryas Onset (~12.8 ka): High-temperature Melting at >2200 °C. *Sci. Rep.* **2020**, *10*(1), 4185; doi: 10.1038/s41598.020.60867.w.

[48] Moore, C.R.; West, A.; LeCompte, M.A.; Brooks, M.J.; Daniel, I.R., Jr.; Goodyear, A.C.; Ferguson, T.A.; Ivester, A.H.; Feathers, J.K.; Kennett, J.P.; et al. Widespread platinum anomaly documented at the Younger Dryas onset in North American sedimentary sequences. *Sci. Rep.* **2017**, *7*, 44031; doi: 10.1038/srep44031.

[49] Teller, J.; Boyd, M.; Le Compte, M.; Kennett, J.; West, A.; Telka, A.; Diaz, A.; Adedeji, V.; Batchelor, D.; Mooney, C. A Multi-Proxy Study of Changing Environmental Conditions in a Younger Dryas Sequence in Southwestern Manitoba, Canada, and Evidence for an Extraterrestrial Event. *Quat. Res.* **2019**, 93, 60–87.

[50] Wolbach, W.S.; Ballard, J.P.; Mayewski, P.A.; Adedeji, V.; Bunch, T.E.; Firestone, R.B.; French, T.A.; Howard, G.A.; Israde-Alcántara, I.; Johnson, J.R.; et al. Extraordinary Biomass-Burning Episode and Impact Winter Triggered by the Younger Dryas Cosmic Impact

~12,800 Years Ago. 1. Ice Cores and Glaciers. *J. Geol.* **2018**, *126*(2), 165–184; doi: 10.1086/695703.

[51] Wolbach, W.S.; Ballard, J.P.; Mayewski, P.A.; Parnell, A.C.; Cahill, N.; Adedeji, V.; Bunch, T.E.; Domínguez-Vázquez, G.; Erlandson, J.M.; Firestone, R.B.; et al. Extraordinary Biomass-Burning Episode and Impact Winter Triggered by the Younger Dryas Cosmic Impact ~12,800 Years Ago. 2. Lake, Marine, and Terrestrial Sediments. *J. Geol.* **2018**, *126*(2), 185–205; doi: 10.1086/695704.

[52] Bunch, T.E.; Hermes, R.E.; Moore, A.M.; Kennett, D.J.; Weaver, J.C.; Wittke, J.H.; DeCarli, P.S.; Bischoff, J.L.; Hillman, G.C.; Howard, G.A.; et al. Very High-Temperature Impact Melt Products as Evidence for Cosmic Airbursts and Impacts 12,900 Years Ago. *Proc. Natl. Acad Sci. U. S. A.* **2012**, *109*(28), E1903–E1912; doi: 10.1073/pnas.1204453109.

[53] Moore, A.M.T.; Kennett, J.P.; Napier, W.M.; Bunch, T.E.; Weaver, J.C.; LeCompte, M.A.; Victor Adedeji, A.; Kletetschka, G.; Hermes, R.E.; Wittke, J.H.; et al. Abu Hureyra, Syria, Part 2: Additional Evidence Supporting the Catastrophic Destruction of this Prehistoric Village by a Cosmic Airburst ~12,800 Years Ago. *Airburs. Crater. Imp.* **2023**. *1*(1), 1–36.

[54] Moore, A.M.T.; Kennett, J.P.; Napier, W.M.; LeCompte, M.A.; Moore, C.R.; West, A. Abu Hureyra, Syria, Part 3: Comet Airbursts Triggered Major Climate Change 12,800 Years Ago that Initiated the Transition to Agriculture. *ScienceOpen* **2023**, *1*(1), 1–24.

[55] Moore, C.R.; Brooks, M.J.; Goodyear, A.C.; Ferguson, T.A.; Perrotti, A.G.; Mitra, S.; Listecki, A.M.; King, B.C.; Mallinson, D.J.; Lane, C.S.; et al. Sediment Cores from White Pond, South Carolina, contain a Platinum Anomaly, Pyrogenic Carbon Peak, and Coprophilous Spore Decline at 12.8 ka. *Sci. Rep.* **2019**, *9*(1), 15121; doi: 10.1038/s41598.019.51552.8.

[56] Moore, C.R.; Brooks, M.J.; Dunbar, J.S.; Hemmings, C.A.; Langworthy, K.A.; West, A.; LeCompte, M.A.; Adedeji, V.; Kennett, J.P.; Feathers, J.K. Geoarchaeological Investigations at Wakulla Springs, Florida. Southeastern Archaeological Conference (SEAC), *Proceedings of the 76th Annual Meeting*, November 6–9, 2019.

[57] Pino, M.; Abarzúa, A.M.; Astorga, G.; Martel-Cea, A.; Cossio-Montecinos, N.; Navarro, R.X.; Lira, M.P.; Labarca, R.; LeCompte, M.A.; Adedeji, V.; et al. Sedimentary Record from Patagonia, Southern Chile Supports Cosmic-Impact Triggering of Biomass Burning, Climate Change, and Megafaunal Extinctions at 12.8 ka. *Sci. Rep.* **2019**, *9*(1), 4413; doi: 10.1038/s41598.018.38089.y.

[58] Wittke, J.H.; Weaver, J.C.; Bunch, T.E.; Kennett, J.P.; Kennett, D.J.; Moore, A.M.T.; Hillman, G.C.; Tankersley, K.B.; Goodyear, A.C.; Moore, C.R.; et al. Evidence for Deposition of 10 Million Tonnes of Impact Spherules across Four Continents 12,800 y Ago. *Proc. Natl. Acad Sci. U. S. A.* **2013**, *110*(23), E2088–E2097; doi: 10.1073/pnas.130176011.

[59] Napier, W.M. Palaeolithic Extinctions and the Taurid Complex. *Mon. Not. R Astron. Soc.* **2010**, *405*, 1901–1906; doi: 10.1111/j.1365.2966.2010.16579.x.

[60] Napier, W.M. The Hazard from Fragmenting Comets. *Mon. Not. R Astron. Soc.* **2019**, *488*(2), 1822–1827; doi: 10.1093/mnras/stz1769.

[61] Osinski, G.R.; Kieniewicz, J.; Smith, J.R.; Boslough, M.B.E.; Eccleston, M.; Schwarcz, H.P.; Kleindienst, M.R.; Haldemann, A.F.C.; Churcher, C.S. The Dakhleh Glass: Product of an Impact Airburst or Cratering Event In the Western Desert of Egypt? *Meteorit. Planet. Sci.* **2008**, *43*(12), 2089–2106; doi: 10.1111/j.1945.5100.2008.tb00663.x.

[62] Harris, R.; Schultz, P. Evidence of Multiple Cometary Airbursts During the Pleistocene from Pica (Chile), Dakhleh (Egypt), and Edeowie (Australia) Glasses. In *Proceedings of the Lunar and Planetary Science Conference*; 2020; Volume 2326, pp. 2229.

[63] Smith, J.R.; Kleindienst, M.R.; Schwarcz, H.P.; Churcher, C.S.; Kieniewicz, J.M.; Osinski, G.R.; Haldemann, A.F.C. Potential Consequences of a Mid-Pleistocene Impact Event for the Middle Stone Age Occupants of Dakhleh Oasis, Western Desert, Egypt. *Quat. Int.* **2009**, *195*(1–2), 138–149; doi: 10.1016/j.quaint.2008.02.005.

[64] Koeberl, C. Libyan Desert Glass: Geochemical Composition and Origin. In *Proceedings of the Silica '96 Meeting on Libyan Desert Glass and Related Desert Events*; 1997; pp. 121–131.

[65] Boslough, M.B.; Crawford, D.A. Low-Altitude Airbursts and the Impact Threat-Final LDRD Report. 2007, Sandia National Lab. (SNL-NM), Albuquerque, NM (United States).

[66] Boslough, M.; Crawford, D.A. Low-Altitude Airbursts and the Impact Threat. *Int. J. Impact Eng.* **2008**, *35*(12), 1441–1448; doi: 10.1016/j.ijimpeng.2008.07.053.

[67] Moore, A.; Kennett, D. Cosmic Impact, the Younger Dryas, Abu Hureyra, and the Inception of Agriculture in Western Asia. *Eurasian Prehist.* **2013**, *10*(1–2), 57–66.

[68] Collins, S. Tall el-Hammam Is Sodom: Billington's Heshbon Identification Suffers from Numerous Fatal Flaws. *Bib. Res. Bull.* **2012**, *XII*(1).

[69] Collins, S. *The Search for Sodom & Gomorrah*. Trinity Southwest University Press, 2006, pp. 71.

[70] Collins, S.; Aljarrah, H. *Tall el-Hammam Season Six, 2011: Excavation, Survey, Interpretations and Insights*; Department of Antiquities of Jordan: Amman, Jordan, 2011.

[71] Collins, S.; Byers, G.A.; Kobs, C.M. *The Tall al-Hammam Excavation Project, Season Fourteen 2019 Report: Excavation, Interpretations, and Insights*; Department of Antiquities of Jordan: Amman, Jordan, 2019.

[72] Collins, S.; Byers, G.A.; Kobs, C.M. *The Tall al-Ḥammām Excavation Project, Season Ten 2015 Report: Excavation, Interpretations, and Insights*; Department of Antiquities of Jordan: Amman, Jordan, 2015.

[73] Collins, S.; Byers, G.A.; Kobs, C.M. *The Tall al-Ḥammām Excavation Project, Season Eleven 2016 Report: Excavation, Interpretations, and Insights*; Department of Antiquities of Jordan: Amman, Jordan, 2016.

[74] Collins, S.; Byers, G.A.; Kobs, C.M. *The Tall al-Ḥammām Excavation Project, Season Thirteen 2018 Report: Excavation, Interpretations, and Insights*; Department of Antiquities of Jordan: Amman, Jordan, 2018.

[75] Collins, S.; Byers, G.A.; Kobs, C.M.; Silvia, P. *Tall el-Hammam Season Nine, 2014: Excavation, Survey, Interpretations and Insights*; Department of Antiquities of Jordan: Amman, Jordan, 2014.

[76] Collins, S.; Byers, G.A.; Luddeni, M.C.; Moore, J.W. *The Tall el-Hammam Excavation Project, Season Activity Report, Season Two: 2006/2007 Excavation, Exploration, and Survey*; Annual of the Department of Antiquities of Jordan, 2007. *VII*(9).

[77] Collins, S.; et al. *Tall el-Hammam Season Seven, 2012: Excavation, Survey, Interpretations and Insights*; Department of Antiquities of Jordan: Amman, Jordan, 2012, pp. 1–19.

[78] Collins, S.; Hamdan, G.A.; Byers, G.A.; Haroun, J.; Aljarrah, H.; Luddeni, M.C.; McAllister, S.; Abu-Shmais, A.; Dasougi, Q. *The Tall el-Hammam Excavation Project, Season Activity Report, Season Five: 2010 Excavation, Exploration, and Survey*; Department of Antiquities of Jordan: Amman, Jordan, 2010.

[79] Collins, S.; Hamdan, K.; Byers, G.A.; McAllister, S.; Haroun, J.; Luddeni, M.C.; Massara, GK; Al-Jarrah, H.; Mullins, R.A.; Dasougi, Q. Tall al-Ḥammām: Preliminary Report on Four Seasons of Excavation (2006-2009). *ADAJ* **2009**, *53*, 385–414.

[80] Collins, S.; Hamdan, G.A.; Haroun, J.; Aljarrah, H.; Luddeni, M.C.; McAllister, S.; Dasougi, Q.; Abu-Shmais, A.; Graves, D. *The Tall el-Hammam Excavation Project, Season Activity Report, Season Four: 2009 Excavation, Exploration, and Survey*; Department of Antiquities of Jordan: Amman, Jordan, 2009.

[81] Collins, S.; Kobs, C.M.; Byers, G.A. *The Tall al-Hammam Excavation Project, Season Fifteen 2020 Report: Excavation, Interpretations, and Insights*; Department of Antiquities of Jordan: Amman, Jordan, 2020.

[82] Collins, S.; Tarawneh, K.; Byers, G.A.; Kobs, C.M. *Tall el-Hammam Season Eight, 2013: Excavation, Survey, Interpretations and Insights*; Department of Antiquities of Jordan: Amman, Jordan, 2013.

[83] Collins, S. 2021. Personal communication for this paper.

[84] Florenskiy, K. Preliminary results from the 1961 combined Tunguska meteorite expedition. *Meteoritica* **1965**, *XXIII*(23), 3–37.

[85] Longo, G.; Di Martino, M.; Andreev, G.; Anfinogenov, J.; Budaeva, L.; Kovrigin, E.; A New Unified Catalogue and a New Map of the 1908 Tree Fall in the Site of the Tunguska Cosmic Body Explosion. In *Asteroid-Comet Hazard-2005, Institute of Applied Astronomy of the Russian Academy of Sciences*; St. Petersburg: Russia, 2005; pp. 222–225.

[86] Koeberl, C.; Huber, H.J.; Morgan, M.L.; Warme, J. Search for an Extraterrestrial Component in the Late Devonian Alamo Impact Breccia (Nevada): Results of Iridium Measurements. In *Impact Markers in the Stratigraphic Record*; Springer, 2003; pp. 315–332.

[87] Harris, R.; Schultz, P. Impact Amber, Popcorn, and Pathology: The Biology of Impact Melt Breccias and Implications for Astrobiology. In *38th Lunar and Planetary Science Conference Lunar and Planetary*; 2007; pp. 12–16.

[88] Schultz, P.H.; Scott Harris, R.; Clemett, S.J.; Thomas-Keprta, K.L.; Zárate, M. Preserved Flora and Organics in Impact Melt Breccias. *Geology* **2014**, *42*(6), 515–518; doi: 10.1130/G35343.1.

[89] Stöffler, D. Progressive Metamorphism and Classification of Shocked and Brecciated Crystalline Rocks at Impact Craters. *J. Geophys. Res.* **1971**, *76*(23), 5541–5551; doi: 10.1029/JB076i023p05541.

[90] Butterman, W.C.; Foster, W.R. Zircon Stability and the Zr02-Si02 Phase Diagram. *Am. Miner.* **1967**, *52*(5–6), 880–885.

[91] Bohor, B.; Betterton, W.; Krogh, T. Impact-Shocked Zircons: Discovery of Shock-Induced Textures Reflecting Increasing Degrees of Shock Metamorphism. *Earth Planet. Sci. Lett.* **1993**, *119*(3), 419–424; doi: 10.1016/0012.821X(93)90149.4.

[92] Glass, B.P.; Simonson, B.M. *Mesozoic Spherule/Impact Ejecta Layers, in Distal Impact Ejecta Layers*; Springer, 2013; pp. 245–320.

[93] Goltrant, O.; Cordier, P.; Doukhan, J.-C. Planar Deformation Features in Shocked Quartz; a Transmission Electron Microscopy Investigation. *Earth Planet. Sci. Lett.* **1991**, *106*(1–4), 103–115; doi: 10.1016/0012.821X(91)90066.Q.

[94] Christie, J.; Ardell, A. Substructures of Deformation Lamellae in Quartz. *Geology* **1974**, *2*(8), 405–408; doi: 10.1130/0091.7613(1974)2[[405:SODLIQ]]2.0.CO;2.

[95] Bohor, B.; Fisler, D.; Gratz, A.J. Distinguishing Between Shock and Tectonic Lamellae with the SEM. In *Proceedings of the Lunar and Planetary Science Conference*; 1995; Volume 26, pp. 145.

[96] Gratz, A.J.; Fisler, D.K.; Bohor, B.F. Distinguishing Shocked from Tectonically Deformed Quartz by the use of the SEM and Chemical Etching. *Earth Planet. Sci. Lett.* **1996**, *142*(3–4), 513–521.

[97] Gratz, A.J.; Tyburczy, J.; Christie, J.; Ahrens, T.; Pongratz, P. Shock Metamorphism of Deformed Quartz. *Phys. Chem. Minerals* **1988**, *16*(3), 221–233; doi: 10.1007/BF00220689.

[98] Hamers, M.; Drury, M. Scanning Electron Microscope-Cathodoluminescence (SEM-CL) Imaging of Planar Deformation Features and Tectonic Deformation Lamellae in Quartz. *Meteoritics & Planetary Science* **2011**, *46*(12), 1814–1831.

[99] Stöffler, D.; Gault, D.E.; Wedekind, J.; Polkowski, G. Experimental Hypervelocity Impact Into Quartz Sand: Distribution and Shock Metamorphism of Ejecta. *J. Geophys. Res.* **1975**, *80*(29), 4062–4077; doi: 10.1029/JB080i029p04062.

[100] Stöffler, D.; Langenhorst F. Shock Metamorphism of Quartz in Nature and Experiment: I. Basic Observation and Theory. *Meteoritics* **1994**, *29*(2), 155–181; doi: 10.1111/j.1945.5100.1994.tb00670.x.

[101] Vernooij, M.G.; Langenhorst F. Experimental Reproduction of Tectonic Deformation Lamellae in Quartz and Comparison to Shock-Induced Planar Deformation Features. *Meteorit. Planet. Sci.* **2005**, *40*(9-10), 1353–1361; doi: 10.1111/j.1945.5100.2005.tb00406.x.

[102] French, B.M.; Koeberl C. The Convincing Identification of Terrestrial Meteorite Impact Structures: What Works, What Doesn't, and Why. *Earth-Sci. Rev.* **2010**, *98*(1-2), 123–170; doi: 10.1016/j.earscirev.2009.10.009.

[103] Langenhorst, F. Shock Metamorphism of Some Minerals: Basic Introduction and Microstructural Observations. *Bull. Czech Geol. Surv.* **2002**, *77*(4), 265–282.

[104] Ferriere, L.; Osinski G.R. Shock Metamorphism. In *Impact Cratering: Processes and Products*; Osinski, G.R., Pierazzo, E., Eds.; John Wiley & Sons, 2012: pp. 106–124.

[105] French, B.M. Traces of Catastrophe: *A Handbook of Shock-Metamorphic Effects in Terrestrial Meteorite Impact Structures.* LPI Contribution 954. Lunar and Planetary Institute: Washington DC, 1998.

[106] Christie J.; Griggs D.; Carter N. Experimental Evidence of Basal Slip in Quartz. *J. Geol.* **1964**, *72*(6), 734–756; doi: 10.1086/627030.

[107] Christie, J.M.; Raleigh, C.B. The Origin of Deformation Lamellae in Quartz. *Am. J. Sci.* **1959**, *257*(6), 385–407; doi: 10.2475/ajs.257.6.385.

[108] Gratz, A. Deformation in Laboratory-Shocked Quartz. *J. Non-Cryst. Solids* **1984**, *67*(1-3), 543–558; doi: 10.1016/0022.3093(84)90175.3.

[109] McLaren, A.; Retchford, J.A.; Griggs D.T.; Christie J.M. Transmission Electron Microscope Study of Brazil Twins and Dislocations Experimentally Produced in Natural Quartz. *Phys. Status Solidi (B)* **1967**, *19*(2), 631–644; doi: 10.1002/pssb.19670190216.

[110] McLaren, A.; Turner, R.G.; Boland, J.N.; Hobbs, B.E. Dislocation Structure of the Deformation Lamellae in Synthetic Quartz; A Study by Electron and Optical Microscopy. *Contrib. Mineral. Petr.* **1970**, *29*, 104–115; doi: 10.1007/BF00392018.

[111] Kowitz, A.; Schmitt R.T.; Reimold U.; Hornemann U. The First MEMIN Shock Recovery Experiments at Low Shock Pressure (5–12.5 GPa) with Dry, Porous Sandstone. *Meteorit. Planet. Sci.* **2013**, *48*(1), 99–114; doi: 10.1111/maps.12030.

[112] Reimold W.U.; Koeberl, C. Impact Structures in Africa: A Review. *J. Afr. Earth Sci.* **2014**, *93*, 57–175; doi: 10.1016/j.jafrearsci.2014.01.008.

[113] Buchanan, P.; Reimold W. Planar Deformation Features and Impact Glass in Inclusions from the Vredefort Granophyre, South Africa. *Meteorit. Planet. Sci.* **2002**, *37*(6), 807–822; doi: 10.1111/j.1945.5100.2002.tb00857.x.

[114] Koeberl, C.; Reimold, W.U.; Cooper, G.; Cowan, D.; Vincent, P.M. Aorounga and Gweni Fada Impact Structures, Chad: Remote Sensing, Petrography, and Geochemistry of Target Rocks. *Meteorit. Planet. Sci.* **2005**, *40*(9-10), 1455–1471.

[115] Reimold, W.U.; Crósta, A.P.; Hasch, M.; Kowitz, A.; Hauser, N.; Sanchez, J.P.; Simões L.S.A.; de Oliveira G.J.; Zaag P.T. Shock Deformation Confirms the Impact Origin for the Cerro do Jarau, Rio Grande do Sul, Brazil, Structure. *Meteorit. Planet. Sci.* **2019**, *54*(10), 2384–2397; doi: 10.1111/maps.13233.

[116] Kowitz, A.; Güldemeister, N.; Schmitt, R.T.; Reimold, W.-U.; Wünnemann, K.; Holzwarth, A. Revision and Recalibration of Existing Shock Classifications for Quartzose Rocks using Low-Shock Pressure (2.5–20 GP a) Recovery Experiments and Mesoscale Numerical Modeling. *Meteorit. Planet. Sci.* **2016**, *51*(10), 1741–1761; doi: 10.1111/maps.12712.

[117] Kieffer, S.W. Shock Metamorphism of the Coconino Sandstone at Meteor Crater, Arizona. *J. Geophys. Res.* **1971**, *76*(23), 5449–5473; doi: 10.1029/JB076i023p05449.

[118] Kieffer, S.W.; Phakey P.P.; Christie J.M. Shock Processes in Porous Quartzite: Transmission Electron Microscope Observations and Theory. *Contrib. Mineral. Petr.* **1976**, *59*(1), 41–93; doi: 10.1007/BF00375110.

[119] Ernstson, K. Evidence of Meteorite Impact-Induced Thermal Shock in Quartz. In *Modern Problems of Theoretical, Experimental, and Applied Mineralogy*; 2020, pp. 1423.

[120] Ernstson, K. Meteorite Impact Spallation: from Mega- to Micro-Scale. Ernstson Claudin Impact Structures - Meteorite Craters 2014 May 3, 2023. Available online: http://www.impact-structures.com/impact-educational/meteorite-impact-spallation-from-mega-to-micro-scale/.

[121] Moore, C.R.; LeCompte, M.A.; Kennett, J.P.; Brooks, M.J.; Firestone, R.B.; Ivester, A.H.; Ferguson, T.A.; Lane, C.S.; Duernberger, K.A.; Feathers, J.K.; et al. Platinum, Shock-Fractured Quartz, Microspherules, and Meltglass Widely Distributed in Eastern USA at the Younger Dryas onset (12.8 ka). *Airburst. Cratering Impacts* **2024**, *2*.

[122] Wakita, S.; Johnson, B.C.; Adeene Denton, C.; Davison, T.M. Jetting During Oblique Impacts of Spherical Impactors. *Icarus* **2021**, *360*, 114365; doi: 10.1016/j.icarus.2021.114365.

[123] Jaret, S.J.; Scott Harris R. No Mineralogic or Geochemical Evidence of Impact at Tall el-Hammam, a Middle Bronze Age city in the Jordan Valley near the Dead Sea. *Sci. Rep.* **2022**, *12*(1), 5189–5193; doi: 10.1038/s41598.022.08216.x.

[124] Poelchau, M.; Kenkmann, T. Feather Features: A Low-Shock-Pressure Indicator in Quartz. *J. Geophys. Res. Solid Earth* **2011**, *116*(B2); doi: 10.1029/2010JB007803.

[125] Aftosmis, M.J.; Mathias, D.L.; Tarano A.M. Simulation-Based Height of Burst Map for Asteroid Airburst Damage Prediction. *Acta Astronaut.* **2019**, *156*, 278–283; doi: 10.1016/j.actaastro.2017.12.021.

[126] Artemieva, N.A.; Shuvalov V.V. From Tunguska to Chelyabinsk via Jupiter. *Annu. Rev. Earth Planet. Sci.* **2016**, *44*, 37–56; doi: 10.1146/annurev.earth.060115.012218.

[127] Robertson, D.K.; Mathias, D.L. Hydrocode Simulations of Asteroid Airbursts and Constraints for Tunguska. *Icarus* **2019**, *327*, 36–47; doi: 10.1016/j.icarus.2018.10.017.

[128] Boslough, M. Abstracts #U21E-03: Computational Modeling of Low-Altitude Airbursts. In *AGU Fall Meeting*, 2007.

[129] Collins, G.S.; Lynch, E.; McAdam, R.; Davison, T.M. A Numerical Assessment of Simple Airblast Models of Impact Airbursts. *Meteorit. Planet. Sci.* **2017**, *52*(8), 1542–1560; doi: 10.1111/maps.12873.

[130] Collins, G.S.; Melosh, H.J.; Marcus, R. Earth Impact Effects Program: A Web-Based Computer Program for Calculating the Regional Environmental Consequences of A Meteoroid Impact on Earth. *Meteorit. Planet. Sci.* **2005**, *40*(2), 817–840; doi: 10.1111/j.1945.5100.2005.tb00157.x.

[131] Shuvalov, V.; Artemieva, N.; Kosarev, I. 3D Hydrodynamic Code SOVA for Multimaterial Flows, Application to Shoemakerlevy 9 Comet Impact Problem. *Int. J. Impact Eng.* **1999**, *23*(1), 847–858; doi: 10.1016/S0734.743X(99)00129.3.

[132] Baldwin, E., Milner, D.J.; Burchell, M.J.; Crawford, I.A. Shock Wave Propagation and Damage to the Target in Oceanic Impact Events. In *Bridging the Gap II: Effect of Target Properties on the Impact Cratering Process*; 2007; Volume 1360, pp. 13–14.

[133] Baldwin, E.; Vocadlo, L.; Crawford, I. Validation of AUTODYN in Replicating Large-Scale Planetary Impact Events. In *36th Annual Lunar and Planetary Science Conference*; 2005, p. 1380.

[134] Robertson, N.J.; Hayhurst, C.J.; Fairlie, G.E. Numerical Simulation of Explosion Phenomena. *Int. J. Comput. Appl. Technol.* **1994**, *7*(3-6), 316–329; doi: 10.1504/IJCAT.1994.062536.

[135] Saito, T.; Kaiho, K.; Abe, A.; Katayama, M.; Takayama, K. Hypervelocity Impact of Asteroid/Comet on the Oceanic Crust of the Earth. *Int. J. Impact Eng.* **2008**, *35*(12), 1770–1777; doi: 10.1016/j.ijimpeng.2008.07.046.

[136] Saito, T.; Kaiho, K.; Abe, A.; Katayama, M.; Takayama, K. Numerical Simulations of Hypervelocity Impact of Asteroid/Comet on the Earth. *Int. J. Impact Eng.* **2006**, *33*(1-12), 713–722; doi: 10.1016/j.ijimpeng.2006.09.012.

[137] Birnbaum, N.K.; Cowler, M.; Hayhurst, C. Numerical Simulation of Impact Using AUTODYN. In *Proc. 2nd Int. Impact Sympo.*; 1996, Beijing, China.

[138] Deller, J.; Lowry, S.C.; Snodgrass, C.; Price, M.C.; Sierks, H. A New Approach to Modelling Impacts on Rubble Pile Asteroid Simulants. *Mon. Not Royal Astron. Soc.* **2016**, *455*(4), 3752–3762; doi: 10.1093/mnras/stv2584.

[139] Jones, A.P.; Price, D.G.; DeCarli, P.S.; Price, N.; Clegg, R. Impact decompression melting: a possible trigger for impact induced volcanism and mantle hotspots? In *Impact Markers in the Stratigraphic Record*; 2003, pp. 91–119.

[140] Nishizawa, M.; Matsui, Y.; Suda, K.; Saito, T.; Shibuya, T.; Takai, K.; Hasegawa, S.; Yano, H. Experimental Simulations of Hypervelocity Impact Penetration of Asteroids into the Terrestrial Ocean and Benthic Cratering. *J. Geophys. Res. Planets* **2020**, *125*(12), e2019JE006291; doi: 10.1029/2019JE006291.

[141] Stickle, A.; Barnouin, O.S.; Bruck Syal, M.; Cheng, A.; El-Mir, C.; Ernst, C.M.; Michel, P.; Oklay, N.; Owen, M.; Price, M.; et al. Impact Simulation Benchmarking for the Double Asteroid Redirect Test (DART). In *47th Annual Lunar and Planetary Science Conference*; 2016; Volume 1903, pp. 2832.

[142] Wie, B., et al. An Innovative Solution to NASA's NEO Impact Threat Mitigation Grand Challenge and Flight Validation Mission Architecture Development. 2014.

[143] Caldwell, W.K.; Euser, B.; Plesko, C.S.; Larmat, C; Lei, Z.; Knight, E.E.; Rougier, E.; Hunter, A. Benchmarking Numerical Methods for Impact and Cratering Applications. *Appl. Sci.* **2021**, *11*(6), 2504; doi: 10.3390/app11062504.

[144] Birnbaum, N.; Cowler, M.S.; Itoh, M.; Katayama, M.; Obata, H. AUTODYN-An Interactive Non-Linear Dynamic Analysis Program for Microcomputers through Supercomputers. In *Transactions of the 9th International Conference on Structural Mechanics in Reactor Technology;* 1987; Volume B.

[145] Marcus, R., Melosh, H.J.; Collins, G.S. Earth Impact Effects Program. 2004. Available online: https://impact.ese.ic.ac.uk/ImpactEarth/ImpactEffects/.

[146] Jenniskens, P.; Popova, O.P.; Glazachev, D.O.; Podobnaya, E.D.; Kartashova, A.P. Tunguska Eyewitness Accounts, Injuries, and Casualties. *Icarus*, **2019**, *327*, 4–18; doi: 10.1016/j.icarus.2019.01.001.

[147] Zlobin, A.E. Discovery of probably Tunguska meteorites at the bottom of Khushmo river's shoal. **2013**, arXiv preprint arXiv:1304.8070.

[148] Brown, P.G., Assink, J.D.; Astiz, L.; Blaauw, R.; Boslough, M.B.; Borovička, J.; Brachet, N.; Brown, D.; Campbell-Brown, M.; Ceranna, L.; et al. A 500-Kiloton Airburst over Chelyabinsk and An Enhanced Hazard from Small Impactors. *Nature* **2013**, *503*(7475), 238–241; doi: 10.1038/nature12741.

[149] Silber, E.A.; Boslough, M.; Hocking, W.K.; Gritsevich, M.; Whitaker, R.W. Physics of Meteor Generated Shock Waves in the Earth's Atmosphere–A Review. *Adv. Space Res.* **2018**, *62*(3), 489–532; doi: 10.1016/j.asr.2018.05.010.

[150] Zhilyaev, B.; Petukhov, V.N.; Reshetnyk, V.; Vidmachenko, A. Meteor Colorimetry with CMOS Cameras. arXiv preprint arXiv:2106.07403, 2021.

[151] Courty, M.A.; Coqueugniot, E. A Microfacies Toolkit for Revealing Linkages Between Cultural Discontinuities and Exceptional Geogenic Events: the Tell Dja'de Case Study (NE Syria). *J. Archaeol. Method Th.*, **2013**, *20*(2), 331–362.

[152] Courty, M.-A.; Crisci, A.; Fedoroff, M.; Grice, K.; Greenwood, P.; Mermoux, M.; Smith, D.; Thiemens, M. Regional Manifestation of the Widespread Disruption of Soil-Landscapes by the 4 kyr BP Impact-Linked Dust Event using Pedo-Sedimentary Micro-Fabrics. In *New Trends in Soil Micromorphology*, Springer, 2008; pp. 211–236; doi: 10.1007/978.3.540.79134.8_12.

[153] Courty, M.-A., The Soil Record of An Exceptional Event at 4000 BP in the Middle East. In *Natural Catastrophes During Bronze Age Civilisations: Archaeological, Geological, Astronomical and Cultural Perspectives*; 1998; pp. 93.

[154] Coqueugniot, E.; Courty, M. Cosmic Airburst Debris, Climate Anomalies and Societal Reactions at 4.2 kyr BP: From North Syria to Adelie Land. In *AGU Fall Meeting Abstracts*, 2012.

[155] Tankersley, K.B.; Meyers, S.A. The Eagle Station Impact Site. *N. Am. Archaeol.* **2023**, *44*(2-3), 103–114; doi: 10.1177/01976931231195111.

[156] Box, G.E., Science and Statistics. *J. Am. Stat. Assoc.* **1976**, *71*(356), 791–799; doi: 10.2307/2286841.

[157] Brown, P.G.; Hildebrand, A.R.; Zolensky, M.E.; Grady, M.; Clayton, R.N.; Mayeda, T.K.; Tagliaferri E.; Spalding, R.; MacRae, N.D.; Hoffman, E.L.; et al. The Fall, Recovery, Orbit, and Composition of the Tagish Lake Meteorite: A New Type of Carbonaceous Chondrite. *Science* **2000**, *290*(5490), 320–325.

[158] Brown, P.G.; ReVelle, D.O.; Tagliaferri, E.; Hildebrand, A.R. An Entry Model for the Tagish Lake Fireball using Seismic, Satellite and Infrasound Records. *Meteorit. Planet. Sci.* **2002**, *37*(5), 661–675; doi: 10.1111/j.1945.5100.2002.tb00846.x.

[159] Martel, L.M. *Better Know A Meteorite Collection: Natural History Museum in London, United Kingdom.* Planetary Science Research Discoveries Report; 2009; pp. 136.

[160] Bronk Ramsey, C. *Analysis Examples.* 2013 [cited 2021 October 6]. Available online: https://c14.arch.ox.ac.uk/oxcalhelp/hlp_analysis_eg.html.

[161] Bronk Ramsey, C. *Analysis Operations and Models.* 2013 [cited 2021 Oct 6]. Available online: http://c14.arch.ox.ac.uk/oxcalhelp/hlp_analysis_oper.html.

[162] Pierazzo, E.; Artemieva, N.; Asphaug, E.; Baldwin, E.C.; Cazamias, J.; Coker, R.; Collins, G.S.; Crawford, D.A.; Davison, T.; Elbeshausen, D.; et al. Validation of Numerical Codes for Impact and Explosion Cratering: Impacts on Strengthless and Metal Targets. *Meteorit. Planet. Sci.* **2008**, *43*(12), 1917–1938; doi: 10.1111/j.1945.5100.2008.tb00653.x.

[163] Svetsov, V.B. Thermal Radiation on the Ground from Large Aerial Bursts caused by Tunguska-Like Impacts. In *Lunar and Planetary Science XXXVII*; 2006; pp. 1–2.

[164] Longo, G. The Tunguska Event. In *Comet/Asteroid Impacts and Human Society: An Interdisciplinary Approach*; 2007; pp. 303–330.

[165] Marcus, R.; Melosh, H.J.; Collins, G.S. *Earth Impact Effects Program, Examples*. 2004 [cited 2024 April, 2024]. Available online: https://impact.ese.ic.ac.uk/ImpactEarth/ImpactEffects/examples.html.

[166] Kletetschka, G.; Vyhnanek, J.; Kawasumiova, D.; Nabelek, L.; Petrucha, V. Localization of the Chelyabinsk Meteorite from Magnetic Field Survey and GPS Data. *IEEE Sensors J.* **2015**, *15*(9), 4875–4881; doi: 10.1109/JSEN.2015.2435252.

[167] Popova, O.P.; Jenniskens, P.; Emel'yanenko, V.; Kartashova, A.; Biryukov, E.; Khaibrakhmanov, S.; Shuvalov, V.; Rybnov, Y.; Dudorov, A.; Grokhovsky, V.I.; et al. Chelyabinsk Airburst, Damage Assessment, Meteorite Recovery, and Characterization. *Science* **2013**, *342*(6162), 1069–1073; doi: 10.1126/science.1242642.

[168] Kocherov, A.; Korochantsev, A.V.; Lorenz, C.A.; Ivanova, M.A.; Grokhovsky, V.I. Recovery, Laboratory Preparation and Current State of the Main Mass of the Chelyabinsk Meteorite. In *45th Annual Lunar and Planetary Science Conference*; 2014; Volume 1777, pp. 2227.

[169] Svetsov, V.; Shuvalov, V.; Kosarev I. Formation of Libyan Desert Glass: Numerical Simulations of Melting of Silica due to Radiation from Near-Surface Airbursts. *Meteorit. Planet. Sci.* **2020**, *55*(4), 895–910; doi: 10.1111/maps.13470.

[170] Stankowski, W.; Katrusiak A.; Budzianowski A. Crystallographic Variety of Magnetic Spherules from Pleistocene and Holocene Sediments in the Northern Foreland of Morasko-Meteorite Reserve. *Planet. Space Sci.* **2006**, *54*(1), 60–70; doi: 10.1016/j.pss.2005.08.005.

[171] Blanco P., Nicolás; Vásquez I., Paulina; Sepúlveda V., Fernando; Tomlinson, Andrew J.; Quezada J., Andrés; Ladino U., Marco. Levantamiento geológico para el fomento de la exploración de recursos minerales e hídricos de la Cordillera de la Costa, Depresión Central y Precordillera de la Región de Tarapacá (20-21 S). Servicio Nacional de Geología y Minería, Informe Registrado IR-12-50; 2012; Volume 7.

[172] Boslough, M.; Schultz, P.; Harris R. *Hypervelocity Airburst Shower Formation of the Pica Glass.* LPI Contributions No. 2702; 2022; pp. 2021.

[173] Osinski, G.; Haldemann, A.F.C.; Schwarcz, H.P.; Smith, J.R.; Kleindienst M.R. Impact Glass at the Dakhleh Oasis, Egypt: Evidence for a Cratering Event or Large Aerial Burst? In *38th Annual Lunar and Planetary Science Conference*; 2007; Volume 1338, pp. 1346.

[174] Van Ginneken, M.; Folco, L.; Perchiazzi, N.; Rochette, P.; Bland, P.A. Meteoritic Ablation Debris from the Transantarctic Mountains: Evidence for a Tunguska-Like Impact over Antarctica ca. 480 ka ago. *Earth Planet. Sci. Lett.* **2010**, *293*(1-2), 104–113; doi: 10.1016/j.epsl.2010.02.028.

[175] Van Ginneken, M.; Suavet, C.; Cordier, C.; Folco, L.; Rochette, P.; Sonzogni, C.; Perchiazzi, N. Oxygen Isotope Composition of Meteoritic Ablation Debris from the Transantarctic Mountains: Constraining the Parent Body and Implications for the Impact Scenario. *Meteorit. Planet. Sci.* **2012**, *47*(11), 1738–1747; doi: 10.1111/maps.12011.

[176] McHone, J.; Killgore M.; Kudryavtsev A. Cristobalite Inclusions in Libyan Desert Glass; Confirmation using Raman Spectroscopy. In *Lunar and Planetary Science Conference*; 2000; pp. 1877.

[177] Pratesi, G.; Viti, C.; Cipriani, C.; Mellini M. Silicate-Silicate Liquid Immiscibility and Graphite Ribbons in Libyan Desert Glass. *Geochim. Cosmochim. Acta* **2002**, *66*(5), 903–911; doi: 10.1016/S0016.7037(01)00820.1.

[178] Kleinmann, B.; Horn, P.; Langenhorst, F. Evidence for Shock Metamorphism in Sandstones from the Libyan Desert Glass Strewn Field. *Meteorit. Planet. Sci.* **2001**, *36*(9), 1277–1282; doi: 10.1111/j.1945.5100.2001.tb01960.x.

[179] Koeberl, C.; Ferrière, L. Libyan Desert Glass Area in Western Egypt: Shocked Quartz in Bedrock Points to a Possible Deeply Eroded Impact Structure in the Region. *Meteorit. Planet. Sci.* **2019**, *54*(10), 2398–2408; doi: 10.1111/maps.13250.

Appendices

Appendix: Text

Appendix: Site setting

This section is adapted from Bunch et al. [1] and reproduced here for reference. The site is situated on a raised, two-tiered occupational mound, the largest in the Jordan Valley (Figure 1B). The site represents the urban core of a city-state that flourished for ~3000 years from the Chalcolithic Period through the Bronze Age. However, Bunch et al. [1] and this contribution more narrowly focus on the city's destruction around 3600 calendar years before 1950 A.D. (cal BP).

Appendix: Melted materials

For context, it is essential to understand Bunch et al.'s initial discovery of melted materials. [1] (Figures 1 and 2; Appendix, Figures A1–A4). Therefore, we have reproduced selected photographs and figures of melted materials first presented by Bunch et al. [1] supporting the hypothesis that a touch-down airburst destroyed Tall el-Hammam. General sampling locations are as shown in Figures 1B and 2.

Appendix: Stratigraphy of Tall el-Hammam

This section, summarized from Bunch et al. [1], is relevant for the stratigraphic context. All sampling profiles examined at Tall el-Hammam contain a complex Middle Bronze Age burn layer. While this layer varies in composition across the tall, it generally consists of three main units. The deepest unit consists mainly of pulverized mudbrick mixed with melted and unmelted mudbrick fragments, melted and unmelted roofing clay, ash, charcoal, charred seeds, unburnt wood, burned textiles, burned and unburnt bones, plaster fragments, broken pottery, and melted pottery. We call this unit the "terminal destruction layer." [3] This unit varies in thickness up to ~2 m and is only occasionally missing across the upper tall and mostly missing across the lower tall, primarily due to agricultural disturbance. Also, about a dozen modern military excavations for artillery emplacements are found across the site, but these disturbances are absent in the areas sampled for this study and in Bunch et al. [1]

The second unit, immediately above the destruction layer, is composed of thin, windblown, fine-grained laminations, including fragments of broken plaster, limestone spherules, and charcoal, radiocarbon-dated to ~1650 BCE. This unusual unit is called the "blow-over layer" [1, 71]. Nothing similar has been identified in any older or younger deposits at the site, beginning in the Early Bronze Age and extending through the Iron Age.

The uppermost unit is a charcoal-and-ash-rich stratum called the "dark layer" [1], which is ubiquitous across the tall and ranges from a few cm to ~1 m thick. Its burial depth varies considerably from being near the surface on parts of the lower tall to being buried 1-4 m across most of the upper tall.

The three units collectively make up the "terminal destruction layer." This layer is nearly always sealed by a culturally sterile layer that has not been disturbed by subsequent human activities, including modern warfare.

Our investigations focused on suites of samples spanning the terminal destruction layer at four sampling sites. The three sites in the city are separated by up to ~500 m laterally, covering an area of 5.7 hectares (0.057 km^2), and the wadi site extends the total horizontal distance to 1500 m for all four sites (Figure 1B). All airburst proxies investigated here and in Bunch et al. [1] came from these four sampling sites. See Bunch et al. [1] and their Supporting Information for more details and maps. Samples from the sites below were collected by co-authors of this paper and Bunch et al., including P.J.S., M.A.L., E.C.S., T.W., G.K., and G.A.H. with assistance from co-author S.C. and members of the Tall el-Hammam Excavation Project (TeHEP).

Palace: the sampled location is at ~132 meters below sea level (mbsl) on the upper tall. Bunch et al. [1] sampled a 28-cm-thick sequence from within the terminal destruction layer, the top of which is at ~360 cm depth below the surface. Five contiguous samples each had an average thickness of 5.6 cm (range: 3-13 cm).

Temple: the sampled location is at ~155 mbsl on the lower tall. Bunch et al. [1] sampled a 43-cm-thick sequence where the top of the terminal destruction layer is 54 cm below the surface. Five contiguous samples had an average thickness of 8.6 cm (range: 6-16 cm).

Ring road: the sampled location is at ~157 mbsl on the road that ringed the lower city inside the city wall. The top of the 30-cm sequence is at a depth of 22 cm, with the terminal destruction layer at 42 cm. Six contiguous samples each had thicknesses of 5 cm.

Wadi: the sampled location is at an elevation of ~197 mbsl along a short seasonal stream located beyond the southern boundary of the tall. Bunch et al. [1] sampled a 170-cm-thick sequence beginning ~100 cm below the surface with the top of the terminal destruction layer at ~160 cm below the surface. Five discontinuous samples had an average thickness of ~13.2 cm (range: 10-20 cm).

Appendix: Destruction of the palace

This section is adapted from Bunch et al. [1] and reproduced here for reference. The excavations revealed that nearly all of the ~4-5-story-tall palace is missing, except for a few courses of mudbricks still present on the stone foundations (Figure A3B). Importantly, there is no evidence across the entire site of walls that collapsed vertically in place; instead, wall debris is distributed laterally across tens of meters from SW to NE. Almost no whole mudbricks are visible anywhere,

and instead, pulverized and fragmented mudbricks fill the churned-up, 2-m-thick destruction matrix. Most of the original mass of mudbricks appears to have been shattered and blown off the tall to the NE [1]. (Figures A3, A4). For reference, the following figures and captions are reproduced from Bunch et al. [1].

Appendix: Fragmentation of bolides

This section is adapted from West et al. [9] and reproduced here for reference. West et al. [9] noted that meteoritic airbursts typically produce multiple fragments that reach the ground, usually at terminal velocity for the high-altitude ones; the velocity increases at lower altitudes. (i) The Tagish Lake meteorite (4-6 m in diameter, 56 tonnes) burst ~29 km high. It produced an elliptical strewn field 5 km by 16 km long containing >10,000 fragments up to ~2.3 kg, each of which reached the surface at low velocities [157, 158]; (ii) the Sikhote-Alin iron meteorite struck Siberia in 1947, distributing ~8500 pieces totaling more than 23,000 kg across 1.6 km^2, creating more than 100 impact craters ranging from 0.5–26 m in diameter [159]; and (iii) Argentina's Campo del Cielo meteorite field was represented by >100 meteorites, some of which formed craters up to 26.5 m in diameter and 6 m in depth. The Sikhote-Alin and Campo del Cielo airbursts produced shock-generated craters, i.e., shock pressures from the airbursts were high enough to excavate unconsolidated surficial sediment.

Appendix: Bayesian analysis, Table A1

This section is adapted from Bunch et al. [1] and reproduced here for reference. Twenty radiocarbon dates on material from the destruction layer. All dates are from the palace (Field UA). The Bayesian-calculated age is 1661 BCE ± 21 cal BP (3611, rounded to 3600 cal BP) for a likely range of 1686 to 1632 BCE at 68% CI. Calculated using the Combine feature of the OxCal program, version 4.4.3, IntCal20 calibration curve. From Bunch et al. [1], usable under Creative Commons, CC by 4.0 (http://creativecommons.org/licenses/by/4.0/).

Two functions in OxCal are used to combine dates from a single inferred event. The 'R_Combine' function combines two or more radiocarbon dates from the same source, e.g., a single skeleton [160, 161]. The 'Combine' function combines two or more radiocarbon dates from different sources that are believed to be coeval, e.g., the date that beams were used to build a cathedral [160, 161]. The 'Combine' routine is the one used in Bunch et al. [1], because there were different radiocarbon sources, e.g., charred palace beams and charred seeds. The presence of tens of thousands of pieces of charcoal, wood, melted mudbricks, melted pottery, and melted spherules randomly mixed throughout a single unstratified, unconsolidated stratum strongly supports the hypothesis that they represent a single city-wide episode of biomass burning. Thus, the 'Combine' function is the appropriate OxCal routine.

Table A1: Bayesian analyses for Tall el-Hammam.

Tall el-Hammam			Unmodelled (BCE/CE)						Modelled (BCE/CE)						Indices	
			68% CI		95% CI				68% CI		95% CI					
20 ¹⁴C dates	¹⁴C	±	From	To	From	To	sigma	mu	From	To	From	To	sigma	mu	Acomb A	Material dated
Combine			-1686	-1632	-1689	-1628	21	-1661	-1686	-1632	-1689	-1628	21	-1661	143.6	
R_Date Beta-494574	3420	30	-1751	-1636	-1873	-1622	61	-1719	-1686	-1632	-1689	-1628	21	-1661	80.1	Carbonized wood
R_Date Beta-494577	3420	30	-1751	-1636	-1873	-1622	61	-1719	-1686	-1632	-1689	-1628	21	-1661	80.1	Carbonized wood
R_Date Beta-477409	3410	30	-1744	-1636	-1870	-1619	56	-1704	-1686	-1632	-1689	-1628	21	-1661	101	Carbonized wood
R_Date Beta-494575	3400	30	-1739	-1631	-1866	-1615	52	-1690	-1686	-1632	-1689	-1628	21	-1661	114	Carbonized wood
R_Date Beta-494576	3400	30	-1739	-1631	-1866	-1615	52	-1690	-1686	-1632	-1689	-1628	21	-1661	114	Carbonized wood
R_Date Beta-589019	3400	30	-1739	-1631	-1866	-1615	52	-1690	-1686	-1632	-1689	-1628	21	-1661	114	Carbonized material
R_Date Beta-490628	3390	30	-1736	-1626	-1863	-1564	49	-1679	-1686	-1632	-1689	-1628	21	-1661	122	Burned bone
R_Date Beta-589000	3390	30	-1736	-1626	-1863	-1564	49	-1679	-1686	-1632	-1689	-1628	21	-1661	122	Carbonized wood
R_Date Beta-589016	3390	30	-1736	-1626	-1863	-1564	49	-1679	-1686	-1632	-1689	-1628	21	-1661	122	Carbonized material
R_Date Beta-589020	3390	30	-1736	-1626	-1863	-1564	49	-1679	-1686	-1632	-1689	-1628	21	-1661	122	Carbonized wood
R_Date Beta-494573	3380	30	-1733	-1623	-1747	-1544	49	-1667	-1686	-1632	-1689	-1628	21	-1661	127	Carbonized wood
R_Date Beta-589001	3380	30	-1733	-1623	-1747	-1544	49	-1667	-1686	-1632	-1689	-1628	21	-1661	127	Carbonized grain
R_Date Beta-484763	3370	30	-1733	-1617	-1743	-1542	50	-1655	-1686	-1632	-1689	-1628	21	-1661	129	Organic sediment
R_Date Beta-490631	3370	30	-1733	-1617	-1743	-1542	50	-1655	-1686	-1632	-1689	-1628	21	-1661	129	Carbonized material
R_Date Beta-589006	3370	30	-1733	-1617	-1743	-1542	50	-1655	-1686	-1632	-1689	-1628	21	-1661	129	Carbonized wood
R_Date Beta-589007	3370	30	-1733	-1617	-1743	-1542	50	-1655	-1686	-1632	-1689	-1628	21	-1661	129	Carbonized wood
R_Date Beta-589008	3370	30	-1733	-1617	-1743	-1542	50	-1655	-1686	-1632	-1689	-1628	21	-1661	129	Carbonized wood
R_Date Beta-494579	3350	30	-1686	-1545	-1736	-1536	53	-1625	-1686	-1632	-1689	-1628	21	-1661	103	Carbonized grain
RDate Beta-589017	3350	30	-1686	-1545	-1736	-1536	53	-1625	-1686	-1632	-1689	-1628	21	-1661	103	Carbonized material
R_Date Beta-494580	3330	30	-1624	-1540	-1687	-1517	47	-1595	-1686	-1632	-1689	-1628	21	-1661	39.7	Carbonized grain

Table A2: Location of oriented materials by excavation pit.

	Directional sherds	Melted pottery	Melted bricks/clay	Directional debris	Directional grains	Source
LA-Ring Road						
28M				NE		Bunch et al. 2021 [1]
29M			NE	NE		Collins et al. 2019 [72]
Temple--LS						
38N			NE	NE		Collins, pers., 2021 [83]
38O			NE	NE		Collins, pers., 2021 [83]
42J				NE		Bunch et al. 2021 [1]
42K				NE		Bunch et al. 2021 [1]
43K		NE				Silvia, 2015 [4]
Ring Road--LA						
19U						
20U		NE	NE	NE		Collins et al. 2019, 2017 [3, 72]
Palace--UA						
6FF	NE			NE	NE	Collins et al. 2019, 2017 [3, 72]
6GG	NE		NE	NE		Collins et al. 2019, 2017 [3, 72]
6HH	NE			NE		Collins et al. 2019, 2017 [3, 72]
7FF	NE		NE	NE	NE	Collins et al. 2019, 2017 [3, 72]
7GG	NE	NE	NE	NE	NE	Collins et al. 2019, 2017 [3, 72]; Bunch et al. 2021 [1]
7HH	NE	NE	NE	NE	NE	Collins et al. 2019, 2017 [3, 72]; Bunch et al. 2021 [1]
8GG	NE		NE	NE		Collins et al. 2019, 2017 [3, 72]
8HH	NE		NE	NE		Collins et al. 2019, 2017 [3, 72]
10JJ		NE				Collins et al. 2019 [72]; Bunch et al. 2021 [1]
15DD				NE		
Upper Gate--UB						
19U						
20U		NE	NE	NE		Collins et al. 2019, 2017 [3, 72]
Housing--UC						
21SS	NE		NE	NE		Collins et al. 2019 [72]
FREQUENCY	9 of 19	6 of 19	12 of 19	18 of 19	4 of 19	

Appendix: Oriented materials, Table A2

Sampling locations and the numbers of each excavated square are listed at left. Results are shown for oriented trails of potsherds, melted pottery, melted mudbricks and clay, directional laminated debris (referred to as "blow-over" in Bunch et al. [1]), and directional trails of grains, such as barley. The average directionality was SW-NE, noted at "NE," but often varied by approximately ± 25°. Published sources for the observed directionality are as shown.

Appendix: Autodyn modeling

This section is adapted from West et al. [9] and reproduced here for reference. Autodyn is particularly useful in modeling complex physical phenomena, including the interaction of liquids, solids, and gases; determining the phase transitions of multiple modeled materials; and illustrating the propagation of pressure, temperature, shock speed (defined here as the velocity of the airburst-induced pressure wave that propagates through air and various materials, often at hypersonic velocities), and bulk material failure (defined as the point at which strain on a material exceeds a specified pressure value in the tensile direction).

Concerning Autodyn's utility, Pierazzo et al. [162] compared Autodyn with other commonly used modeling codes, including SOVA, SPH, iSALE, CTH, and ALE3D, and then compared those models with physical experiments. Those authors found Autodyn to agree well with the other code models and the experimental results [162]. They found that increasing the impact velocity adversely affected the accuracy of predicted peak pressures, but even so, they found Autodyn and other codes to be in good overall agreement with each other and with real-world experiments [162]. Baldwin et al. [133] concluded that Autodyn was able to replicate their laboratory impact experiments and used them to model large planetary impacts. However, both studies focused only on typical crater-forming impacts rather than airbursts.

Appendix: Testing the accuracy of modeling

This section is adapted from West et al. [9] and reproduced here for reference. In a test of Autodyn's accuracy, West et al. [9] compared the model of the Trinity nuclear detonation with the available real-time recorded data and found Autodyn's model to be consistent with the recorded data. Those authors also compared modeling by the EIEP with that of known airbursts. They wrote that it is challenging to determine modeling accuracy because there are no scientifically recorded direct observations of the effects of touch-down airbursts with which to make comparisons. However, two modern observed high-altitude airbursts can be compared using the EIEP. The following is quoted from their article.

Tunguska: Russia. West et al. [9] reviewed the high-altitude airburst at Tunguska in 1908. The blast yield of this airburst is estimated at ~3-30 megatons of TNT equivalent with a burst altitude of ~5-10 km. The airburst generated a shock wave that toppled or snapped >80 million trees across ~2000 km² in a radial pattern [51, 84, 163, 164]. Estimated surface wind velocities were ~40-70 m/s (144-250 km/h), greater than an EF-3 tornado [127], and the airburst ignited fires that consumed ~500 km² of forest [163]. The blast from this relatively small high-altitude airburst is reported to have killed ~3 of the ~30 people near ground zero, and nearly everyone experienced severe burns within an eight-km radius. [146] The comparison between the modeled and actual values (Appendix, Table A3) shows good correspondence (factor: −0.23 to +1.1 times).

Table A3: Tunguska data from the EIEP.

Tunguska	EIEP values	Actual values	Factor	Source
Diameter	60 m			Marcus et al. 2004 [145]
Density	2700 kg/m³			Marcus et al. 2004 [145]
Velocity	20 km/s	20-40 km/s		Marcus et al. 2004 [145]
Entry angle	45°	5°-45°		Marcus et al. 2004 [145]
Airburst height	5.74 km	6-12 km	>1.1×	Jenniskens et al. 2019 [146]
Airburst energy	13.4 Mt	10-15 Mt	=	Jenniskens et al. 2019 [146]
Fragments struck Earth	Yes	Yes?	≈	Zlobin 2013 [147]
Overpressure	130-260 kPa	10-30 kPa	~0.23×	Jenniskens et al. 2019 [146]
Max wind velocity	211 m/s	40-70 m/s	~0.33×	Jenniskens et al. 2019 [146]
Trees, 90% blown down	Yes	Yes	=	Jenniskens et al. 2019 [146]

Appendix: Table A3. Tunguska, comparison of actual to modeled values

First, we entered the top four variables into the EIEP using the same values presented online by Marcus et al. [165] in their use of the EIEP for Tunguska. Next, we compared the EIEP output with known or estimated values for the Tunguska high-altitude airburst. Actual values were either equal (three values) or different by ~0.23 to 1.1 times (three values), a reasonable difference. The table is from West et al. [9], usable under Creative Commons, CC by 4.0 (http://creativecommons.org/licenses/by/4.0/).

Chelyabinsk, Russia. West et al. [9] reviewed another airburst over Chelyabinsk. It occurred in 2013 at a height of ~29.7 km with an energy of ~500 kt [11, 126, 166–167]. The bolide underwent cascading fragmentation prior to the final airburst, which ejected numerous meteorite fragments, two of which weighed 64.7 and 540 kg [168]. The fragments struck Earth's surface at low velocities, with the largest creating a 9-m diameter hole in a frozen lake. Even though this airburst occurred high above the Earth's surface, the shockwave injured nearly 1500 people on the ground, mostly from flying glass and other debris. The comparison between the modeled and actual values (Appendix, Table A4) shows good correspondence (factor: −0.0 to +2.0 times). Given the lack of detailed information about touch-down airbursts, the use of EIEP is acceptable in this study as a first-order approximation.

Table A4: Chelyabinska data from the EIEP.

Chelyabinsk	EIEP values	Actual values	Factor	Source
Diameter	22 m	-	-	Marcus et al. 2004 [145]
Density	3300 kg/m³	-	-	Marcus et al. 2004 [145]
Velocity	19 km/s	-	-	Marcus et al. 2004 [145]
Entry angle	20°	-	-	Marcus et al. 2004 [145]
Airburst height	28.4 km	27-33 km	=	Brown et al. 2013 [148]
Airburst energy	350 kt	400-600 kT	>1.1×	Brown et al. 2013 [148]
Fragments struck Earth	Yes	Yes	=	Brown et al. 2013 [148]
Overpressure	2160 Pa	2600-4200 Pa	>1.2×	Brown et al. 2013 [148]
Max wind velocity	2.54 m/s	5.5-9.5 m/s	>2×	Brown et al. 2013 [148]
Shattered windows	Yes	Yes	=	Brown et al. 2013 [148]

Appendix: Table A4. Chelyabinsk, comparison of actual to modeled values

First, we entered the top four variables into the EIEP using the same values presented online by Marcus et al. [165] in their use of the EIEP for Chelyabinsk. Next, we compared the EIEP output with known or estimated values for the Chelyabinsk high-altitude airburst. For six key parameters, actual values were either equal (three values) or different by ~1.1 to 2.0 times (three values). The table is from West et al. [9], usable under Creative Commons, CC by 4.0. (http://creativecommons.org/licenses/by/4.0/).

Appendix: Previous hydrocode modeling of airbursts

To investigate a possible airburst origin of Libyan Desert glass, Svetsov et al. [169] produced a hydrocode model similar to that used in this study. This model demonstrated that a touch-down airburst could have produced the glass instead of a typical crater-forming impact. Likewise, Boslough and Crawford [65] produced a hydrocode airburst model for Libyan Desert glass using a 120-meter-diameter sphere to represent an asteroid with an initial velocity of 20 km/s, a kinetic energy of about 108 megatons, and a maximum temperature of 5800 K. The caption of Boslough and Crawford's Fig. 8 states that the model produced a "*low-altitude airburst for which the fireball descends to the surface,*" and their figure shows that it excavated a multi-meter-deep crater under the airburst [65]. They reported that "*the resulting fireball (which contains air and ablated meteoritic material at temperatures exceeding the melting temperature of quartz) makes direct contact with the surface over a 10 km diameter area for more than 10 s after the explosion.*" [65].

Supporting the results of this study, Robertson and Mathias [127] produced hydrocode models showing that 100-m-wide bolides typically burst close to the ground and that even 50-m-wide bolides "*can have a significant effect on the ground damage.*" Regarding airbursts in general, Boslough [6] wrote, "*Among the resulting discoveries has been the recognition that airbursts caused by downwardly directed collisions do more damage at the surface than a nuclear explosion of the same yield. They are therefore more dangerous than previously thought.*"

Thus, considerable previous physical and theoretical evidence exists that airbursts can, under the right conditions, (i) cause significant damage to the Earth's surface, (ii) produce shallow craters, (iii) produce multiple fragments that reach the ground, (iv) produce shock-fractured quartz, (v) produce meltglass, and (vi) form microspherules. Our contribution presents hydrocode models of a subset of these events, in which touch-down (Type 2) airbursts occur at an altitude low enough for the high-velocity jet of vapor and fragments to damage Earth's surface, creating shallow craters. In particular, we explored the conditions under which touch-down airbursts produce fragments traveling at velocities higher than a few km/s that are capable of producing shock-fractured

quartz, microspherules, and meltglass. Note that this model represents just one set of parameters, and the problem does not have a unique solution. Impactors with the diameters studied here can have numerous combinations of density, velocity, and angle of entry that will produce major variations in burst heights and surface damage. Nevertheless, all the evidence indicates that a wide range of touch-down airbursts can produce all the evidence observed at Tall el-Hammam.

Appendix: Airburst examples

The Chrudim/Pardubice strewn field covers ~135 km of the Czech Republic [12, 13]. This proposed Holocene-aged airburst produced extensive clusters of small craters containing meltglass, glass-filled fractured quartz, glass-like carbon, and multiple shock effects in polymictic breccias, including planar deformation features (PDFs), diaplectic glass, and silicate ballen structures (defined as a polycrystalline aggregate marked curved interfaces between crystallites).

An airburst event produced the Holocene-age Nalbach/Saarlouis (Saarland in Germany) strewn field with a minimum length of 15 km, containing two primary craters, one 250 m in diameter and the other 2.3 km [14–16]. Both craters feature densely extended surficial occurrences of impactites, such as strongly shocked polymictic breccias (PDFs, diaplectic glass, silica ballen structures, toasted quartz), impact glasses, melt rocks, and shatter cones.

On the plains of Kansas ~2600 years ago and in Hopewell Native American villages in Ohio ~1600 years ago, the discovery of meltglass, microspherules, and micrometeorites indicates the occurrence of two large asteroid airbursts [34, 35].

In the Chiemgau district of southeast Germany, extensive evidence exists of a significant Holocene-age airburst event [17–27]. The Chiemgau field is roughly elliptical, covering an area of about 60 km by 30 km (1,800 km²) and containing more than 100 impact craters ranging from a few m to 1,300 m. The strewn field displays shocked quartz, feldspar and mica, glass-filled fractured quartz, microspherules, microtektites, meltglass, glass-covered cobbles, ballen quartz structures, toasted quartz, shock-spallation cobble deformations, and shatter cones. The Chiemgau event can be dated to ~2900-2600 years ago in the Bronze Age/Celtic Era, using a unique new kind of impact rock, artifact-in-impactites, in which culturally datable artifacts are embedded in melted impact rocks [21, 22].

Approximately 5000 years ago, an iron meteorite produced an airburst that formed the Morasko strewn field in Poland, comprised of seven impact craters with diameters ranging from 20 to 90 m [36]. Bronikowska et al. [36] used hydrocode modeling to determine that the impactor mass was between 600 and 1100 tons, the entry velocity was between 16 and 18 km/s, and the trajectory angle was 30–40°. The airburst produced numerous microspherules [168].

An airburst/impact event is proposed to have produced a 50-km-wide strewn field in the Niederrhein region in

Germany, where there are dozens of small craters (100 to 200 m wide) [28]. A considerable mass of stony meteorites has been recovered from 40 locations, most likely from a rubble-pile asteroid. The evidence includes highly vesicular meltglass with native iron inclusions, polymictic breccia, diaplectic glass, shock-fractured quartz, and shocked feldspar. The age is unclear, but the event is estimated to be most likely from the Holocene but no older than the middle Pleistocene.

A large ~12,500-year-old strewn field of meltglass has been reported in a 75-km-long narrow corridor of the Atacama Desert in Chile [37–39]. Some have attributed the glass to a low-angle, low-altitude airburst. The field is divided into six main areas, each 1 to 3 km^2 in size and containing numerous meltglass clusters covering 1 to >100 m^2. The studies reported twisted and folded silicate glasses up to 4 m in diameter and up to 15-25 cm thick [171], containing meteoritic grains [39] and shocked quartz grains [171]. Boslough et al. [172] attribute the 75-km-long field of meltglass to "*low-altitude airbursts from six fragments of a single 120-m diameter comet* [that] *generated separate airbursts.*" This glass also contains fossil remains of plants on the surface at the time of the airburst.

At the 12,800-year-old Younger Dryas Boundary (YDB), numerous studies have reported peak abundances of shock-fractured quartz, nanodiamonds, meltglass, microspherules, soot and charcoal from impact-related biomass burning, and platinum-iridium anomalies [40–58]. These widespread impact proxies are suggested to have resulted from multiple hemispheric airbursts, some high-altitude and some as touch-downs, caused by the Earth's collision with dust and fragments in the tail of a comet [54, 59, 60].

Osinski et al. and others [61–63] reported large quantities of meltglass produced ~145,000 years ago at the Dakhleh Oasis in Egypt. The glass was discovered near the oasis at six locations separated by >40 km across ~400 km^2. The glass contains melted silica (lechatelierite, which forms at >1700 °C), shock-fractured quartz, and microspherules [61, 173]. Notably, Dakhleh glass also contains imprints and fossil remains of plants growing along the shores of the oasis at the time of the airburst. Smith et al. [63] used the EIEP to model the effects of the Dakhleh Oasis airburst.

Van Ginneken et al. [7, 8] describe two near-surface airbursts in Antarctica, one ~430,000 years old and a second one ~2.3 Myr old, the oldest ever discovered, in which high-pressure, high-velocity, high-temperature jets intersected the surface [8, 174, 175]. In the younger event, the touch-down airburst distributed melted microspherules across a radius of up to ~1400 km (2×10^6 km^2) [174].

The Libyan Desert glass field is attributed to a cosmic event ~29 million years ago. The field extends across ~6500 km^2 of the desert in Egypt [64] and is estimated to contain 1400 tonnes of meltglass [169], microspherules [176, 177], and shocked quartz [178, 179]. Because no crater has been discovered, some have proposed that a low-altitude airburst produced the field [65, 128]. However, other studies interpret the presence of shocked quartz [178, 179] as evidence that a typical impact crater exists but remains undiscovered. Alternatively, Hermes et al. [10] showed that airbursts can produce glass-filled, shock-fractured quartz without requiring a typical crater-forming impact.

Many other proposed airbursts have been described, including the following. (i) More than a dozen small craters, including one 300 m in diameter, as part of Germany's Holocene-age Lower Franconia strewn field [29]. (ii) The Pleistocene/Holocene-aged ~25-km-wide Sachsendorf Bay structure, a proposed airburst/impact crater in northeastern Germany [30]. (iii) The Luzice melt rock and megabreccia outcrops, proposed as evidence of a low-altitude airburst [32]. (iv) The 20-km-diameter Kolesovice airburst crater in the Czech Republic [33]. (v) A 6400-year-old strewn field of 33 craters up to 100 m in diameter in Finland [31].

Appendix: Methods
Shock-fractured quartz
We employed a comprehensive suite of ten analytical techniques to study polished, thin-sectioned slides. The techniques included optical transmission microscopy (OPT), epi-illumination microscopy (EPI), scanning electron microscopy (SEM), energy dispersive spectroscopy (EDS), focused ion beam milling (FIB), transmission electron microscopy (TEM), scanning transmission electron microscopy (STEM), fast-Fourier transform (FFT), electron backscatter diffraction (EBSD), and cathodoluminescence (CL). All procedures and instruments followed Hermes et al. [10] and Moore et al. [46] Each slide was carefully searched for candidate grains of shock-fractured quartz using optical and transmission microscopy. Grains exhibiting closely spaced, oriented fractures were considered candidates for shock-fractured quartz, with each requiring focused investigations using multiple techniques.

Directionality of debris
The archaeologists from Trinity Southwest University, including co-authors S.C. and P.J.S., determined the average directionality of most debris from SW to NE (range: approximately ± 25°) using 15 years of photographs, observations, and field notes. The compass headings of lines of recognizable debris (e.g., trails of potsherds and charred grains) were used to determine an average direction. Table S1 below summarizes the site locations where directional evidence was discovered.

Asteroid airburst modeling (adapted from West et al. [9])
For this study, three co-authors (L.C., M.D.Y., and A.W.) were involved in various stages of the modeling, image rendering, and video production under the leadership of L.C., an expert Autodyn instructor for Ozen Engineering, Inc. L.C. recommended using Autodyn, based on his modeling work for the U.S. Army Futures Command Combat Capabilities

Development Center, where he used Autodyn to produce various hydrocode models and simulations, including for geological impacts at high strain rates.

First, we modeled the airbursts using the Earth Impact Effects Program (EIEP) by Marcus et al. [145] and Collins et al. [129, 130] We entered projectile diameters, densities, velocities, entry angles, and target densities to determine the estimated burst heights, energies in megatons and joules, peak overpressures, and wind velocities. Results from the EIEP show that for nearly all low-altitude touch-down airburst events, no typical impact craters form, although large fragments may strike Earth's surface. The airburst energies used in the Autodyn calculations approximately correspond to observed values, where known.

Next, we entered the output generated by the EIEP into Autodyn using the following parameters, assumptions, and specifications:

(i) We used Autodyn's two-dimensional Eulerian hydrocode solver.

(ii) Following Saito et al. [135, 136] and Boslough and Crawford [66], we specified a 90° entry angle for simplicity. Although statistically less likely than a 45° entry angle for asteroids, comets from the spherical Oort cloud are equally as likely to impact at 90° as at any other angle.

(iii) We used the Tillotson equation-of-state (EOS), an expression that describes the relationship between pressure, volume, and temperature during high-speed impacts. The Tillotson EOS only approximates the temperatures involved, so the temperature calculations are considered semiquantitative; they are presented here primarily to illustrate convection currents.

(iv) We also used von Mises strength values to predict the yielding or fracturing of materials under complex loading conditions.

(v) The Hydro (Pmin) failure values were used to determine when a material exceeds a specified pressure value in the tensile direction.

(vi) The appropriate physical/mechanical properties for each material are listed in the **Supporting Information**).

(vii) All materials were assumed to be homogeneous for this study, but asteroids and comets are likely heterogeneous, fractured, and semi-porous.

(viii) The downward pre-burst and post-burst velocity values provided by the EIEP were entered into Autodyn, which used them in its calculations.

(ix) For our Autodyn models, we used horizontal axial symmetry [135, 136], where only half of the domain is modeled, and the other half is duplicated horizontally through symmetry.

(x) The meshes were modeled at 356 × 356 cells, measuring 4.2 m wide × 2.1 m high.

(xi) Following Collins et al. [129], we modeled the bolides as solid homogeneous deformed spheres, but in actuality, they are high-velocity swarms of heterogeneous co-moving fragments and vapor. Atmospheric friction causes the swarm to assume a pancake-like shape, and most energy dissipates in the air. In these simplified models, we did not consider fragmentation; however, we did use the same airburst energy calculated by the EIEP.

(xii) Convergence for spatial resolution was not explored because these models are first-order approximations.

(xiii) Unless otherwise specified, computational input and output were in millimeters (mm), milligrams (mg), and milliseconds (ms). See **Supporting Information** for input parameters.

In Autodyn, each model's simulation run-time was typically 2-4 hours. The image sequence generation for creating videos typically required 5-10 hours for each parameter, e.g., temperature or pressure. All models and figures were created using Autodyn-2D, versions 2023 R1 and 2023 R1 Student (Ansys, Inc.). Videos were created using Camtasia, Version 23.3.3 (Build 49804), 2023. The figures illustrate visible materials, semiquantitative temperature, pressure, shock speed, and material bulk failure on scales with up to 50 colored divisions.

Earth Impact Effects Program [130, 145] (accessed 12/2023)
Stony asteroid:
Impactor diameter = 55 m
Density = 2920 kg/m^3, dense rock,
Impactor velocity = 11 km/s = 11000 mm/ms
Entry angle = 90°
Target density = 2500 kg/m^3
Energy, Mt = 3.68 Mt, 1.54e16 Joules
Initial breakup = 47.9 km
Airburst altitude = 653 m
Distance below airburst = 653 m
Residual velocity = 2.09 km/s = 2090 mm/ms
Peak overpressure at ground = ~0.012 GPa
Wind velocity = 1950 m/s
Air blast will arrive ~2.8 s after impact
No crater; large fragments may strike the ground
Average recurrence interval = 1100 years

Autodyn-2D
Unless otherwise specified, units below are reported in mg, mm, and ms.

Material Name – Asteroid

Equation of State	Tillotson model
Reference density	2.92000E + 00 (g/cm³)
Parameter A	4.55500E + 07 (kPa)
Parameter B	1.60500E + 06 (kPa)
Parameter a	5.00000E-01 (none)
Parameter b	6.00000E-01 (none)
Parameter alpha	5.00000E + 00 (none)
Parameter beta	5.00000E + 00 (none)
Parameter e0	1.00000E + 07 (J/kg)
Parameter es	2.75000E + 08 (J/kg)
Parameter esd	1.50000E + 09 (J/kg)
Reference Temperature	1.80000E + 02 (K)
Specific Heat	1.00000E + 03 (J/kgK)
Thermal Conductivity	5.00000E + 00 (J/mKs)
Strength	**von Mises model**
Shear Modulus	5.30000E + 07 (kPa)
Yield Stress	3.44000E + 08 (kPa)
Failure	**Hydro (Pmin)**
Hydro Tensile Limit	−2.75000E + 04 (kPa)
Reheal	Yes
Crack Softening	No
Stochastic failure	No
Erosion	**None**
Material Cutoffs	-
Maximum Expansion	5.00000E-01 (none)
Minimum Density Factor	1.00000E-04 (none)
Minimum Density Factor (SPH)	2.00000E-01 (none)
Maximum Density Factor (SPH)	3.00000E + 00 (none)
Minimum Shock speed	1.00000E-06 (m/s)
Maximum Shock speed (SPH)	1.01000E + 05 (m/s)
Maximum Temperature	1.01000E + 20 (K)
Reference:	-

Minimum Density Factor	1.00000E-04 (none)
Minimum Density Factor (SPH)	2.00000E-01 (none)
Maximum Density Factor (SPH)	3.00000E + 00 (none)
Minimum Shock speed	1.00000E-06 (m/s)
Maximum Shock speed (SPH)	1.01000E + 05 (m/s)
Maximum Temperature	1.01000E + 20 (K)
Reference:	-

Material Name – AIR

Equation of State	Ideal Gas
Reference density	1.22500E-03 (g/cm³)
Gamma	1.40000E + 00 (none)
Adiabatic constant	0.00000E + 00 (none)
Pressure shift	0.00000E + 00 (kPa)
Reference Temperature	2.88200E + 02 (K)
Specific Heat	7.17600E + 02 (J/kgK)
Thermal Conductivity	0.00000E + 00 (J/mKs)
Strength	**None**
Failure	**None**
Erosion	**None**
Material Cutoffs	-
Maximum Expansion	1.00000E-01 (none)
Minimum Density Factor	1.00000E-04 (none)
Minimum Density Factor (SPH)	2.00000E-01 (none)
Maximum Density Factor (SPH)	3.00000E + 00 (none)
Minimum Shock speed	1.00000E-02 (m/s)
Maximum Shock speed (SPH)	1.01000E + 20 (m/s)
Maximum Temperature	1.01000E + 20 (K)
Reference:	"Thermodynamic and Transport Properties of Fluids, SI Units", GFC Rogers, YR Mayhew

Material Name – Earth

Equation of State	Tillotson model
Reference density	3.30000E + 00 (g/cm³)
Parameter A	1.00000E + 08 (kPa)
Parameter B	3.54000E + 07 (kPa)
Parameter a	5.00000E-01 (none)
Parameter b	6.00000E-01 (none)
Parameter alpha	5.00000E + 00 (none)
Parameter beta	5.00000E + 00 (none)
Parameter e0	1.00000E + 07 (J/kg)
Parameter es	2.50000E + 08 (J/kg)
Parameter esd	1.40000E + 09 (J/kg)
Reference Temperature	2.88000E + 02 (K)
Specific Heat	9.20000E + 02 (J/kgK)
Thermal Conductivity	5.00000E + 00 (J/mKs)
Strength	**von Mises model**
Shear Modulus	4.50000E + 07 (kPa)
Yield Stress	6.19000E + 08 (kPa)
Failure	**Hydro (Pmin)**
Hydro Tensile Limit	−6.88000E + 04 (kPa)
Reheal	Yes
Crack Softening	No
Stochastic failure	No
Erosion	**None**
Material Cutoffs	-
Maximum Expansion	1.00000E-01 (none)

Material Name – Mudbrick

Equation of State	Tillotson model
Reference density	1.50000E + 00 (g/cm³)
Parameter A	4.55500E + 07 (kPa)
Parameter B	1.60000E + 06 (kPa)
Parameter a	5.00000E-01 (none)
Parameter b	6.00000E-01 (none)
Parameter alpha	5.00000E + 00 (none)
Parameter beta	5.00000E + 00 (none)
Parameter e0	1.00000E + 07 (J/kg)
Parameter es	2.75000E + 08 (J/kg)
Parameter esd	1.50000E + 09 (J/kg)
Reference Temperature	2.93000E + 02 (K)
Specific Heat	1.00000E + 03 (J/kgK)
Thermal Conductivity	5.00000E + 00 (J/mKs)
Strength	**von Mises model**
Shear Modulus	5.30000E + 07 (kPa)
Yield Stress	3.44000E + 08 (kPa)
Failure	**Hydro (Pmin)**
Hydro Tensile Limit	−2.75000E + 04 (kPa)
Reheal	Yes
Crack Softening	No
Stochastic failure	No
Erosion	**None**
Material Cutoffs	-
Maximum Expansion	1.00000E-01 (none)
Minimum Density Factor	1.00000E-04 (none)

Minimum Density Factor (SPH)	2.00000E-01 (none)
Maximum Density Factor (SPH)	3.00000E + 00 (none)
Minimum Shock speed	1.00000E-06 (m/s)
Maximum Shock speed (SPH)	1.01000E + 20 (m/s)
Maximum Temperature	1.01000E + 20 (K)
Reference:	-

Initial Condition Summary

Name:	**Air**
Material:	AIR
Density	1.22E-03
Internal Energy	2.07E + 05
Shell Thickness	0.00E + 00
X Velocity	0.00E + 00
Y Velocity	0.00E + 00

Name:	**Asteroid Energy**
Material:	Asteroid
Density	2.92E + 00
Internal Energy	4.59E + 08
Shell Thickness	0.00E + 00
X Velocity	2.09E + 03
Y Velocity	0.00E + 00

Name:	**Asteroid**
Material:	Asteroid
Density	2.92E + 00
Internal Energy	0.00E + 00
Shell Thickness	0.00E + 00
X Velocity	1.10E + 04
Y Velocity	0.00E + 00

Name:	**Mudbrick walls**
Material:	Mudbrick
Density	1.50E + 00
Internal Energy	0.00E + 00
Shell Thickness	0.00E + 00
X Velocity	0.00E + 00
Y Velocity	0.00E + 00

Appendix, Figures
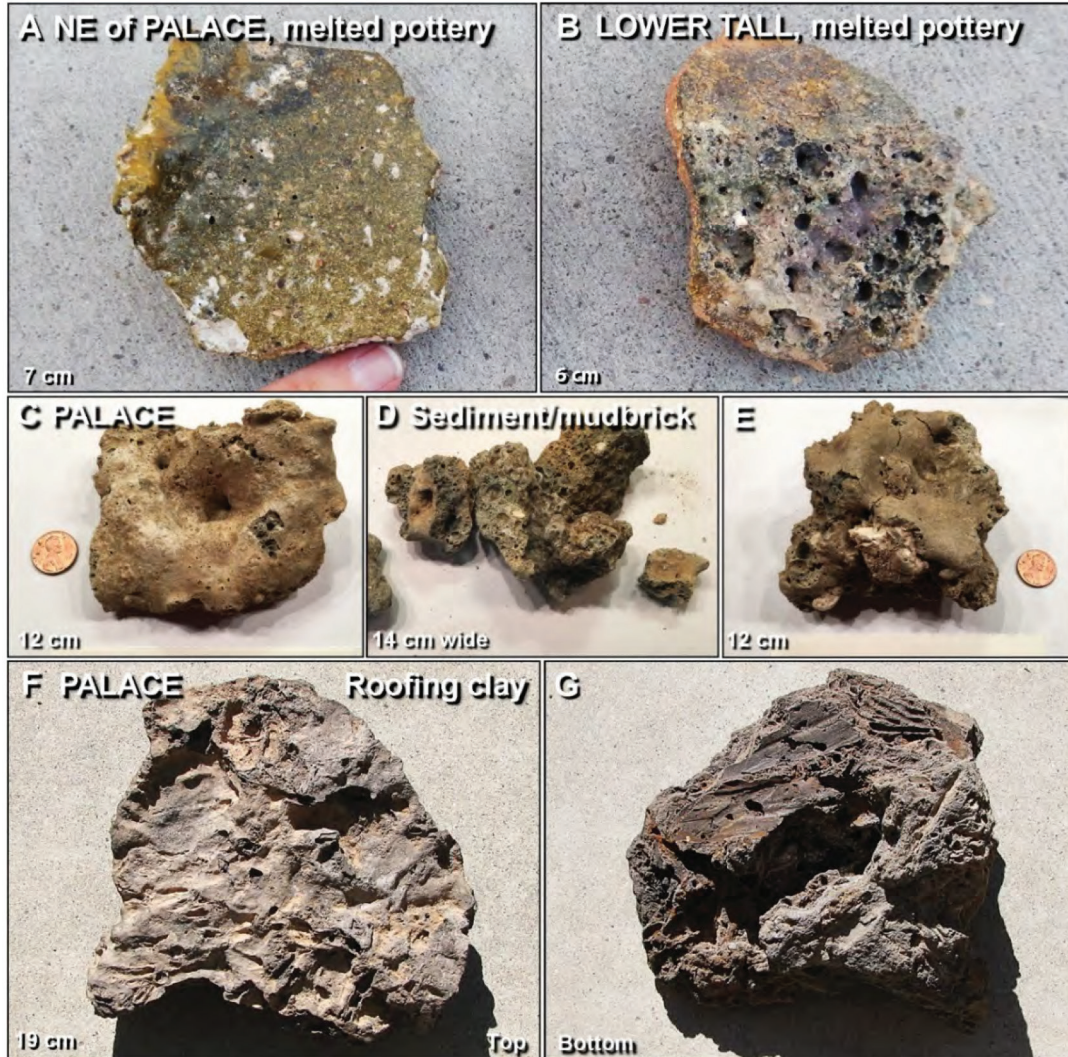
Appendix, Figure A1: *Melted materials*. **(A)** Photograph of a 7-cm-wide potsherd from the NE of the palace showing an outer surface that melted at high temperatures. **(B)** A photograph of a 6-cm-wide potsherd from the lower tall displays a highly vesicular, melted outer surface. **(C)** The upper surface of the melted mudbrick fragment shows a melted 'skin.' **(D)** Broken surfaces of mudbrick meltglass display a vesicular texture. **(E)** A photograph shows the upper surface and broken faces of mudbrick meltglass. **(F)** The upper surface of a 19-cm-wide piece of roofing clay melted at high temperatures. **(G)** The same object's lower surface shows imprints of plant material silicified at high temperatures. Images and caption adapted from Bunch et al. [1], usable under Creative Commons, CC by 4.0 (http://creativecommons.org/licenses/by/4.0/).
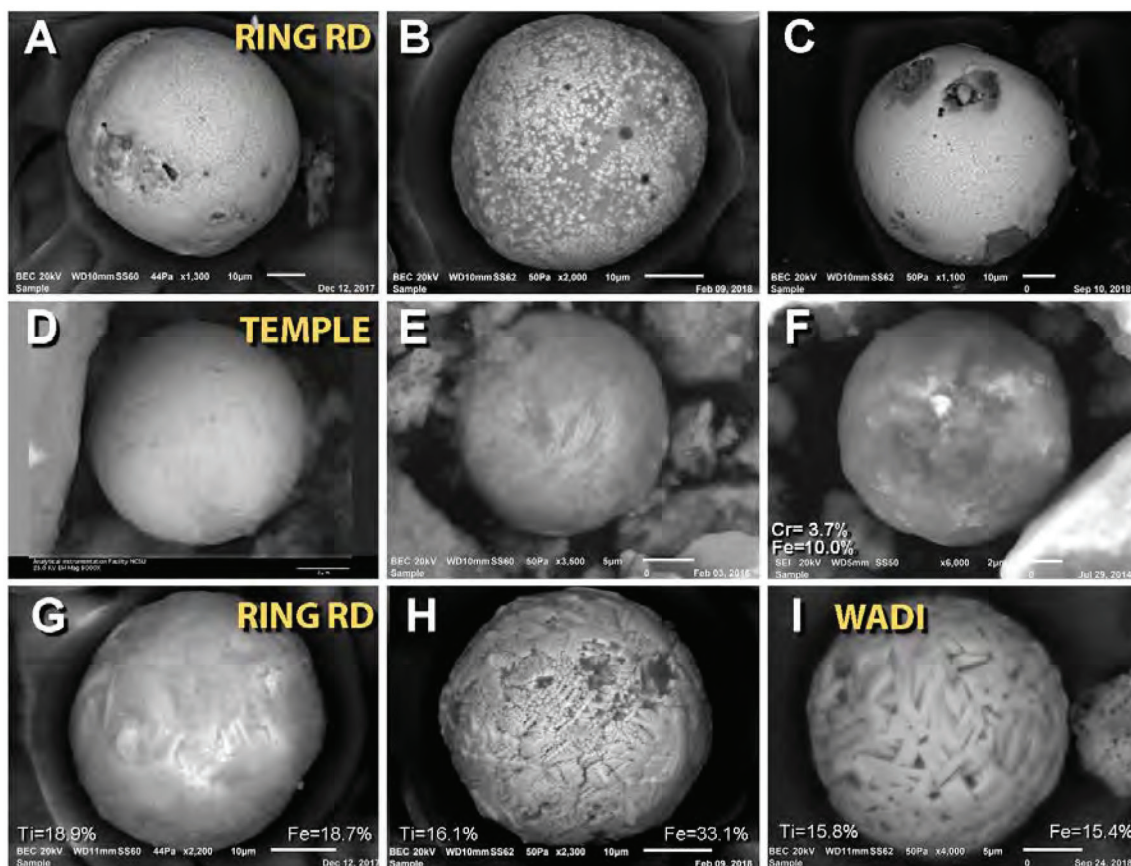
Appendix, Figure A2: *SEM images of microspherules.* **(A)-(C)** Silica-rich spherules from the ring road around the lower tall. **(D)-(F)** Iron-rich spherules from the temple complex. **(G)-(I)** Titanium-rich spherules from the ring road and wadi sites. Ti content ranges from 18.9 to 1.2 wt%, averaging 10.7 wt%. Images and caption adapted from Bunch et al. [1], usable under Creative Commons, CC by 4.0 (http://creativecommons.org/licenses/by/4.0/). An unusual microspherule enriched in rare-earth elements (REEs) was previously reported (Fig. 26 of Bunch et al. [1]) but is not shown here.

Appendix, Figure A3: *Palace on the upper tall.* **(A)** An artist's hypothetical reconstruction of the 52-m-long multi-story palace before its destruction by the airburst. **(B)** An artist's hypothetical reconstruction of the palace site shortly after its destruction, superimposed on the modern excavation. "MBA" (upper right) indicates the top of Middle-Bronze-age rubble. Once almost completely covered with buildings, the surrounding field has been leveled by the proposed airburst. The airburst shockwave scoured the palace complex, burying the few remaining courses of mudbricks. Debris once filled the area between sheared walls but was removed by the excavators. The comparison of panel 'A' to panel 'B' shows that the numerous mudbricks from the palace and other buildings are missing. Bunch et al. [1] discussed evidence that this debris had been blown off the tall to the NE. Images and caption adapted from Bunch et al. [1], usable under Creative Commons, CC by 4.0 (http://creativecommons.org/licenses/by/4.0/).
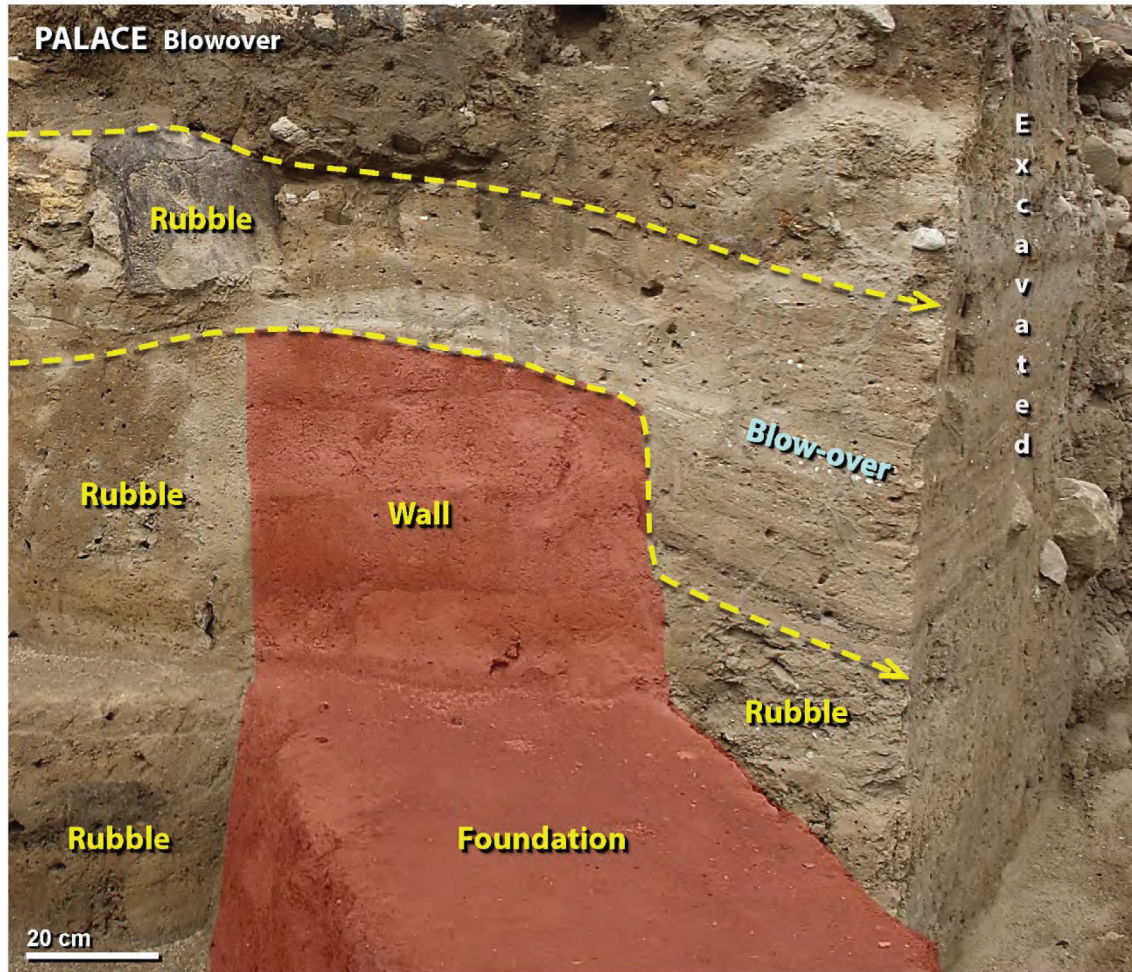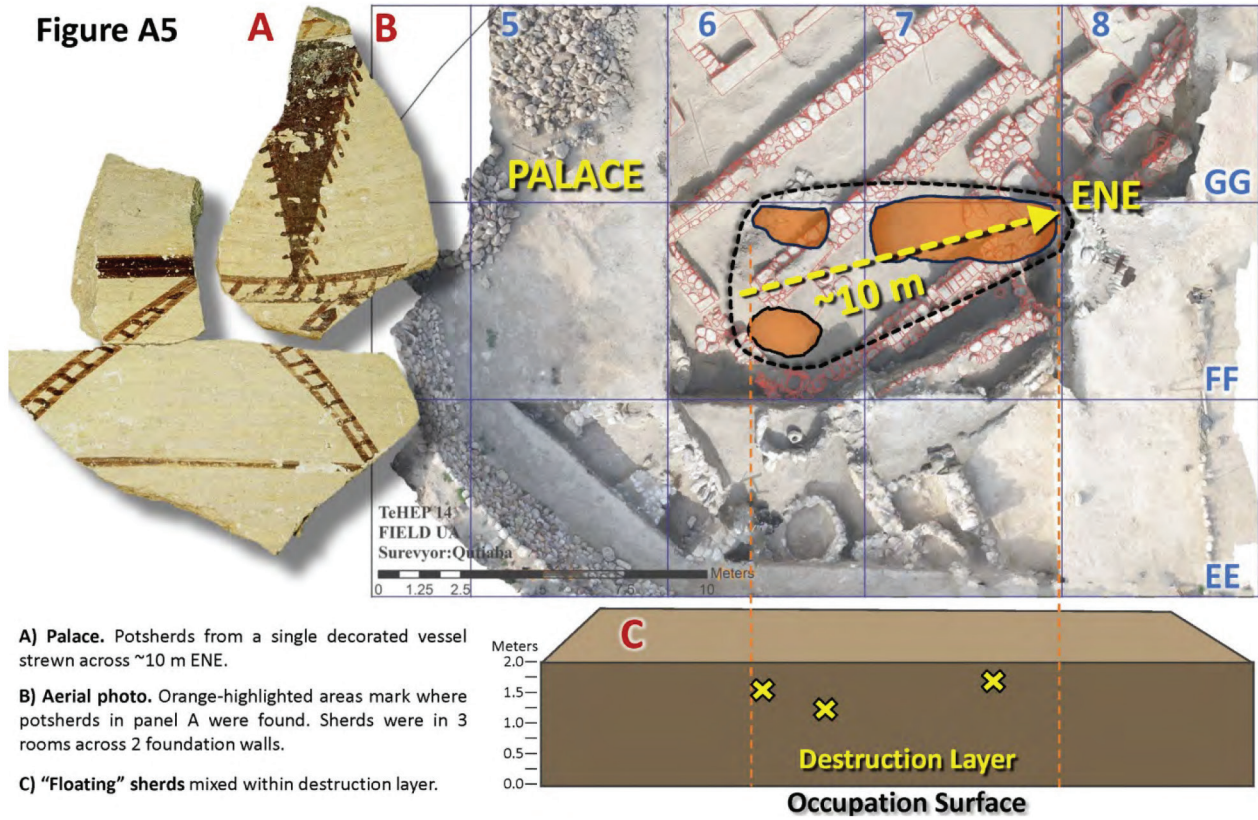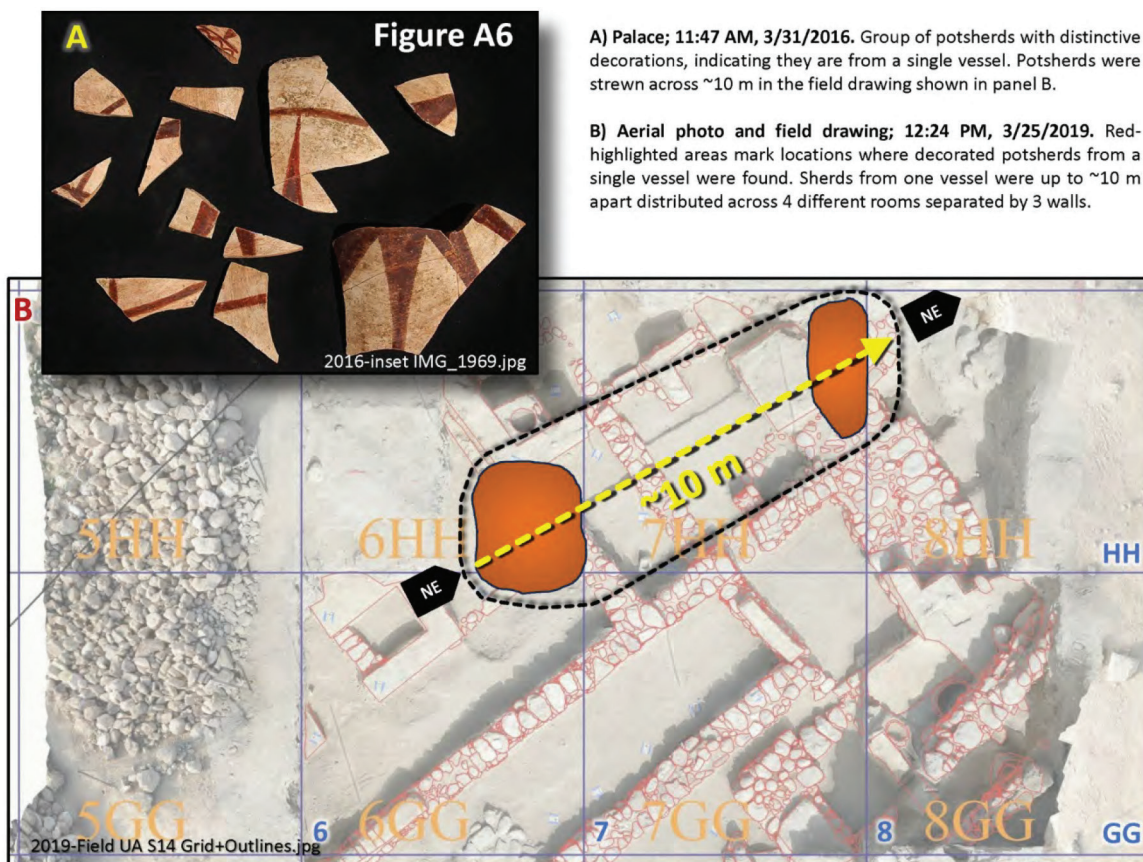
Appendix, Figure A4: *Photograph of an excavated palace wall.* In the center are the lower few courses of a mudbrick wall ('Wall' and 'Foundation'; in red). Sediment between the yellow dashed lines represents a "blow-over" deposited by the proposed airburst blast wave; the inferred wind direction is to the NE. "Rubble" mainly indicates broken and pulverized mudbricks from the destroyed walls. Note the line of white fragments of broken plaster intermixed with small carbonate spherules within the blow-over layer, inferred to have been stripped off the plastered palace walls and melted by the high-temperature, high-velocity blast wave. The top of the wall is curved downward, consistent with abrasion by intense winds traveling from SW to NE. On the right side of the image, "Excavated" marks the limit of the modern excavated section. Image and caption adapted from Bunch et al. [1], usable under Creative Commons, CC by 4.0. (http://creativecommons.org/licenses/by/4.0/).

Figure A5

A) **Palace.** Potsherds from a single decorated vessel strewn across ~10 m ENE.

B) **Aerial photo.** Orange-highlighted areas mark where potsherds in panel A were found. Sherds were in 3 rooms across 2 foundation walls.

C) **"Floating" sherds** mixed within destruction layer.

Appendix, Figures A5-A12:   (continued)

A) Palace; 11:47 AM, 3/31/2016. Group of potsherds with distinctive decorations, indicating they are from a single vessel. Potsherds were strewn across ~10 m in the field drawing shown in panel B.

B) Aerial photo and field drawing; 12:24 PM, 3/25/2019. Red-highlighted areas mark locations where decorated potsherds from a single vessel were found. Sherds from one vessel were up to ~10 m apart distributed across 4 different rooms separated by 3 walls.

Appendix, Figures A5-A12: (continued)

Figure A7

Palace; 11:36 AM, 3/11/2016. Pot mended from sherds strewn across ~5 m of orange area in panel B.

Palace. Colorized field drawing by co-author P. Silvia. NE line of 150+ sherds strewn across ~5 m (orange area). Walls tan; stones blue.

Palace; 11:56 AM, 3/11/2016. Part of mended pot from sherds strewn across orange area of panel B.

Palace; 11:43 AM, 02/18/2016. Potsherds from some of 150+ vessels in orange area of panel B. Sherds from individual pots extend across ~5 m.

Appendix, Figures A5-A12: (continued)

Figure A8

Ring Rd; 11:20 AM, 02/06/2012. ~70-cm-long cluster of NNE-trending potsherds.

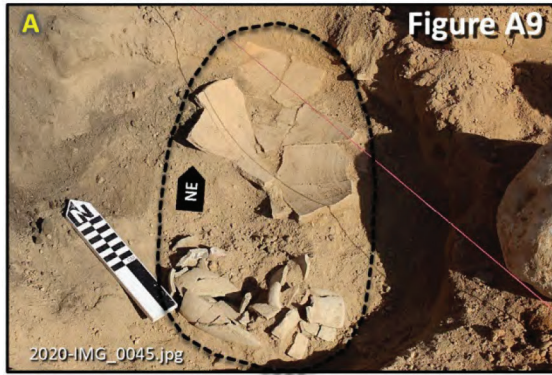Ring Rd; 2:40 PM, 1/23/2012. ~60-cm-long group of potsherds. Mixed with rocks from fallen wall.

Palace; 2:58 PM, 2/4/2020. Potsherds from a single shattered pot banked up against mudbrick wall and strewn NE across ~70 cm.

Ring Rd; 1:53 PM, 01/28/2013. 1.5-m-long group of potsherds, mixed with rocks from fallen wall.

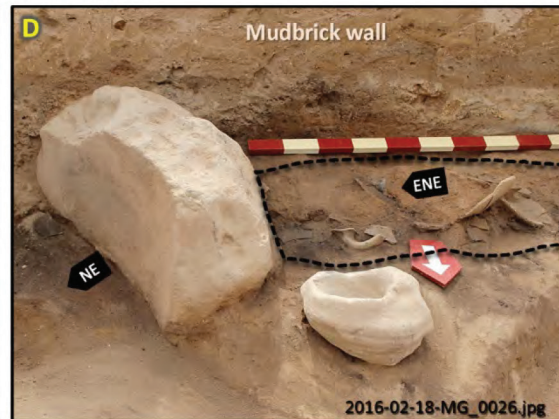**Appendix, Figures A5-A12:**   (continued)

Palace; 3:50 PM, 2/3/2020. ~50-cm-long NE trail of potsherds.

Palace; 10:47 AM, 2/9/2016. Potsherds from single pot, mixed with rocks and a bone.

Ring Rd. 3:36 PM, 12/28/2010. Potsherds from single pot. Mixed with rocks at base of fallen wall.

Palace; 11:43 AM, 02/18/2016. 200-kg quern tipped to NE. Sherds from 150+ vessels banked up to wall and against quern with none on NW side.

Appendix, Figures A5-A12: (continued)

Figure A10

Palace; 11:06 AM, 02/17/2017. ~90-cm trail of potsherds intermixed with rocks from fallen wall.

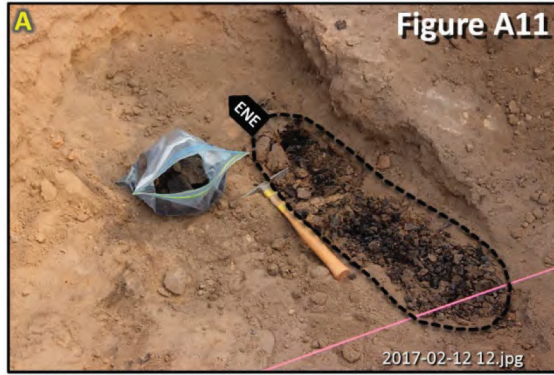Palace; 10:18 AM, 2/10/2019. Potsherds from a single pot strewn NE across ~1.5 m.

Palace; 10:00 AM, 2/19/2018. ~1-m-long NE-trending group of potsherds from multiple vessels, intermixed with rocks.

Ring Rd. 6:27 AM, 01/16/2011. Potsherds from single pot among rocks of fallen wall.

Appendix, Figures A5-A12: (continued)

Figure A11

A Palace; 2:00 PM, 2/12/2017. ENE-trending trail of charcoal.

B Palace; 1:28 PM, 2/3/2016. Cluster of ENE-trending charcoal and charred seeds intermixed with fragments of floor plaster.
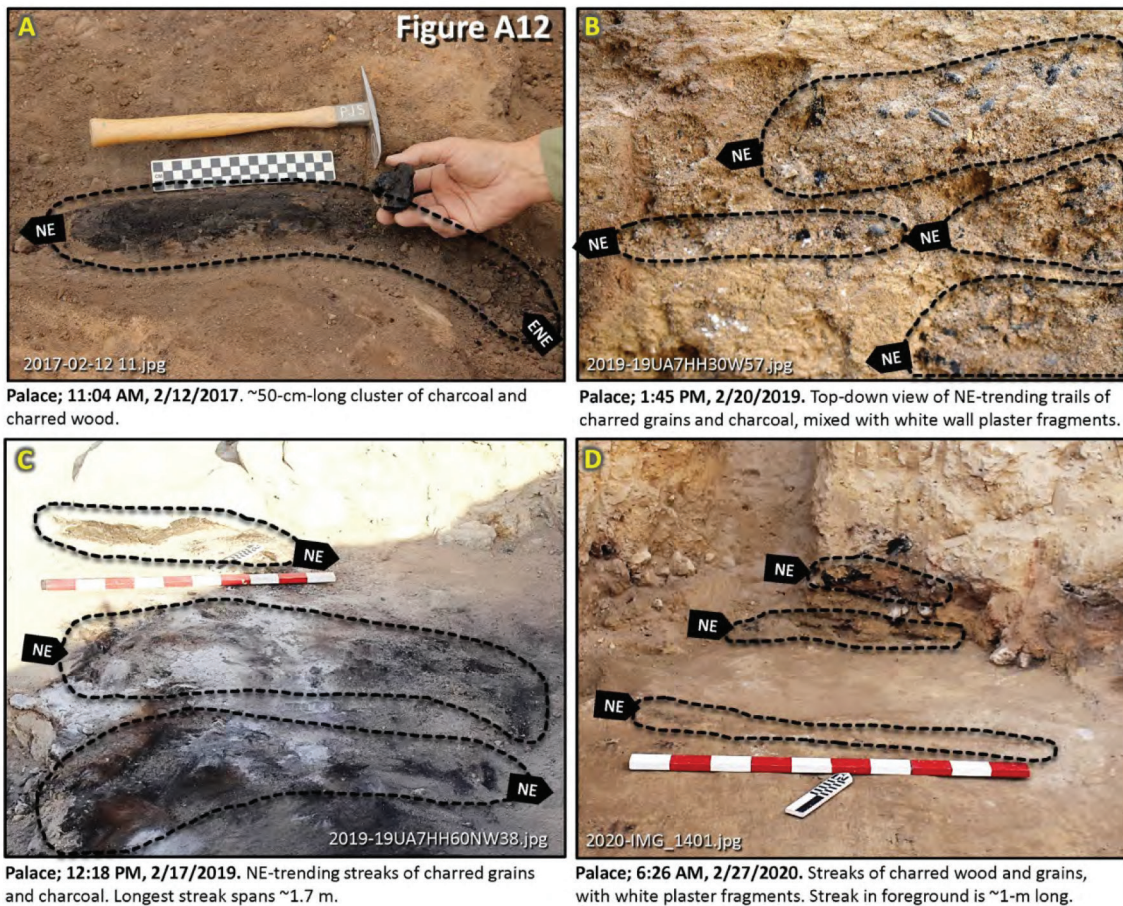
C Palace; 1:10 PM, 2/11/2019. ~1.5-m-long NE trail of charcoal against and along the base of a collapsed wall.

D Palace; 11:45 AM, 2/18/2016. ~70-cm-long NE-trending streak of charred grains, strewn NE from top of the tipped over quern.

Appendix, Figures A5-A12: (continued)

Figure A12

Palace; 11:04 AM, 2/12/2017. ~50-cm-long cluster of charcoal and charred wood.

Palace; 1:45 PM, 2/20/2019. Top-down view of NE-trending trails of charred grains and charcoal, mixed with white wall plaster fragments.

Palace; 12:18 PM, 2/17/2019. NE-trending streaks of charred grains and charcoal. Longest streak spans ~1.7 m.

Palace; 6:26 AM, 2/27/2020. Streaks of charred wood and grains, with white plaster fragments. Streak in foreground is ~1-m long.

Appendix, Figures A5-A12: Additional images of directional evidence for potsherds (**A5-A10**) and charred grains/charcoal (**A11-A12**).